CONSTRAINING THE DYNAMICAL MASSES OF SPT2349-56: A MASSIVE GALAXY PROTOCLUSTER AT Z $\sim$ 4.3

by:

Ryan Perry

Submitted in partial fulfilment of the requirements
for the degree of Master of Science

at

Dalhousie University
Halifax, Nova Scotia
September 2018

Contents

List of Tables

List of Figures

Abstract

This study presents an analysis of SPT2349-56, the brightest unlensed source found by the South Pole Telescope during a 2500 $\deg^2$ survey of the sky. Follow-up observations showed that SPT2349-56 is comprised of 14 Submillimeter Galaxies, all at the same redshift ($z \sim 4.3$), suggesting that SPT2349-56 is a massive high redshift protocluster. Using this data, the kinematic properties from 12 galaxies within the protocluster were derived by probing the [CII] emission line. From these results, the mass of each source was measured from two different mass estimates: one based on the turbulence of the galaxy and the other based on the rotation of the galaxy. The mass estimates are compared to one another, and a new optimal mass estimate is provided for a range of galaxy environments. The mass fractions within each galaxy are also measured, as well as the total mass fraction for the protocluster as a whole.

List of Abbreviations Used

ALMA: Atacama Large Millimeter/Submillimeter Array

CMB: Cosmic Microwave Background

IGrM: Intragroup Medium

ISM: Interstellar Medium

SED: Spectral Energy Distribution

SFR: Star Formation Rate

SMG: Submillimeter Galaxy

SPT: South Pole Telescope

submm: Submillimeter

Chapter 1

Introduction

Surveys at the far-infrared and sub-millimeter (submm) wavelengths have demonstrated the value of studying dusty, high redshift galaxies and their relevance to the evolution of the universe [1]. During the early 1990s, the absolute energy distribution of the universe was measured using the Far-Infrared Absolute Spectrophotometer (FIRAS) aboard the space based Cosmic Background Explorer (COBE) at wavelengths above $150\mu m$ [1]. The implications of these measurements, along with prior measurements of nearby galaxies using the Infrared Astronomy Satellite (IRAS), demonstrated that the universe emits a comparable energy in the infrared and submm wavelengths as it does at the much more well studied optical and ultraviolet spectrums [1]. Thus, if astronomers limited themselves to the optical and ultraviolet wavelength alone, they would miss approximately half of the star formation activity in the universe. Even more interesting is that most of these infrared and submm emitting sources occur at high redshift ($z > 1$), which is where most of the universe's star formation took place [2]. Thus, by observing galaxies that emit these wavelengths, some of the first galaxies ever formed can be observed.

Attempting to observe sources at these long wavelengths has many difficulties. Due to water vapour in the atmosphere, measurements must be made from either a very high or dry place on the earth, or space, which puts extreme limits on where telescopes can be positioned. The longer wavelengths at which these galaxies must be observed also results in low resolution. Despite these limitations, the field has seen a massive amount of interest and attempts to get better resolution images [1].

Submm bright objects were first detected using the Submillimeter Common-User Bolometer Array (SCUBA) at 850 μm on the James Clerk Maxwell Telescope (JCMT) in the late 1990's [3]. High redshift sources that were bright in the infrared/submm wavelengths and nearly invisible at the optical were observed. These are known as Submm Galaxies (SMGs). These discoveries completely changed our perception of galaxy formation. Since the majority of these sources were found to be at high redshift, it allowed astronomers to observe galaxies at the beginning of their evolution [1].

SMGs are known for being the most luminous galaxies in the universe, with luminosities reaching as high as $\sim 10^{13}$ L$_\odot$ [4]. These objects also have incredibly high star formation rates (SFRs) which can reach as high as 10^2 - 10^3 M$_\odot$/yr (incredibly high comparing to the Milky Way's $\sim$ 1 - 2 M$_\odot$/yr). The defining feature of these objects (namely, the wavelengths of their emissions) have been attributed to the amount of dust that enshrouds the galaxy [1]. The radiation that is initially emitted by these massive young stars in the galaxy is absorbed by the surrounding dust, heating it to $\sim 20 - 60$K, and then is remitted via thermal radiation [1]. This thermal radiation is initially emitted in the infrared wavelengths, but is redshifted to the submm regime. Thus giving them the name, Submillimeter Galaxies.

The highest number density of SMGs appear at a redshift (z) of z $\sim$ 2 - 3, which implies that they were most prominent during the peak formation of the universe [3]. SMGs are also thought to be the progenitors of the present day massive elliptical galaxies [4]. Although it's clear that these objects are extremely important to the evolution of the universe, they are also quite rare, with space densities of about 10^{-5} -

10^{-6} Mpc^{-3} [4]. This rarity is attributed their relatively short period of star formation ($<$ 100Myr) which makes it uncommon to observe an SMG undergoing a starburst.

Although now there are many telescopes dedicated to SMG identification, follow-up observations on SMGs once they are found is difficult due to the coarse resolution delivered by single dish telescopes. One major complication that can occur is that objects will blend together due to low resolution (or equivalently, large beam size) of the telescopes [5]. A typical single antenna has a resolution of $14''$ (at a wavelength of $850\mu m$ on a 15m telescope) whereas galaxies in general are about $0.5''$ in diameter. Thus, when an object is found with the $14''$ resolution, it could be that numerous galaxies are within the detection that are unresolved and appear as one source. This is to be expected since some studies have shown that SMGs are a product of mergers (where galaxies are $1''$-$2''$ apart) and that they reside in the most over dense regions of the universe. [6]

The brightest SMGs recorded are the most luminous galaxies in the universe and are known for having the most intense starbursts ever observed [1]. It is clear that these galaxies play an extremely important role in the evolution of the universe, and so it's very important for these objects to be studied in detail.

This thesis analyzes the galaxy field SPT2349-56, an extremely over dense population of SMGs comprised of 14 submillimeter bright galaxies. For each of the individual galaxies, their kinematics are determined and physical properties are derived from these results.

The structure of the thesis is as follows. Chapter 2 gives background context to the field of Astronomy, as well as SMGs in general. The concept of redshift is discussed, why it's important in astronomy, and how it relates to other observable properties. Then, basic galaxy properties are explained and the different processes in which galaxies evolve are described. Next, the radiation emitted from galaxies is explored, as well as how it is used to determine the motions of the stars and gas within the galaxy. In particular, the emission line [CII], the emission line observed in SPT2349-56, is examined. Lastly, the relationship between the kinematics of a galaxy and how to determine its total mass is explained.

Chapter 3 introduces the instrumentation used to image astrophysical objects. In particular, SMGs are observed by a method known as aperture synthesis, which is described fully.

Chapter 4 outlines the motivation as to why the research is important, as well as introducing the field SPT2349-56.

In Chapter 5 the data analysis is shown, which measures the kinematics of the galaxies within SPT2349-56. Each emission contained within a galaxy line is fit and parameters from each fit in the galaxy are extracted in order to determine the kinematics of each source.

Chapter 6 determines the physical properties of the galaxies within SPT2349-56 from the kinematic properties found in Chapter 5, such as the radius, the total velocity spread, the integrated dispersion, and the mass. Also, each source within SPT2349-56 is described in full detail, in order to gain a better understanding of the specific physical processes going on within each of the galaxies.

Chapter 7 proposes a new way to calculate the dynamical mass of a galaxy for a variety of different types of kinematics, instead of confining ourselves to just two different estimates. Next, the subcomponents of the mass for each galaxy in SPT2349-56 are measured and compared to other SMGs with measured mass fractions. Lastly, the mass fractions of the protocluster as a whole are measured.

Chapter 8 gives the conclusions and suggests what may be done next to further the research shown in this thesis. In particular, attempting to get higher resolution images of SPT2349-56 and to find more astrophysical systems similar to SPT2349-56 in order to access to significance of these results.

Chapter 2

Background

2.1 Redshift and Distance

In order to understand fully this thesis, it's important to first introduce a few key concepts in the topic of astronomy. Redshift (z) is the process that occurs when a wave emitted from an object shifts towards a lower energy (or equivalently, lower frequency) state. This is the case for the energy of a photon since it is given by the following formula:

$$E_{\text{photon}} = hf \tag{1}$$

The effect of redshift was first discovered in the 19th century by Christian Andreas Doppler who was the first person to give a physical explanation for the phenomenon's existence [7]. Doppler suggested that as a wave emitting source moved away from an observer, each successive wavefront would be emitted farther from the observer than the previous wave was. Thus, the time it took each successive wavefront to reach the observer would be increased, or equivalently increasing the time interval between each wavefront and decreasing the frequency of the wave. The phenomenon was then named, the Doppler effect. The most common occurrence of this effect comes in the form of sound waves.

Doppler theorized that this would be the case for all types of waves, even light [7]. This theory was proven correct by Armand Hippolyte-Louis, who was the first person to observe the Doppler effect for light by looking at the spectral lines from stars [7]. He too observed that the light emitted by objects that are moving away from an observer are shifted to a lower frequency, or equivalently, the light is shifted more into the "red" end of the spectrum. Hence, the effect is also given the name "redshift". Conversely for an object moving towards an observer, they experience a "blueshift" (shifting to a higher energy / frequency state.).

Initially cosmological redshifts were interpreted as being due to the Doppler Effect [8]. Edwin Hubble was one of the first to notice there may be another process at play in which light can be redshifted. Hubble measured the radial velocities of 24 galaxies where the distances to each were known [8]. He then realized that the distance to each galaxy and their velocity were related by what we now know as Hubble's Law, which is

$$v = H_0 r \tag{2}$$

where v is the radial or recessional velocity away from earth, r is the distance to the object, and H_0 is the Hubble parameter which is most commonly quoted in literature as $H_0 = 70 \frac{km/s}{Mpc}$. The conclusion from these measurements led astronomers to believe that the universe was expanding [8]. Hubble also started to realize that there was a relation between the redshift of light emitted by an object, and the distance to the object themselves. It didn't take long for astronomers to realize that these observations could be explained by solutions to Einstein's equations of General Relatively, in which redshifts of light appear as a consequence of an expanding universe [8]. This cosmological redshift is different than the Doppler Effect in the sense that the light increases in wavelength not due to the relative motion of the observer and the object, but due to the expansion of the space the light travels through [8].

The cosmological redshift is typically described by the following equation:

$$1 + z = \frac{\lambda_{obs}}{\lambda_{rest}} \tag{3}$$

where λ_{obs} and λ_{rest} are the observed and rest wavelengths respectively, and z is the cosmological redshift parameter.

The redshift of an object can be determined by looking at its spectral lines. Scientists have discovered that each element in the periodic table can only emit photons at very specific wavelengths that are related to the atom's energy levels. Thus, for a given spectrum of a galaxy, the pattern of the spectral lines will remain the same as in the rest frame, but they will be shifted to longer wavelengths. By distinguishing the spectral lines in a given pattern, one can determine the redshift of a galaxy given equation 3, by determining how much the lines have been shifted.

Redshift is also often used to talk about the age of the universe since the amount light is redshifted depends on how long it travels through the expanding universe. Figure 1 shows an model used to approximate the relationship between redshift and the age of the universe which is defined by:

$$t = \frac{2H_0^{-1}}{1 + (1 + z)^2} \tag{4}$$

where t is time, H_0 is the Hubble parameter, and z is redshift [9].

The relationship between redshift and distance is much more complicated however, due to the expansion of the universe. Not only has the universe been expanding, its rate of expansion has been changing over time as well. Thus, the distance between two objects when the light was first emitted is not the same as when the light finally reaches its observer. However, a common distance that is used in astronomy is known as Luminosity Distance (D_L) which describes the distance light travels to reach an

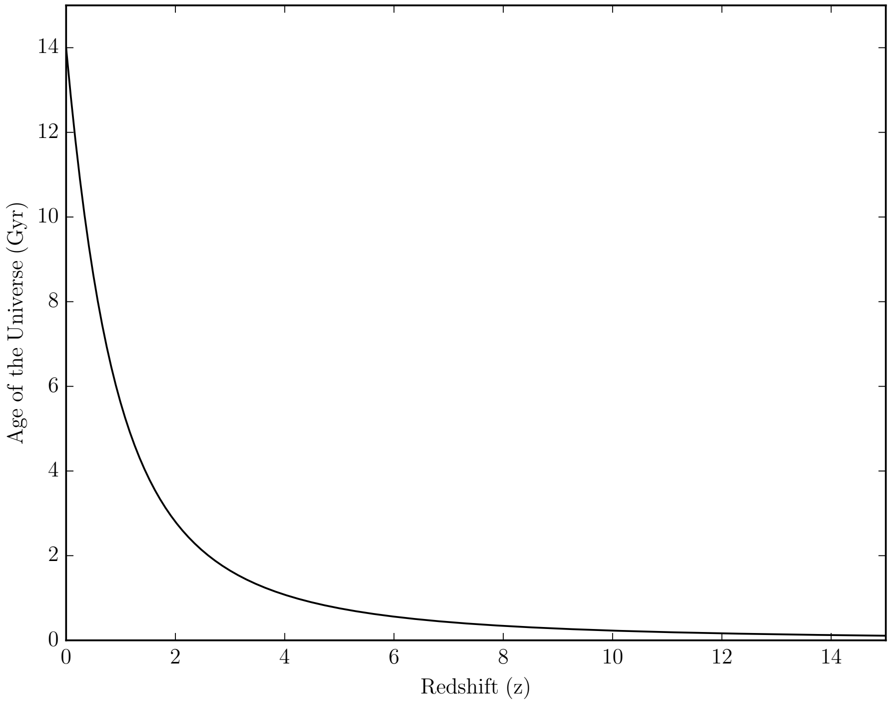

Figure 1: The relation between the Age of the Universe and the value of redshift (z) which describes how much an emission line is shifted in a spectrum due to the expansion of the universe.

observer. The relationship between redshift and luminosity distance is,

$$D_L = c(1+z)\int_0^z \frac{dz'}{H_0 E(z')} \tag{5}$$

where c is the speed of light, z is redshift, H_0 is the Hubble constant, and $E(z)$ is a term than depends on the energy densities of matter and radiation in the universe, as well as the cosmological constant [10].

One can then relate Luminosity distance to the luminosity of an object by,

$$S = \frac{L}{4\pi D_L^2} \tag{6}$$

where S is the luminosity observed per unit area, known as the flux and L is the intrinsic luminosity of the object. The most common unit used for distance in astronomy is known as a parsec (pc) which is defined as 3.26 light years. For example, the diameter of the milky way galaxy is $\sim$ 30kpc.

It is also important to be able to determine angular distances in astronomy so that the distance between two locations in the plane of the sky can be measured. Angular distance also depends on redshift, which is analogous to measuring the arc length of a circle. As the radius of the circle gets larger, or equivalently, the observing plane in the sky is farther away, for a given angle the angular distance increases. However, measuring an angle in the sky between two points can often become extremely small for objects that are very far away from earth. Thus measuring an angle in units of degrees is not practical. Therefore, the units of arcminutes ($'$), and arcseconds ($''$) are used. There are 60 arcminutes in one degree, and 60 arc second in one arcminute. For example, the angular scale at a redshift of 4.3 (the redshift of SPT2349-56) is 6.882kpc/$''$.

2.2 Galaxy Fundamentals

Almost all of the matter that we are able to see in the universe is concentrated in galaxies [11]. Although all galaxies can be described as a gravitationally bound system which contains stars, gas, dust and dark matter, there is also an incredible amount of variety of properties observed in galaxies too. For one, galaxies morphologies can be described by 2 observable properties, the disk and the bulge [11].

The bulge is mostly made up of old dying stars which are much cooler than younger stars due to their lack of available gas to burn, making the stars, and consequently the bulge, a red colour [11]. The bulge itself also is depleted of much of its gas and dust, which is not conducive to allowing new stars to form [11]. The bulge is shaped like an ellipsoid due to the more random motions of the stars within the system [11].

The disk on the other hand has a much flatter profile, where the majority of the matter is confined to one plane [11]. The disk is also the area in which the majority of the young stars are located and has a more blue colour than the bulge because of its higher temperature young stars [11]. These younger stars are more than likely a consequence of the large amounts of gas and dust the disk has, allowing the majority of the star formation in a galaxy to reside there [11]. Both of these properties would collapse under their own mass if it not for the dynamics going on within each system. The bulge is able to withstand the force of gravity due to the motions of the stars within itself. Very analogous to the molecules within a gas, the motion of stars and gas cause a pressure within the galaxy which counteracts the force of gravity [11]. The disk however, stays in dynamical equilibrium with gravity due the centrifugal force that arises from the rotation of the disk [11].

There are 3 types of galaxies observed in the local universe that result from a combination of these two properties. The first, an elliptical galaxy, is one which has no disk component but only consists of large bulge [11]. The second, a spiral galaxy, mainly consists of a disk, but has a small bulge in the center where a supermassive black hole resides [11]. Spiral galaxies get their name for having large spiral arms that extend out from the center of the galaxy. Lastly, irregular galaxies typically do not have a very well defined shape, consisting of neither a bulge of a disk, and are much fainter and smaller than the other 2 types of galaxies [11].

In the distant universe however ($z > 1$), most galaxies seem to have an irregular shape [12]. Irregular galaxies in the distant universe can also be extremely bright, as opposed to the faint ones seen in the local universe. Both the shape and the brightness of distant galaxies is attributed to the vigorous star formation happening at these time periods, which disrupts the galaxies' morphology and makes them intrinsically luminous objects. It is also hypothesized that the irregular morphologies of galaxies in the distant universe are a product of mergers, where two or more galaxies collide [12].

Galaxies in general, are comprised of stars, interstellar medium (ISM) and dark matter. ISM is the gas and dust that lies in between all of the already formed stars. The ISM can be used by the galaxy in order to form more stars, but it also can emit emission lines visible for astronomers to observe and analyze. The dust component of the ISM is extremely important for SMGs, as it's the substance that absorbs UV light emitted from stars and reemits it in the submm regime. Dust is comprised of both carbon and silicon grains with a range in physical sizes (0.01-1.0μm) [13]. Dust is most often formed by the ejection of gas from stars that have gone supernovae (the eventual explosion of a star with a high enough mass). The carbon and silicon atoms condense to from crystals/grains which makes up the dust seen within the ISM [13]. Dark matter is also a very important substance in a galaxy. Dark matter is a non-luminous substance that is theorized by astronomers. It was first introduced after a study of galaxies in the 1950's suggested there should be more mass than astronomers could see due to the rotation of the galaxy. Thus, they suggested there was more matter that simply wasn't light emitting, called dark matter. This idea will be expanded upon and explained fully in §2.5.

2.3 Galaxy Evolution

In order to fully understand how galaxies evolve, its important to first look at the evolution of the universe as a whole. Its widely understood that the universe started in a much denser, hotter and nearly homogenous state than it is today [14]. Ever since the beginning of time, the universe has been expanding, which is known as inflation. As the universe continued to expand over time, it became less dense and thus, less hot, and free electrons in the universe started to combine with nuclei for the first time, creating neutral atoms [14]. Photons in the universe that were initially only being emitted and then reabsorbed by the electrons and nuclei, were starting to be allowed to propagate freely since the universe was becoming less dense [14]. Today, we can observe these freely propagating photons as blackbody radiation, known as the Cosmic Microwave Background (CMB) [14].

Upon the discovery of the CMB, and along with other observations seen in the universe, astronomers started to realize that the universe was mainly dominated by two mysterious substances, dark matter and dark energy [14]. Little is known about both of these substances other than the fact that they make up about 95% of the energy density in the universe, whereas the other 5% is made up of baryons [14]. However, with these initial conditions, astronomers were then able to determine how dark matter density evolved as the universe expanded over time using dark matter only simulations [14]. Over time, the dark matter in the universe started to clump together in gravitationally bound structures known as dark matter halos [14]. These dark matter only simulations have since provided a great framework for astronomers to study galaxy evolution and formation [14].

Modelling galaxy formation is one of the greatest challenges in Astronomy, largely due to the many physical processes that are involved [14]. These processes and their relevance to the evolution of a galaxy are discussed in the following.

Gravity is one of the most obvious and important components in the evolution of a galaxy. From the beginning of a galaxy's life, it is gravity that determines how dark matter clusters in space, and where galaxies will reside [14]. It is also gravity which causes mergers, an event where two or more galaxies collide and eventually coalesce into one [14]. Mergers have a crucial role in the evolution of a galaxy. Most obviously, the morphology of a galaxy changes due to the collision, but it can also cause a large spike in star formation, due to the mixing of the gas within the galaxies [14].

Once large amounts of gas have gravitated in toward a dark matter halo, if large enough densities are reached, nuclear fission will start and stars will begin to form [14]. As more and more stars begin to form, the galaxy's luminosity becomes larger, and its gas clouds become less dense until they are depleted enough that it becomes very difficult to form new stars [14]. Thus, star formation is also an important process in galaxy evolution.

Astronomers soon realized that without any opposition to star formation however, that their models were drastically over estimating the amount of star formation occurring in a given galaxy [14]. It was originally suggested that the energy due to a supernova could perhaps blow some gas out of the galaxy, making the galaxies environment less dense and thus, slowing down the star formation rate [14]. However, we now know that there are many processes that are associated with big stars and supernova that suppress star formation, such as stellar winds and photo-heating of the gas within the galaxy which slows down the star formation rate [14]. All of these processes are known as stellar feedback, which also plays an important role in galaxy evolution.

It is believed that at the center of most galaxies in the universe, such as our own Milky Way galaxy, there lies a supermassive black hole ($M_\odot > 10^6$) [14]. These black holes can drastically change the formation of a galaxy, specifically due to their high-velocity winds, which can blow the ISM right out of a galaxy, and radio jets, which heats up the gas around it [14].

Lastly, the radiation that it emitted from within a galaxy is also important to examine in order to fully understand the evolution of a galaxy. The radiation within a galaxy can heat up its own gas, causing the gas to expand and make it harder to form stars [14]. More importantly, from an observational stand point, the radiation from stars can be absorbed or scattered by gas and dust into different wavelengths, effecting the measured luminosity, morphology, and a number of different observational properties [14].

2.4 Radiation from a Galaxy

Galaxies emit light at pretty much every frequency of the electromagnetic spectrum. Each frequency range emitted from a galaxy tends to be dominated by a specific process or emission source [15]. Thus, analyzing the spectrum from a galaxy in specific regions can explain much about the processes going on within the source [15]. The distribution of frequencies is known as a Spectral Energy Distribution (SED) [15].

The total amount of light that is emitted from a galaxy is known as its Bolometric Luminosity (L_{bol}), which is synonymous with Power (energy per unit time). The value telescopes measure however is known as a Flux (power/unit area), since a telescope will only observe a very small portion of the energy emitted by an object. More often than not, Flux values will also be given as frequency dependent values, F_ν, since it is common for astronomers to only look at the flux at one frequency. The most common unit for Flux in submm astronomy is given by a Jansky (Jy) where 1 Jy = 10^{-26} W m^{-2} Hz^{-1} since the power typically received by submm radiation is so weak. A common unit used in astronomy for Luminosity is Solar Luminosity ($L_\odot$) which describe the luminosity of an object as compared to our Sun.

The SED of a galaxy depends on many different processes [15]. Photons from stars within a galaxy typically emit their light in the UV/optical to the Near Infrared range and thus is a direct link to the star formation history of the galaxy [15]. Galaxies are in general filled with stars with a number of different properties, such as different ages, luminosities and masses [15]. Thus, a typical UV/optical spectrum for a galaxy is just a sum of spectra involving many different types of star [15]. Often when stars are first forming, UV photons from the newly born star will ionize and excite the gas around it producing [HII] emission lines, which is a direct probe of the SFR [15].

Another large portion of the radiation emitted from galaxies comes from the ISM dust [15]. The dust within the ISM of a galaxy is able to absorb the UV light from stars with a high efficiency, and then reemit the light in the infrared range [15]. Dust can often play a vital role in the evolution of a galaxy, such as shielding cold and dense gas from UV photons, allowing them to collapse and form stars [15]. Dust can also act as a catalyst in the formation of H_2 molecules [15].

X-ray emission is mainly emitted from the hot plasma within a galaxy but can also be seen emitting from galaxies with Supermassive Black Holes at the center as well [15]. Radiowaves are mainly a result of free-free emission and synchrotron radiation [15]. Free-Free emission, or “Bremsstrahlung Radiation” is the radiation emitted from a charged particle as it is decelerated by an electric field. To be considered free-free emission however, the deceleration experienced must be collinear with the velocity. Whereas synchrotron radiation describes the emission from a charged particle as its accelerated perpendicular to the direction of the velocity.

A typical model of an SMGs SED can be seen in Figure 2, which spans the Optical to the Radio wavelengths. The model was taken from Da Cunha et al. 2015 which describes an average SMG at $z \sim 2.7$ [16]. The UV emission from young stars, thermal IR radiation from dust particles, and the radio emission from synchrotron and free-free emission are all labeled accordingly.

Galaxies can also have emissions at many different discrete wavelengths, called emission lines. Electrons within the gas of the ISM can be excited by light from stars into a higher energy level. Once the electron leaves the excited state, the energy is reemitted in the form of a photon. The energy of the emitted photon has a unique frequency that can be detected. However, spectral lines are not infinitely sharp structures, instead they follow the profile of a Gaussian. The main reason for this is due to the motions within the gas that emit the spectral line. Not all of the light emitting gas in a given location is all moving at the same speed or direction. Thus, some light may be more/less doppler shifted than the average speed of the gas. This variation of doppler shifts in the emitted light gives rise to a Gaussian shape. Thus, these motions are related to the width of the Gaussian. Specifically,

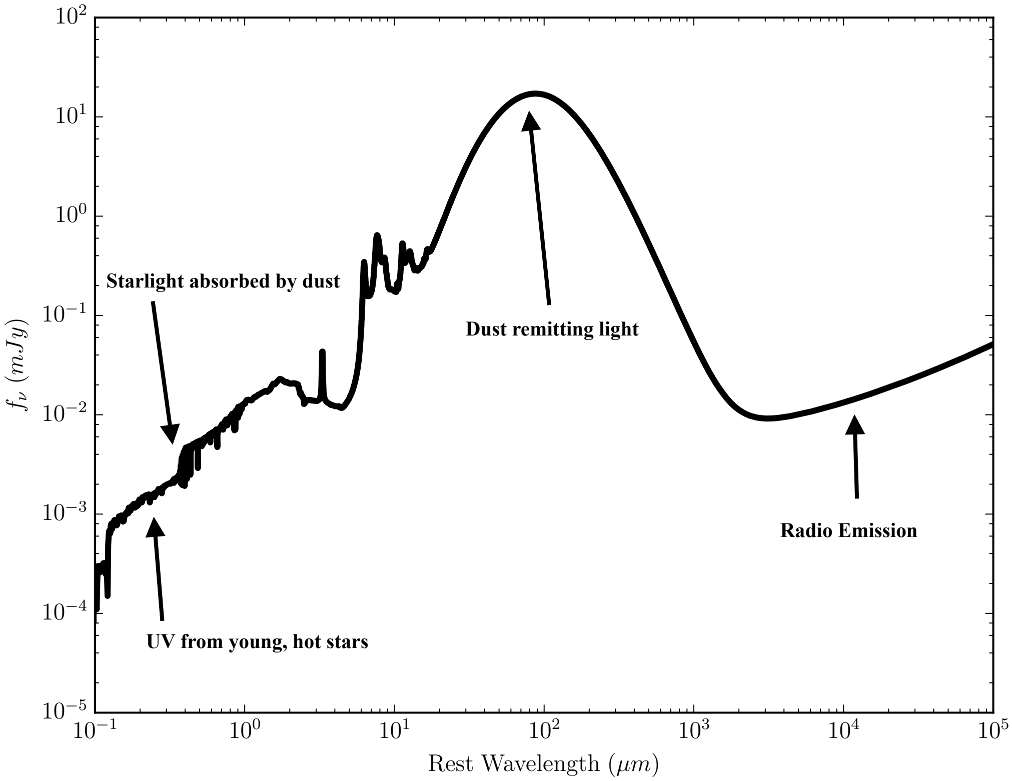

Figure 2: A typical SED for an SMG at $z \sim 2.7$. The SED spans from the optical to the radio wavelengths in the rest frame (before the radiation is redshifted).

the standard deviation of the average motion of the stars and gas within the galaxy is equal to

$$\sigma = \frac{\mathrm{FWHM}}{2\sqrt{2\ln 2}} \tag{7}$$

where σ is the standard deviation, or otherwise known as the dispersion, and FWHM is the Full Width at Half Maximum of the Gaussian distribution. The spectrum of a galaxy will include both emission lines and the SED added together. The part of the SED that is emission line free is known as the "Continuum" of a spectra, which is the shape of the SED.

An effect that can drastically change the measured flux of a galaxy is gravitational lensing. Gravitational lensing occurs due to the bending of spacetime predicted by

Einstein's General Relativity [17]. General Relativity states that the presence of matter can bend spacetime, and that light will follow the path of the curved spacetime as a result [17]. For a sufficiently large mass/gravitational field, light could bend enough such that the rays start to converge after passing the object. Thus, if a large mass is in the line of sight between earth and a light emitting source, the light will bend towards earth making the source to appear brighter than it actually is [17]. This effect is known as gravitational lensing. Figure 3 shows an example of gravitational lensing, where a light emitting source has its radiation bent due to the sun's (or equivalently, any massive object's) gravitational field and later coming to a focus at earth [17].

Not only will the light emitting source seem brighter since more light rays are being detected, but the sources apparent position will also change [17]. When the light reaches earth after being lensed, it appears as if the radiation came from the direction equal to the tangent of its path. Thus, when an image is gravitationally lensed, it tends to appear off centre [17]. If the source lies directly on the line of sight (ie. the line between the gravitational lens and the earth) the light from the source will pass by the gravitational lens equally in all directions and when seen at earth, it will appear as a bright ring known as an Einstein Ring [17]. The galaxies analyzed throughout this thesis are the brightest unlensed objects observed in a 2500 deg^2 survey of the sky, meaning that they are intrinsically very bright galaxies.

2.5 Galaxy Kinematics based on Spectroscopy

Galaxy kinematics based on spectroscopy is an extremely important technique used in order to determine properties otherwise unknown to astronomers. Due to the Doppler effect, if the gas within a galaxy is moving away or towards the earth, it can be observed as a corresponding shift in an emission line. Thus, by tracing the

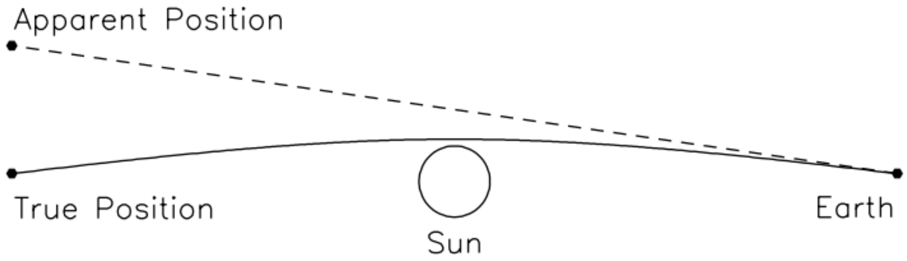

Figure 3: Example of gravitational lensing. The source on the left of the image at its true position emits light that is later curved due to the strong gravitational field of the sun in the center (or equivalently any massive object). That bent light is then focused, or "lensed" on the other side of the object (in this case at earth). The apparent position of the object is the tangent line to the light path.

emission line throughout the galaxy, astronomers are able to directly determine the motions of its gas (the kinematics). The relation between velocity and the change in frequency of a spectral line is given by,

$$\frac{v}{c} = 1 - \frac{f}{f_0} \tag{8}$$

where v is the speed of the gas, c is the speed of light, f is the shifted frequency, and f_0 is the rest frame frequency. This equation comes from a first order approximation of the relativistic doppler formula. This is often used to change the axis of a spectrum from frequency to velocity so that velocity maps can be made. Examples of frequency and velocity spectrums are shown in Figure 4. These emission lines also allow astronomers to make rotation curves of galaxies.

Since the late 1950's, rotation curves (rotational velocity as a function of position) have been acquired from the emission lines of ionized gas within galaxies [18]. What astronomers discovered very early on was that the rotation velocity increased in the center portion of the galaxy but surprisingly flattened out at large radius [18]. This was contrary to what astronomers expected given Newtonian Physics. By equating the centrifugal force to the force of gravity, one can show that the rotation velocity,

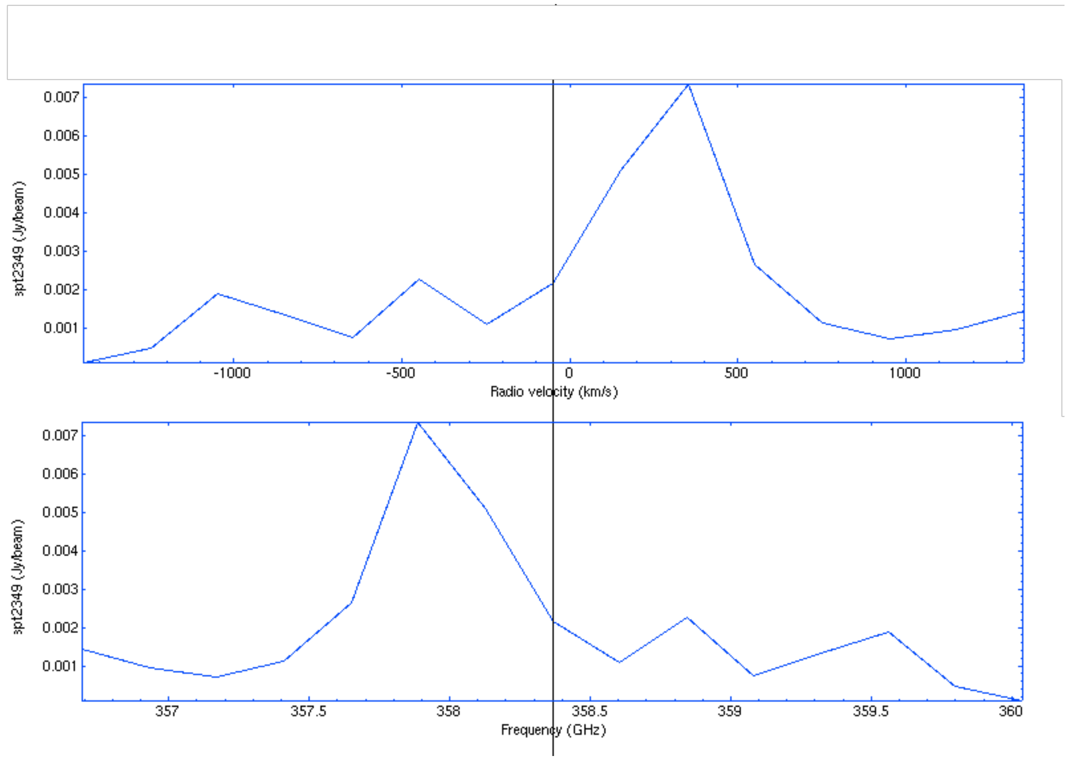

Figure 4: The bottom image shows an example frequency spectrum from the data used in this thesis. Using equation 8, this can be transformed into a velocity spectrum, shown in the top image.

v, of a star for a given radius r, is

$$v = \sqrt{GM(r)/r} \tag{9}$$

where G is the gravitational constant, and $M(r)$ is the mass of the galaxy contained within r. For the central region of the galaxy where the density is approximately constant, $M(r) = \pi r^2 \rho$ where the galaxy is assumed to be a flat disk. Thus, in the central region of the galaxy,

$$v \propto \sqrt{r^2/r} = \sqrt{r} \tag{10}$$

Whereas in the outer regions of the galaxy, the mass stays roughly constant with radius since it is much less dense. Thus, the expected rotation velocity scales as

$$v \propto \sqrt{1/r} \tag{11}$$

In order for the orbital velocity to stay roughly constant with radius, there must be more mass at increasing radius than we are able to detect. It was these findings that led to the hypothesis of dark matter to account for the extra mass [18]. Figure 5 shows the observed rotation curve the galaxy NGC 3198, as well as the assumed halo and disk component rotation curves as well [19].

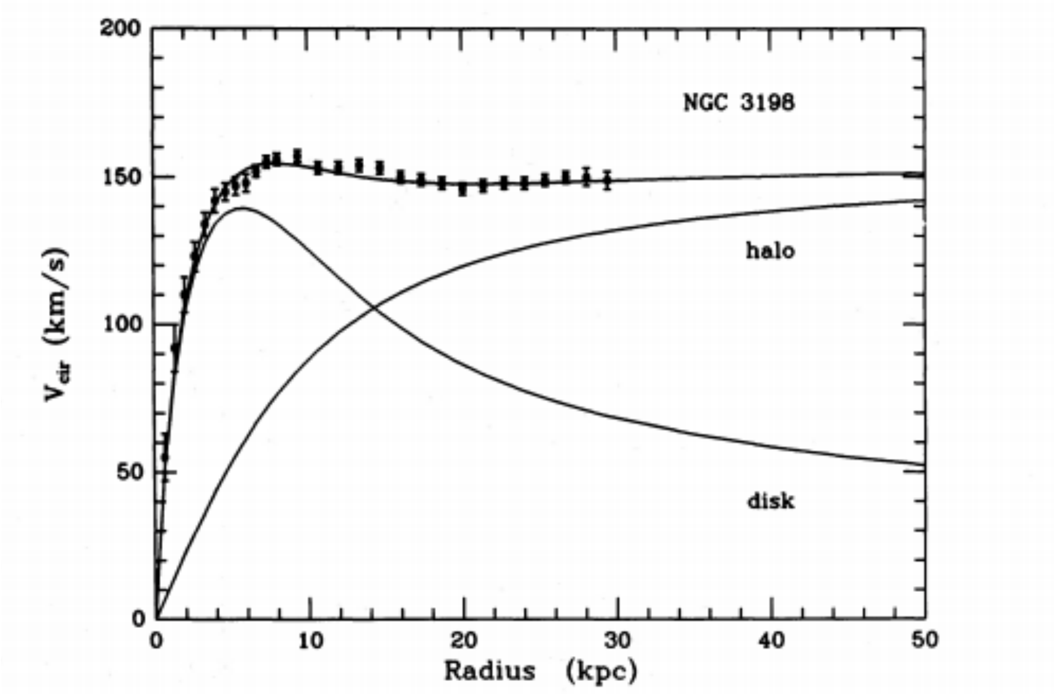

Figure 5: The rotation curve observed for NGC 3198 is shown above (Van Albada et al, 1985). A galaxies rotation curve is expected to fall off after the radius encloses the bulk of the mass. What is observed however, is that the velocity is relatively constant with increasing radius, suggesting that there is mass around the galaxy that isn't being detected. Thus, dark matter was theorized in order to account for this missing mass.

2.6 Using [CII] to probe the properties of a Galaxy

The brightest emission line that arises in the ISM of a galaxy is the [CII] line at 157.74 μm [20]. [CII] is the emission line that occurs due to a transition from the $^2P_{3/2}$ to the $^2P_{1/2}$ energy level in Carbon. [CII] is able to provide us with invaluable insight into the fine structure and kinematics of galaxies due to its intensity and prevalence in high redshift SMGs. [CII] typically carries about 0.1 - 1% of the FIR energy in dormant galaxies and less than 0.1% for ultra luminous infrared galaxies [20]. When galaxies are at redshifts of greater than z $\sim$ 1, the [CII] line is redshifted into the submm regime where it can be observed through Earth's atmosphere. Another advantage of using [CII] is that it appears in many different environments of the ISM due to its low ionization energy, such as warm neutral and ionized medium and cold atomic medium [21].

Thus, due to its diverse origins, [CII] is able to trace out the kinematics over a very large area of the galaxy [22]. By mapping out the emission lines, one can determine the velocity field of the gas within a galaxy. Then from these properties, a galaxy's dynamical mass can be estimated.

2.7 Derived Dynamical Mass Estimates

As mentioned earlier, galaxies prevent all their matter falling inwards through two different dynamical processes: the centrifugal force due to rotation, and the turbulence due to the motion of the gas and stars. The physics of these processes allow us to determine the total mass of a galaxy.

The first mass estimate for objects that stay in equilibrium due to the turbulence of the stars within the galaxy is derived from the virial theorem. The virial theorem states for a stable, self-gravitating spherical distribution of objects, that

$$\mathrm{KE} = -\frac{\mathrm{PE}_{\mathrm{grav}}}{2} \tag{12}$$

where KE is the average kinetic energy of the objects, and $\mathrm{PE}_{\mathrm{grav}}$ is the average gravitational potential energy of the objects [23]. Rearranging this equation for the mass gives

$$\mathrm{M}_{\mathrm{dyn}} = f\frac{\langle v\rangle^2 R}{G} \tag{13}$$

where $\langle v\rangle$ is the average speed of the objects within the galaxy, R the half-light radius of the galaxy, and G is the gravitational constant. The average velocity of the stars within the galaxy is given by the dispersion of the velocity (equation 7). The factor of f in front of the equation depends on the geometry of the mass distribution of the galaxy. Förester Schreiber et al. (2009) give a value for f of 6.7, for dispersion dominated galaxies, that takes into account a wide variety of galaxy mass distributions [24]. Finally, the following equation can be found,

$$\mathrm{M}_{\mathrm{dyn}}[M_{\odot}] = 1.56 \times 10^6 \sigma^2 R \tag{14}$$

where σ is the total integrated galaxy dispersion (in km/s), R is the half-light radius of the galaxy (in kpc) and the $\mathrm{M}_{\mathrm{dyn}}$ is given in Solar Masses ($\mathrm{M}_{\odot}$) which is defined as the mass of an object relative to our sun [25]. The total integrated galaxy dispersion, as previously mentioned, represents the average velocity of the stars within the galaxy. The constant term out front factors in the gravitational constant, the conversions for kpc, km/s and $\mathrm{M}_{\odot}$, as well as the factor of 6.7 mentioned earlier.

The second mass estimate is used for galaxies that predominantly stay in equilibrium with gravity due to rotation. This occurs when the acceleration due to gravity is equal to the centripetal acceleration, namely,

$$\frac{v^2}{R} = \frac{GM}{R^2} \tag{15}$$

where v is the rotational velocity, R again is the half-light radius of the galaxy, G is the gravitational constant and M is the total mass of the galaxy. Rearranging for mass and changing units gives the following result:

$$\mathrm{M_{dyn}}\sin^2(i)[M_\odot] = 2.35 \times 10^5 V^2 R \tag{16}$$

where V is the line of sight velocity in km/s, R is in kpc, and i is the inclination of the galaxy. The inclusion of the $\sin^2(i)$ term is to account for the fact that the observed velocity of the galaxy is the velocity projected along line of sight of the observer, and not necessarily the total rotational velocity of the galaxy. For example, if the galaxy is completely flat when observed, $i = \frac{\pi}{2}$ and $\sin^2(i) = 1$ since the entire rotational velocity is being observed.

Both dynamical mass estimators can be useful, depending on the characteristics of the molecular ISM within the galaxy. Engel et al. (2010) have argued that most SMGs are products of major mergers. If this is the case, then it may make more sense to use the dispersion dynamical mass estimator to get a sensible calculation of the mass, since a major merger would cause much more chaotic and turbulent motions within the galaxy. However, some other groups, such as Swinbank et al. (2011), have found that some rotating disk galaxies are also home to emission from molecular gas. Thus, it seems that each estimator could be relevant depending on the environment within each galaxy.

Förester Schreiber et al. (2009) define a criteria in order to determine whether a galaxy has rotational or dispersion dominated kinematics using the peak to peak observed velocity of the galaxy (total line of sight velocity, ΔV), as well as the integrated dispersion (a weighted average of all emission line dispersion values, σ). They state that based on simulations of many galaxies with different masses, sizes and different ratios of peak to peak velocities to integrated dispersion, the distinction between rotationally dominated and dispersion dominated system happens at $\Delta V/2\sigma \sim 0.4$. Thus, if a galaxy has a $\Delta V/2\sigma > 0.4$, it is considered to be rotationally dominated, whereas if a galaxy has a $\Delta V/2\sigma < 0.4$, it is considered to be dispersion dominated. They also specify that $\Delta V/2\sigma$ are observed quantities that are not corrected for inclination. Otherwise, if inclination corrected and the intrinsic quantities were measured, the criteria would be at $\Delta V/2\sigma \sim 1$.

Hung et al. (2015) also describe a classification criteria for kinematic classes of galaxies, which is based completely on a qualitative analysis of the dispersion and velocity maps. They find that rotationally dominated galaxies have a clear velocity gradient in its velocity map and the dispersion map has a clear peak in the center of the map where the gradient of the velocity map is the sharpest. Whereas for dispersion dominated kinematics, the velocity map could either have a clear gradient or could be more random, and the dispersion map will either show a peak offset from the center or no clear peak at all. Both the qualitative and quantitative analysis of determining whether or not a galaxy has rotational or dispersion dominated kinematics will be useful when determining which mass estimate should be used for each galaxy in our sample.

Chapter 3

Data

3.1 Single Antenna Telescopes

The Atacama Large Millimeter/Submillimeter Array (ALMA) is a telescope that was used in order to acquire the data used throughout this thesis. ALMA is comprised of 66 antennas arranged in different orientations that allows astronomers to observe astronomical objects over a large range of millimeter and submillimeter wavelengths.

Antenna dishes work by bringing electromagnetic radiation to a focus point after reflecting off of a surface. These antenna are very directionally sensitive due to the effect of diffraction [26]. An example of such a situation is shown in Figure 6 (ALMA Partnership, 2017). The top schematic shows the situation of a phase front incident on the antenna from an object in the sky. Since the object emitting the light is so far away from the antenna, they can be treated as plane waves [26]. Due to the parabolic shape of the antenna, any light ray that reflects off its surface then constructively interferes at the focus since all path lengths are the same. This is not the case for any light ray that comes in off axis from the antenna, as shown in the lower schematic of Figure 6. In this case, the phase front path differences to the focus are different, and the light does not add constructively [26]. In addition to this effect, the projected diameter of the antenna from the direction of the off axis phase front decreases as well [26]. This means that the focus will also receive less light, effectively decreasing the power even more [26]. Figure 7 shows the sensitivity of a 12m antenna with respect to angle for an incident phase front of frequency 350Hz (ALMA Partnership, 2017). The Half Power Width Beam (HPWB) in Figure 7 is also commonly known as the "beam size" of a telescope.

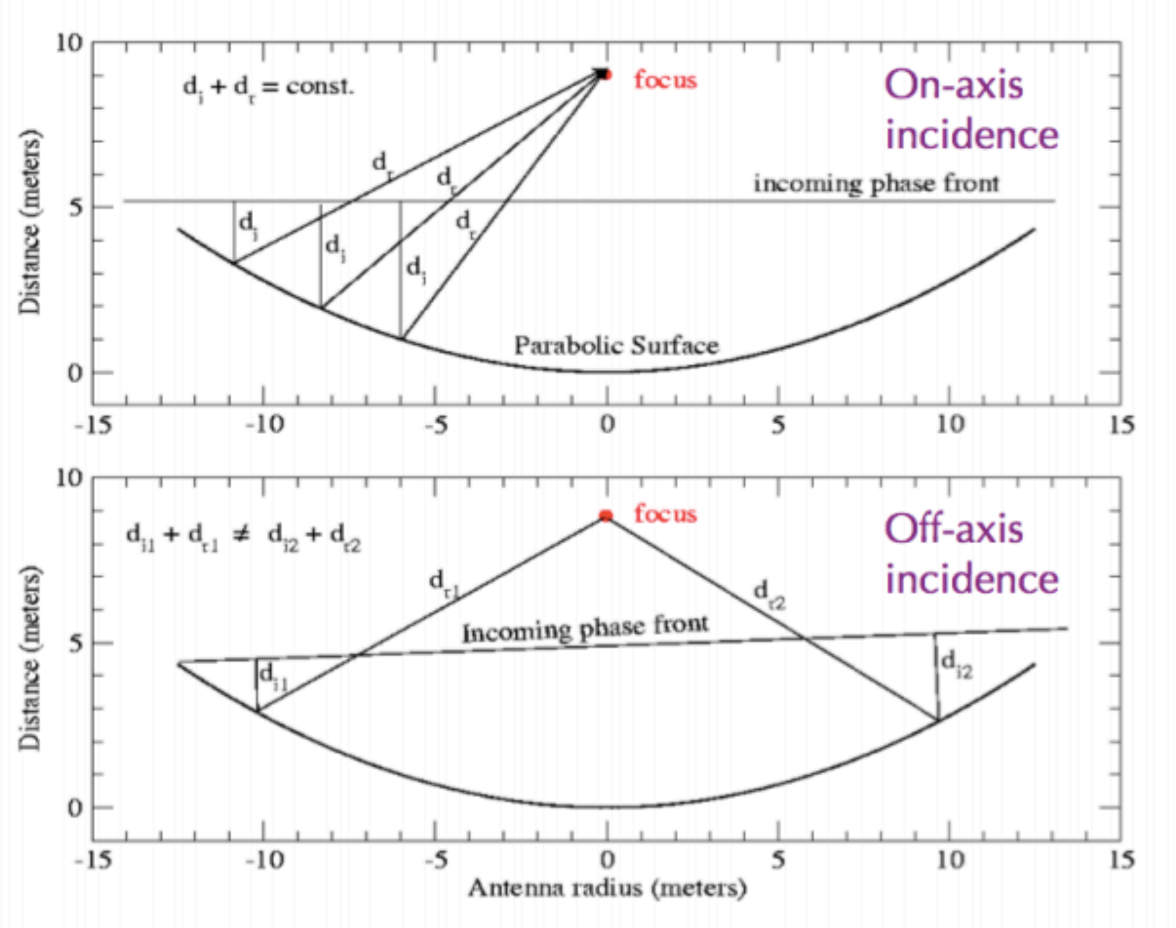

Figure 6: **Top:** An on axis phase front incident on the antenna from an object in the sky. **Bottom:** An off axis phase front incident on the antenna from an object in the sky.

Thus, the beam size of an antenna restricts the resolution of an image that can achieved. For any given antenna (ie., Telescope), the angular resolution of the image

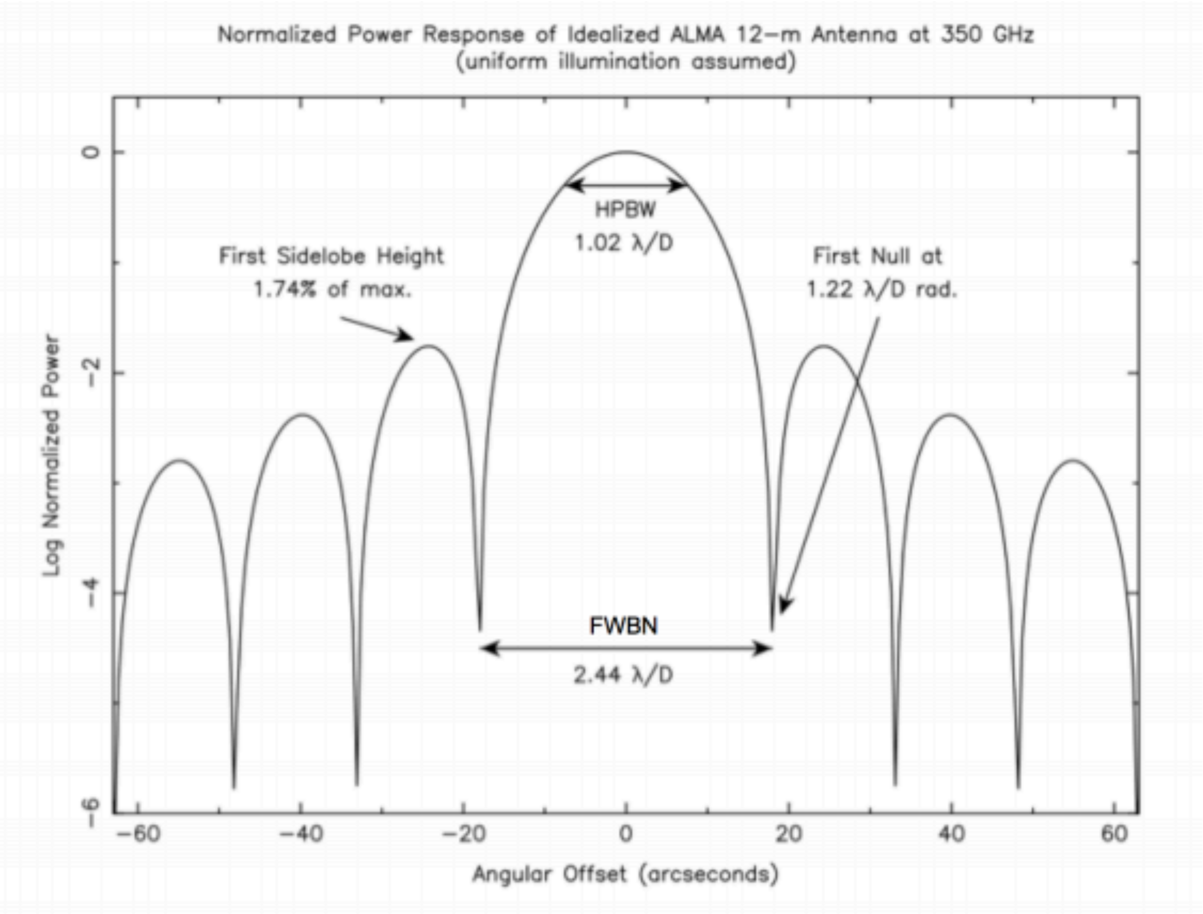

Figure 7: The sensitivity of a 12m antenna with respect to angle for an incident phase front of frequency 350Hz.

is defined by

$$\Delta\theta \propto \lambda/D \tag{17}$$

where $\Delta\theta$ is the angular resolution, λ is wavelength of the light received, and D is the antenna diameter. Therefore, for longer wavelengths, the resolution of the image becomes worse [26]. In particular, typical single antenna telescopes have difficulty trying to observe SMGs due to their long wavelengths. To account for this, one must sufficiently increase the diameter of the telescope such that the resolution becomes reasonable. This can be very challenging, since a larger diameter telescope is more expensive to make and more space is required. However, the diameter can be effectively increased by combining signals received from physically separated antenna, commonly referred to as aperture synthesis [26].

3.2 Aperture Synthesis

Lets again look at the situation above for an on axis phase front incident on the antenna. Imagine that instead of having one large continuous antenna, the antenna is split up into N individual elements [26]. The total voltage measured for the array of antenna would just be the sum of the N individual ones. Knowing this, one could show that the power received by the system can be written as,

$$\langle P \rangle \propto \sum_{i=j} \langle V_i^2 \rangle + \sum_{i \neq j} \langle V_i V_j \rangle \tag{18}$$

where P is Power and V_i is the voltage received from one individual element in the array. The first term in equation 18 is called the auto-correlation term because it only depends on the signal from itself, whereas the second term is called the cross-correlation term [26]. From equation 18, it is clear that the power can be thought of as a sum which for any given value, only depends on 2 elements in the array [26]. There is also no reason for these N elements to be physically connected to one another. In this way, individual antenna can be placed much farther apart than the typical size of a single dish antenna that could be built. Thus, synthesizing a measurement that would be obtained by a large single antenna [26].

Of course, there is also phase fronts coming in from other directions as well, where the path lengths to each individual antenna in a pair is not the same [26]. An example of this situation can be seen in Figure 8, which shows a diagram of 2 antennae observing an incident wavefront coming from a position in the sky, s_0 which is at an angle of θ from the normal [26]. The distance between each of the antenna is b, and is also known as the baseline. The baseline is often written in terms of number of wavelengths, $b = L/\lambda$ where L is the distance between the two antenna, and λ is the wavelength of radiation [26]. The projected distance between each of the antenna from the perspective of the on-axis wave front is $u = b\cos\theta$. The wavefront initially strikes antenna 2 first and then is detected at antenna 1 a time later due to the extra path the wave front had to travel [26]. In order to account for the path length difference between the two antenna for an on axis wavefront, an artificial delay is added to the voltage measured at antenna 2, V_2, such that both voltages are received in the correlator at the same time [26].

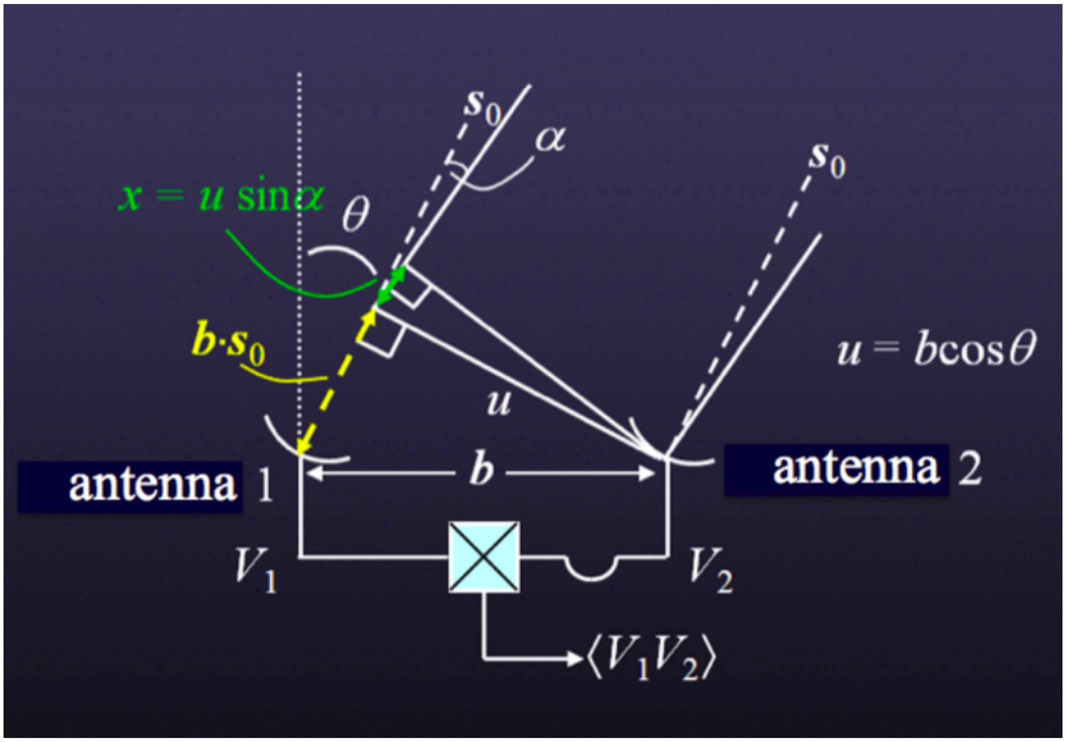

Figure 8: The above image shows the geometry of a wavefront coming from a source in the sky s_0, and striking two antenna.

Now, consider the case where a wavefront is incident on the antenna pair off the axis by an angle α, at a position in the sky $l = \sin\alpha$ (also shown in Figure 8). Again, the wavefront will reach antenna 2 a short time before antenna 1, even with the artificial delay added earlier. This extra path is defined as $x = u \sin\alpha = ul$, which is typically in the units of number of wavelengths, and causes a phase difference between the 2 signals. The difference can be characterized as,

$$V_1 = V_2 e^{2\pi i(ul)} \tag{19}$$

where V_1 is the voltage measured at antenna 1, V_2 is the voltage measured at antenna 2, and the exponential term describes a phase delay that varies sinusoidally as a function of the off axis angle [26]. This situation can be thought as very analogous to Young's double slit experiment, where the path difference of the light causes diffraction on a viewing screen. In this situation however, one can think of the diffraction pattern occurring on the sky. This idea can also be extrapolated into 2-dimensions, where β is the angle off axis orthogonal to α, $m = \sin\beta$ is the orthogonal sky position to l, $v = b\cos\phi$, is the projected distance between the 2 antenna, and ϕ is the angle to the source, s_0, orthogonal to θ [26]. Typically u and v are called "spatial frequencies" of the sinusoids in the directions defined by l and m (ie. E-W and N-S respectively) [26].

Once both voltages are measured, the correlator acts as a time averaging multiplier [26]. Thus, its output is the following:

$$\langle V_1 V_2\rangle = \int\int \langle V_1(l,m)V_2(l,m)\rangle dldm = \int\int \langle V_1^2(l,m)\rangle e^{2\pi(ul+vm)} dldm \tag{20}$$

also, by knowing that $V^2 \propto P$, and $P \propto I$,

$$\langle V_1 V_2\rangle \propto \int\int I(l,m) e^{2\pi(ul+vm)} dldm \tag{21}$$

where I(l,m) is the intensity distribution on the sky. The above equation is in the form of a Fourier transform, thus providing the relationship between what is measured

(V) and the sky intensity (I) [26]. The measurement taken by the correlator is more commonly known as a complex visibility, and can be used to determine the sky distribution using

$$I(l,m) = \int\int \mathcal{V}(u,v)e^{-2\pi(ul+vm)}dudv \tag{22}$$

where $\mathcal{V}(u,v)$ is a complex visibility [26]. The complex visibility is a complex number with an amplitude and phase associated with it, where the amplitude and phase contain information about the brightness of an object on a particular angular scale [26]. As discussed earlier, each one of these visibilities can be thought of as an interference pattern on the sky (Young's double slit experiment). Just as in that experiment, the spacing of the fringes, or equivalently in this case, the angular scale sampled, is dependent on the spacing of the slits/antenna and the wavelength, namely,

$$\text{Fringe Spacing} = \frac{\lambda}{L\cos\theta} \tag{23}$$

Thus, for a given wavelength, the angular scale observed depends solely on the projected distance between the two antenna. In order to recover the true sky intensity distribution, many of these angular scales should be sampled in order to approximate having one large antenna as discussed earlier. For N number of antenna available, there are N(N-1)/2 possible baselines to use, all which can provide different angular scales [26]. As well as having many antenna, the Earth's rotation also allows for more visibilities to be measured as well. Although the actual distance between the antenna never changes, the projected distance between the 2 can depending on where the source is in the sky that's being measured [26]. As example of such a situation is shown in Figure 9. The left hand side of Figure 9 shows all of the projected distances between the different antenna pairs on a "u-v plane". The right hand side shows the corresponding image recovered from the Fourier Transform of the visibilities for a point source. Its clear that as the Earth rotates the point source image becomes much clearer.

Even with the rotation of the Earth however, it still seems like the final image in Figure 9 (bottom right hand panel) still has a lot of interference patterns apparent. This occurs because the system is only sampling a finite number of visibilities and is often referred to as “the dirty image”. In order to account for this, a CLEAN algorithm is used. CLEAN algorithms works by determining the brightest part of the dirty image, then subtracting it and then recording its position and brightness in a new CLEAN file [26]. This is then done iteratively over the dirty image up to a particular cut off level [26]. Finally, the dirty image is convolved with a Gaussian beam, and the residuals of the image are added to the CLEAN image in order to essentially fill in all the gaps [26]. Finally, the resulting image can be used for analysis.

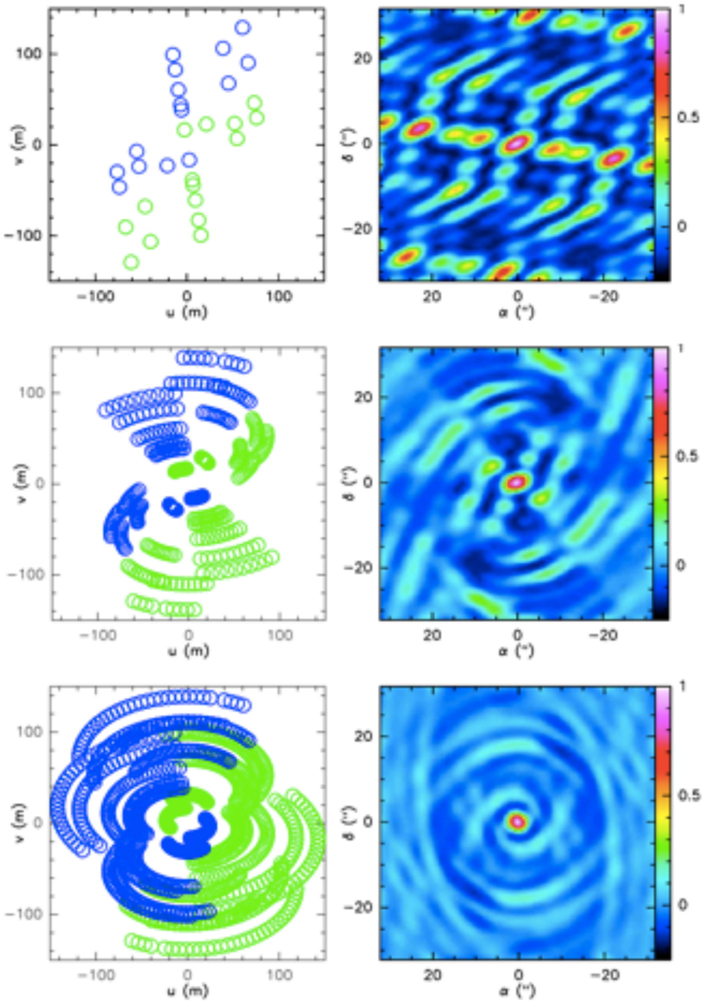

Figure 9: **Left panels:** The plots show the u-v plane, which describes the projected distances between the different antenna pairs in an array (the visibilities sampled). In the lower two panels, the rotation of the earth is utilized, which then allows the array to sample more of the u-v plane. This procedure approximates having one large antenna.**Right panels:** Each plot on the right shows the sky brightness distribution, for a point source, measured by the telescope for each of the corresponding visibilities sampled on the left. As the rotation of the earth is utilized, the image becomes more accurate.

Chapter 4

Motivation

4.1 Protoclusters traced by SMGs

The galaxies analyzed throughout this thesis reside in a structure that seems to be in the early stages of becoming a galaxy cluster. A galaxy cluster is a collection of galaxies that are bound together by the force of gravity. Galaxy clusters first started to form as early as 3 billion years after the big bang and are often seen to have extremely hot (T $\sim 10^6 - 10^7$K) x-ray emitting gas contained within them called the Intragroup Medium (IGrM) [27]. The mechanism which heats this IGrM is still not very well understood, and neither is the epoch at which it starts to form.

The structures that form before a cluster coalesces is known as a protocluster [28]. Protoclusters are typically found at high redshift and in simulations they seem to trace extremely high dark matter densities [28]. SMGs are some of the most luminous and massive galaxies to live in the early universe and due to this were theorized to be markers for the most massive protoclusters in the universe [29]. However, this does not seem to be the case in every scenario. A number of massive protoclusters have been found to contain as little as zero SMGs, whereas some intermediate mass protoclusters have had a few [29]. Some groups (Chapman et. al 2009; Miller et al.

2015) believe this is due to the relatively short life span of the submm luminous phase and thus cannot be treated as a reliable protocluster locator. However, C.M. Casey et al. (2015) argue the opposite might be true. Thus, they suggest that spectroscopic incompleteness of high redshift protoclusters in the submm regime has prevented the discovery of more protoclusters. It's clear that the debate is unresolved and so finding more protoclusters containing a large number of SMGs could help differentiate the views. [29]

4.2 SPT2349-56

The South Pole Telescope (SPT) is a millimeter/submm telescope that is located at the geographic South Pole. SPT provides astronomers with a number of different unique properties such as its selection wavelengths (3.0, 2.0, 1.4 mm), sensitivity and angular resolution, that are ideal for locating galaxy clusters forming at high redshifts ($z > 1$). Gravitationally-lensed sources typically dominate SPT surveys because of the rarity of unlensed SMGs that are bright enough to be detected.

During a 2500 deg^2 survey of the sky, SPT discovered a number of extremely rare and luminous submm sources (number density $\sim 0.04\text{deg}^{-2}$). Most of these objects seem to be gravitationally lensed ($\sim 90\%$). However, the remaining 10% showed no signs of being lensed and thus, may be intrinsically bright objects, or even a collection of unresolved sources. The brightest unlensed source in the survey was SPT2349-56. Further observations using the Large APEX Bolometer Camera at 870 μm showed that SPT2349-56 split into two elongated sources (north and south sources). The southern source was again resolved using ALMA, splitting it again into two different objects which were both found at be at a redshift of $z = 4.3$. Finally, a 385 GHz map was used to look for line emitting galaxies (corresponding to $[\text{CII}]_{1900.5\text{GHz}}$) which found 14 sources at $z \sim 4.3$ [28]. Figure 10 shows twelve of the fourteen galaxies within

SPT2349-56, which are labeled Source A through to L, ordered based on their 1000 μm flux values. The image intensity shown is the average value over all wavelengths observed.

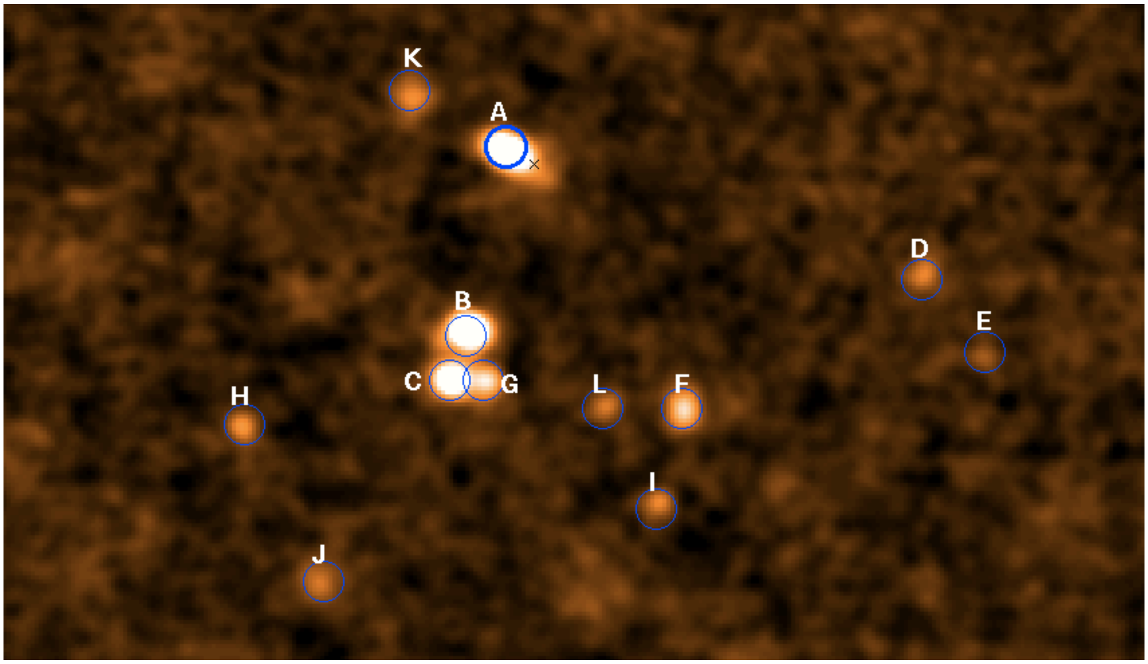

Figure 10: ALMA image of the SPT2349-56 field showing all 12 SMGs. Each source is labeled with their corresponding letter and location is indicated by the black circle. The intensity of the image is an average over the entire spectrum observed.

Miller et al. (2017) analyzed these objects in detail, determining each of the galaxy's Star Formation Rates (SFRs) and gas masses. The SFRs of the galaxies on average are about 500-1000 times greater than our own Milky Way, and are all detected within a 150 kpc projected diameter of one another. This small projected area that they lie in makes it one of the most over dense regions in the known universe, with a space density that is $\sim$ 1000 times greater than the average field space density. Miller et al. (2017) have suggested that due to the extremely high star formation rates and large gas masses, that SPT2349-56 exhibits the properties of a galaxy cluster core that is at an advanced stage of its evolution. This makes SPT2349-56 unique as it is much more evolved than the average field given the age of the universe at the time (1.4 billion years old). This makes SPT2349-56 a truly unique source that could possibly be one of the most dense and evolved fields in the universe. [28]

Protoclusters are the most ideal location to observe galaxies in a uniform set of conditions. All of the galaxies in a protocluster have the same density of environment and are at the same redshift/epoch. Thus, making SPT2349-56 an ideal candidate to study. The data obtained is of sufficient quality and resolution to determine the kinematic properties of the protocluster in Miller et al. (2017), allowing us to look in detail at the astrophysical properties of the galaxies within the cluster. This was done by utilizing the [CII] emission line observed in SPT2349-56 and tracing it throughout the galaxy. Once each galaxies kinematics are determined, the dynamical masses of each source can then be determined.

Currently, simulations have not reproduced the characteristics seen within SPT2349-56. It is very surprising that all 14 SMGs within the protocluster would all be undergoing massive starbursts at the same time, since the lifespan of these structures are so short. Thus, recreating an event similar to this using simulations has been difficult (Lin et al. 2013, Ragone-Figueroa et al. 2018). The question then becomes, is this a typical evolution for these massive early epoch protoclusters, or are we just seeing a brief glimpse of this system's evolution? The simulations used to determine the characteristics and dynamics of systems such as SPT2349-56 have numerous parameters to help constrain it better. Any information added, such as the galaxy's kinematics and total masses, can help to improve the accuracy of the timescales and dynamics of the simulations which is what this thesis sets out to accomplish.

Chapter 5

Methods

5.1 Line Fitting and Kinematics

The data used to preform analysis on throughout this thesis is in the form of a 3D array, or equivalently, data cube. The data cube provides the x and y spatial dimensions of the sky and the z dimension provides the emission spectrum corresponding to each pixel in the map. This data was extracted from the cube and used to analyze each galaxy's emission line. An example spectrum from the data cube can be seen in Figure 11 with the corresponding image of SPT2349-56 below. The intensity of the image displays the average intensity over all observed wavelengths in the data cube. In this case, the emission spectrum has been converted into a velocity spectrum by equation 8, which describes how the galaxy's gas is Doppler shifted. The [CII] emission line can be seen in the spectrum at $\sim$ 370 km/s with a peak value of $\sim$ 8 mJy. The blue 'x' in the image of SPT2349-56 (next to Source A) shows the location in the image where the spectrum was taken from. Each source in SPT2349-56 is indicated by a blue circle with their corresponding letter next to them.

Initially, every galaxy had to be mapped out, determining which pixels to include in our analysis of each galaxy. This was done by determining each pixel in the source

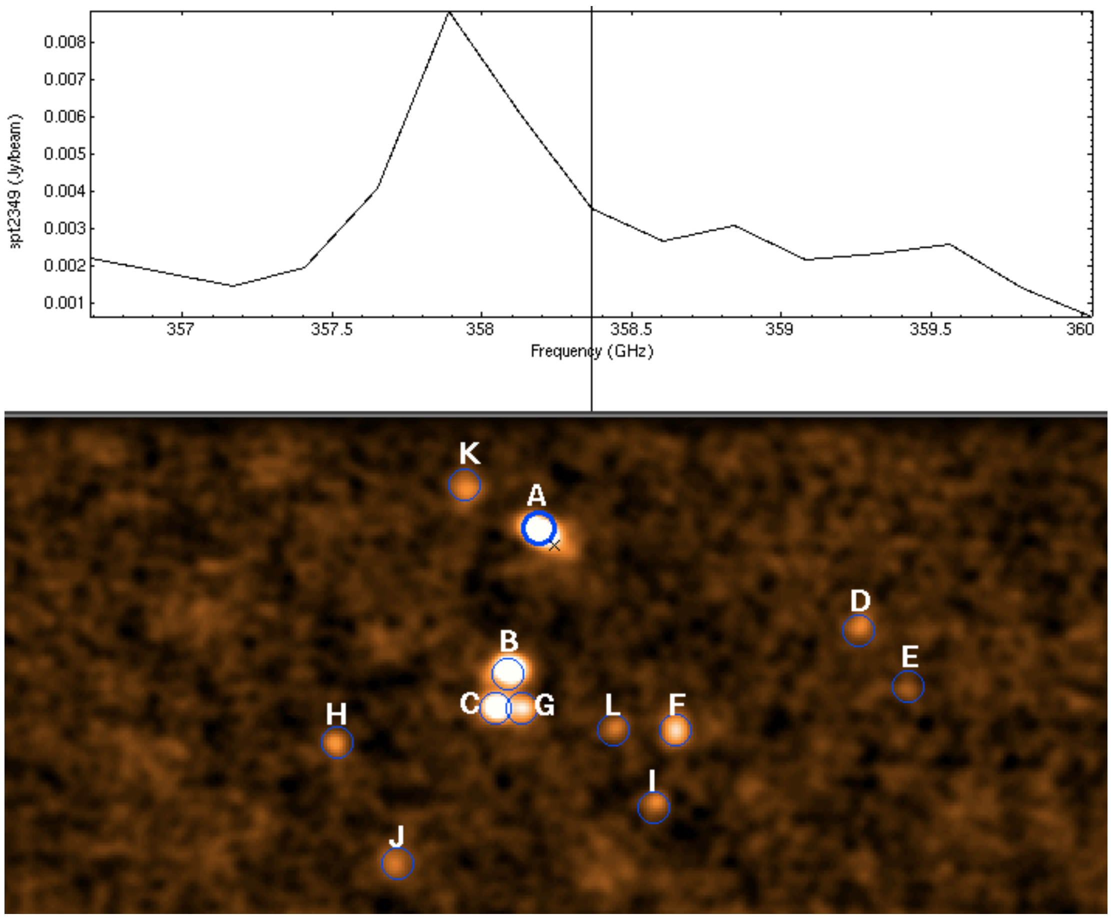

Figure 11: The data cube that contains the emission line data used in our analysis. The labeled map shows the spatial dimensions of the field and the graph above displays the emission spectrum. The current spectrum displayed is from the pixel on the map indicated by the blue x. Each galaxy is indicated by a blue circle and its corresponding letter associated with it. The intensity of the image is an average over the entire spectrum in the data.

that contained a visible emission line. An example of this is shown in Figure 12, which includes every visible emission line contained within Source I. Once it was determined which pixels included a visible emission line, each spectrum was fit with a single Gaussian profile. In each spectrum however, the continuum of the galaxy (ie. the underlying SED) was still present. Thus, in order to get the true area underneath the Gaussian fit, the continuum has to be subtracted from the spectrum. An example of a spectrum with and without the continuum subtracted off can be seen in Figure

13. The continuum was found by adding a constant term to the Gaussian fit, and then subtracting that value afterwards. The emission line was then fit again after being continuum-subtracted to get the true Gaussian profile fit. The emission line shown in Figure 13 also seems to be skewed to the lower velocity end of the spectrum. This is likely an effect due to the beam size of the telescope used. Since the beam size of the telescope has some finite size, each spectrum for a given pixel also contains some information about its surrounding pixels. Thus, if the pixels surrounding the spectrum in Figure 13 are all shifted to a lower velocity due to the doppler effect, we will see that corresponding effect in this spectrum as well. Fitting a Gaussian to this emission line then attempts to recover the true emission line of the galaxy without effects due to the beam.

Three parameters were extracted from each Gaussian profile fit. Firstly, the velocity of the gas at each pixel was measured from the peak of the Gaussian. Then, the dispersion (σ), or equivalently, how much the velocity of the gas fluctuates, was determined directly from one of the fitting parameters (related to the FWHM of the Gaussian by equation 7). Finally, the integrated velocity flux was determined by integrating the total fit Gaussian over the velocity spectrum.

There were a number of different complications associated with this process however. To start, the quality of the data at the edge of the data cube decreases because the antennae response becomes worse as you deviate from its main axis, previously discussed and shown in Figure 7. Thus, for sources that are more towards the edge of the map, it is more difficult to accurately fit their emission lines. An example of this is Source E, shown in Figure 14, where the spectra of each pixel is very noisy and so it is difficult to fit a Gaussian profile properly. Also, when fitting emission lines near the edge of a galaxy, the emission line becomes very weak and the fitting program has a very hard time trying to find the correct data to fit. Sources B, C and G are especially interesting, since their emission lines seemingly overlap due to their

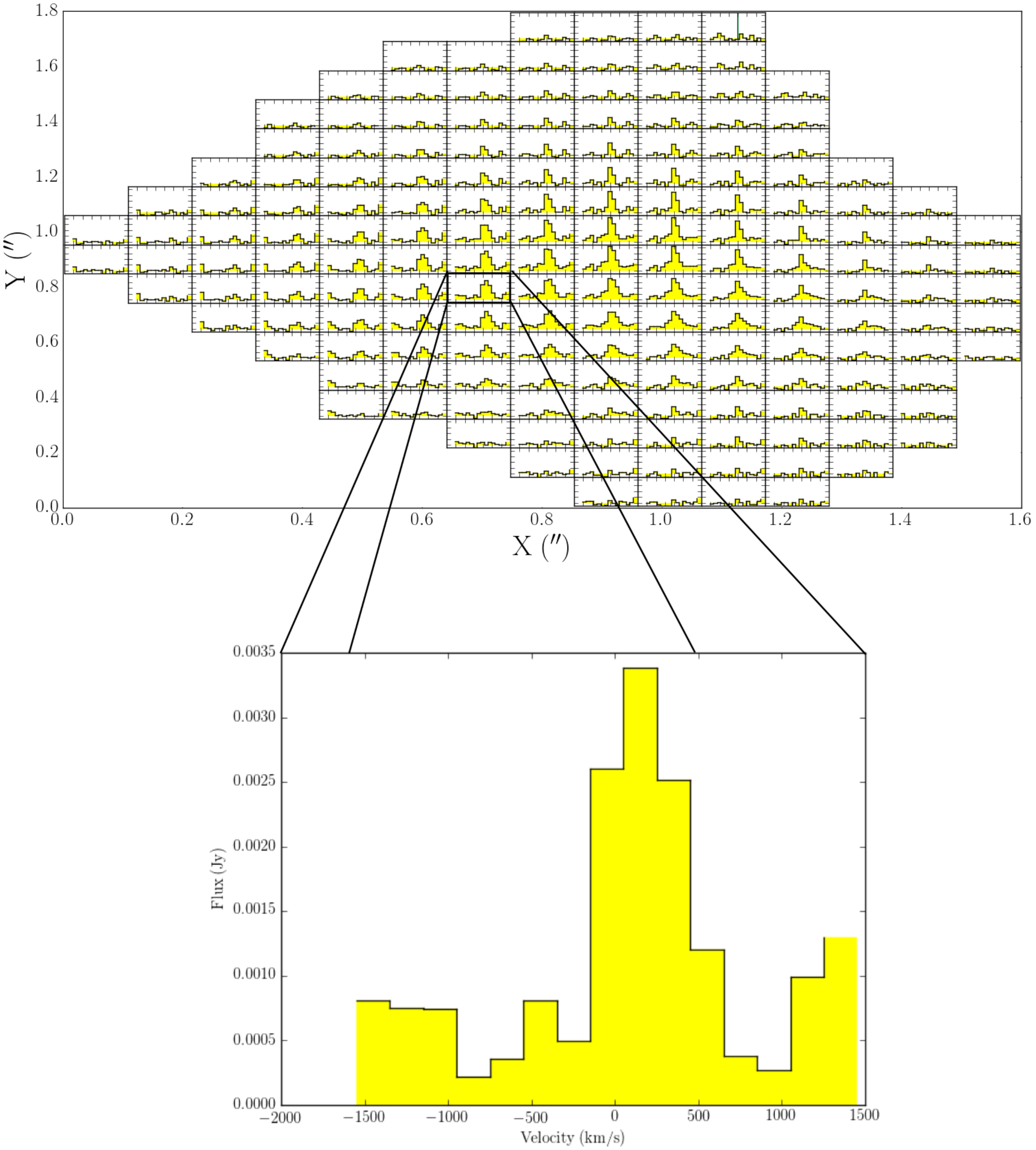

Figure 12: The top image is an example of a spectral map, which displays the spectrum in the location of its corresponding position in the galaxy. Then a zoomed in example of one of the spectra in the map is shown below. The spectra clearly shows the [CII] emission line centered around $\sim$ 200km/s. These spectra maps are useful in order to determine which pixels in the galaxy have visible emission lines. Once it is determined which pixels have emission lines, each one can be fit with a Gaussian profile.

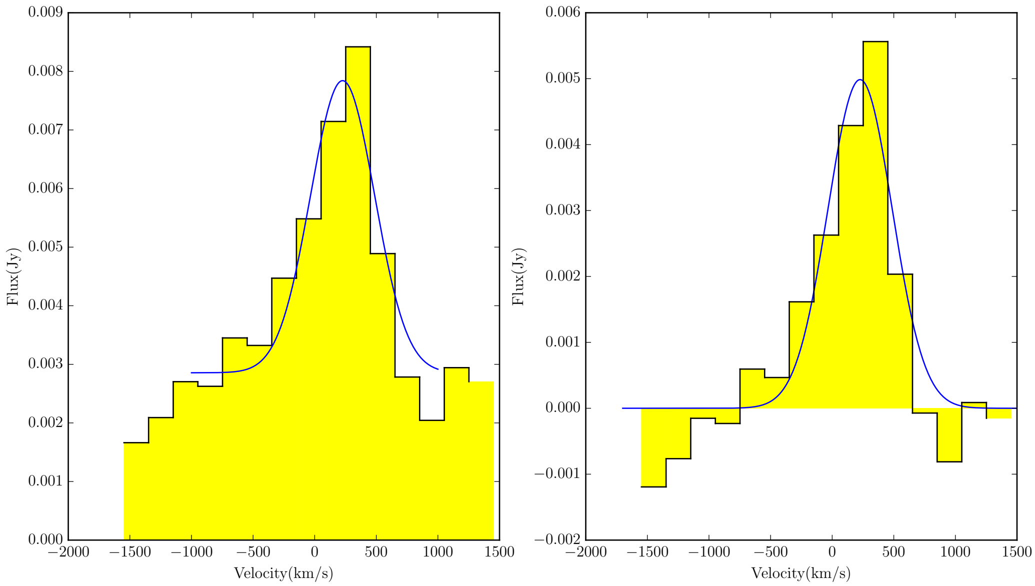

Figure 13: **Left:** The yellow bars represent a typical emission line spectra observed for a single pixel within one of the galaxies in SPT2349-56. The blue line shows the Gaussian fit to the emission line. This is an example of a spectra that is has not yet had its continuum subtracted. **Right:** The spectra of the same pixel after the continuum has been subtracted off to get the true fit to the emission line.

proximity to one another, and separating them is difficult. Also, owing to the fact that the beam size of the ALMA telescope has some finite size ($5''$), it will smear out the actual sources, making it more difficult to clearly spatially resolve each source. Thus, all sources will seem more extended than in actuality.

Once all the fittings were done and the parameters were extracted, each value for the velocity, integrated velocity flux and dispersion were sorted into a 2d plot, matching their pixel locations in the galaxy. This shows what the line of sight velocity is in the galaxy (velocity map), the variation in the line of sight velocity (dispersion map) as well as the strength of each emission line (integrated velocity flux map). An example of Source A's maps are shown in Figure 15. All other maps are shown in Appendix A.

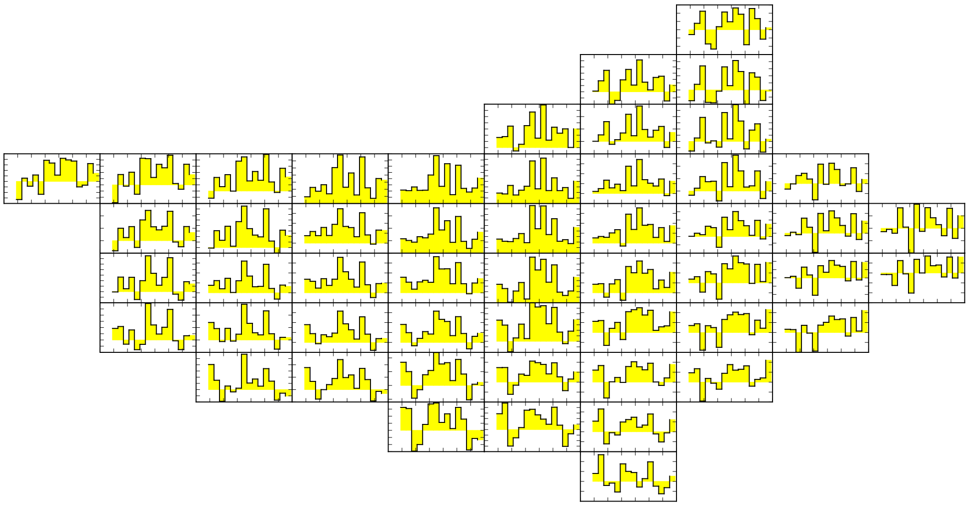

Figure 14: The spectra map of Source E. The spectra for each pixel is much noisier than other galaxies in SPT2349-56 because Source E is so close to the edge of our data, where the telescope's response is much weaker and thus, less accurate.

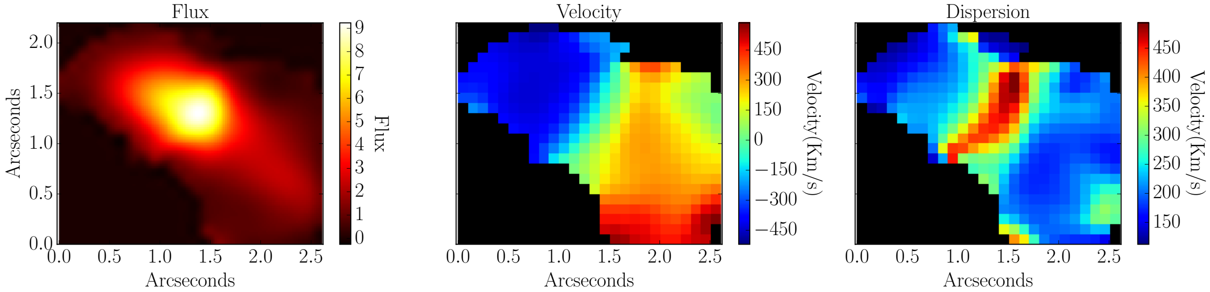

Figure 15: **Left:** The integrated velocity flux map of Source A, created by integrating the emission line of each pixel within the galaxy. The image has also been smoothed with a Gaussian filter. **Middle:** The velocity map of Source A, created by extracting the velocity value at the peak of the fit Gaussian for each pixel. **Right:** The dispersion map of Source A, created by extracting the dispersion parameter used in the fit to each emission line.

Chapter 6

Results

6.1 Physical Characteristics of Sources

In order to further characterize each source, the velocity maps were used in order to derive rotation curves. Rotation curves are vital to understanding fundamental properties of each source. The rotation axis (major axis) of each galaxy was found by slicing through the velocity map at different angles and generating rotation curves for each slice (for every pixel the slice cuts through, the velocity measurement is extracted and plotted versus its position in the galaxy.) Then, the angle at which the most reasonable rotation curve is obtained (ie, the line in which the velocity field of the galaxy is most symmetric/mirrored as well as the largest velocity spread) is chosen as the slice. This symmetrization process of determining the rotation axis of the galaxy is not as rigorous as full disk model fitting that other groups have done (Jones et al. 2017) but is out of the scope of this research. An example of such a rotation curve is shown Figure 16.

The bottom image of Figure 16 shows the velocity field of the Source A along with the slice through the field chosen to make the rotation curve. The top figure then shows the rotation curve generated by the slice. There also seems to be an unexpected bump in the rotation curve from $\sim$ -9 to -7 kpc, as the rotation curve is expected to flatten out with increasing distance. This is most likely due to the issue of fitting lines at the edge of a galaxy as mentioned previously. As the line moves further from the center of the galaxy, the line becomes weaker and harder to fit properly. Thus, some galaxies seem to have high velocity edge regions in their velocity map that aren't physical. The peak to peak velocity measurement from each of the rotation curves can then be used in determining the dynamical mass of each galaxy, from equation 16. For all the galaxies within SPT2349-56, the inclination is unknown, and so an average value of $i = \frac{\pi}{4}$ is used.

However, before the dynamical masses of each galaxy could be estimated by equation 16, the half light radius of each of the galaxies had to be determined. The half light radius was determined by analyzing the intensity profiles along the major axis of each galaxy. An intensity profile shows the integrated velocity flux versus position in the galaxy. The intensity profile for Source B is shown in Figure 17 as an example. The intensity profiles were created by slicing through the 2D integrated flux map and extrapolating all the values along the slice. Each intensity profile was fit with a Gaussian, and the Half Width Half Maximum of the Gaussian was extracted which is equivalent to the half-light radius. However, this measurement still does not give us the true size of the galaxies because as said earlier, due to the finite beam size of the telescope, the galaxies will be smeared out and be perceived as larger than they actually are. In order to determine the actual size of each source, we used the following equation to deconvolve the objects:

$$\text{Deconvolved Size} = \sqrt{(\text{observed size})^2 - (\text{beam size})^2} \tag{24}$$

which comes from combining errors in quadrature.

The dynamical masses of each of the galaxies was then calculated under the assumption that they are rotationally dominated objects by equation 16. However, it is

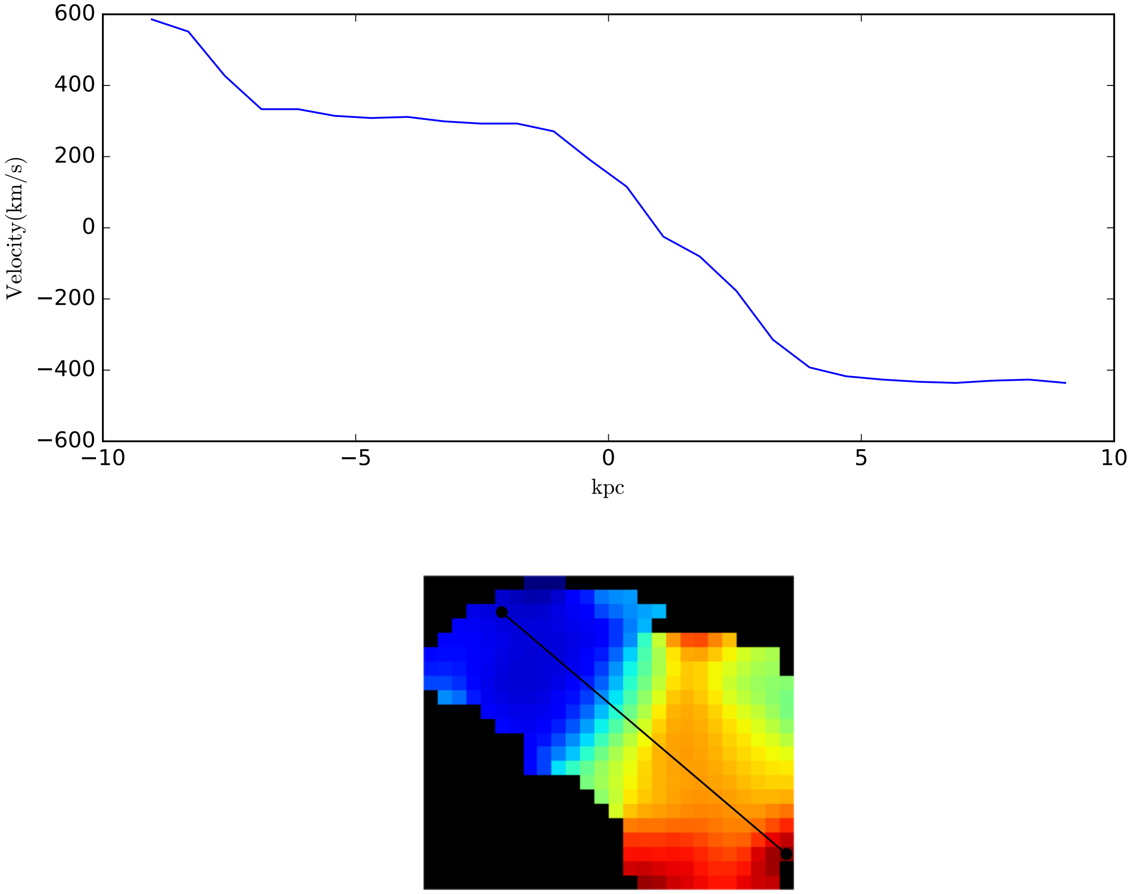

Figure 16: **Top:** The rotation curve of Source A. The curve seems to flatten out in the outer regions of the galaxy, implying that we are mapping out to the dark matter halo that surrounds the galaxy. **Bottom:** The velocity field of Source A. The black line shows the assumed axis of rotation for the galaxy determined by the symmetry of the velocity map. For each pixel the line slices through, the value is taken and used in order to create the rotation curve.

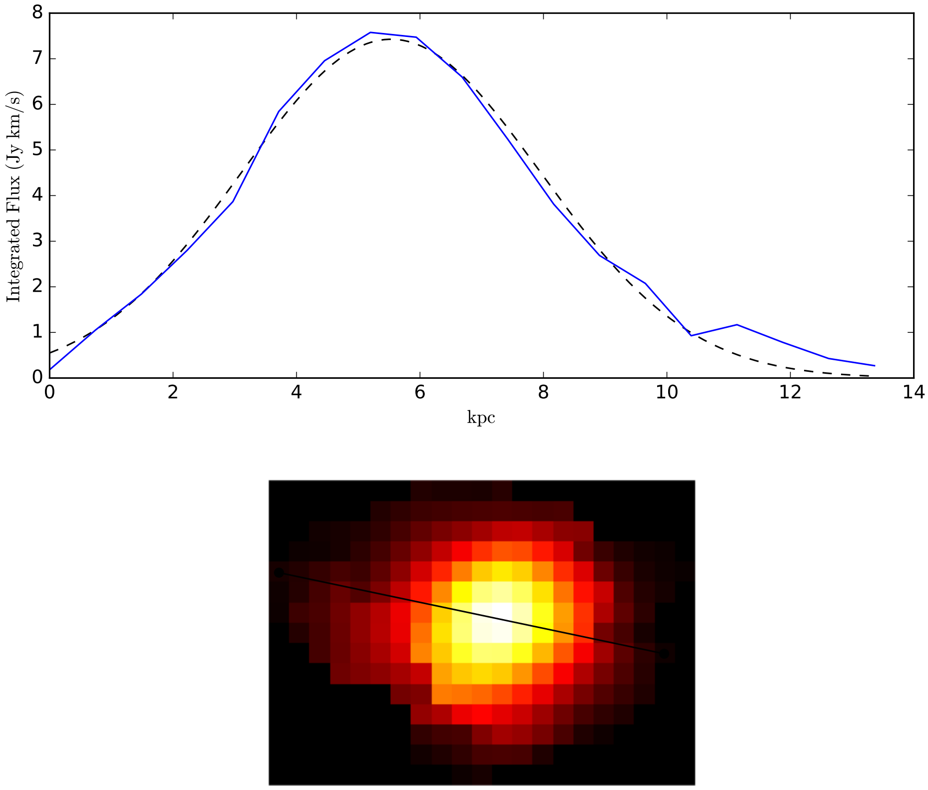

Figure 17: **Top:** The blue line shows the intensity profile of Source B, created by slicing through the integrated velocity flux map, extracting the values along the slice and plotting them versus the position in the galaxy. The dashed black line shows the Gaussian fit to the data. This fit then allows the radius of the galaxy to be determined from the Half Width Half Maximum. **Bottom:** The integrated velocity flux map of Source B. The black line through the map is the slice through the galaxy used in order to create the intensity profile.

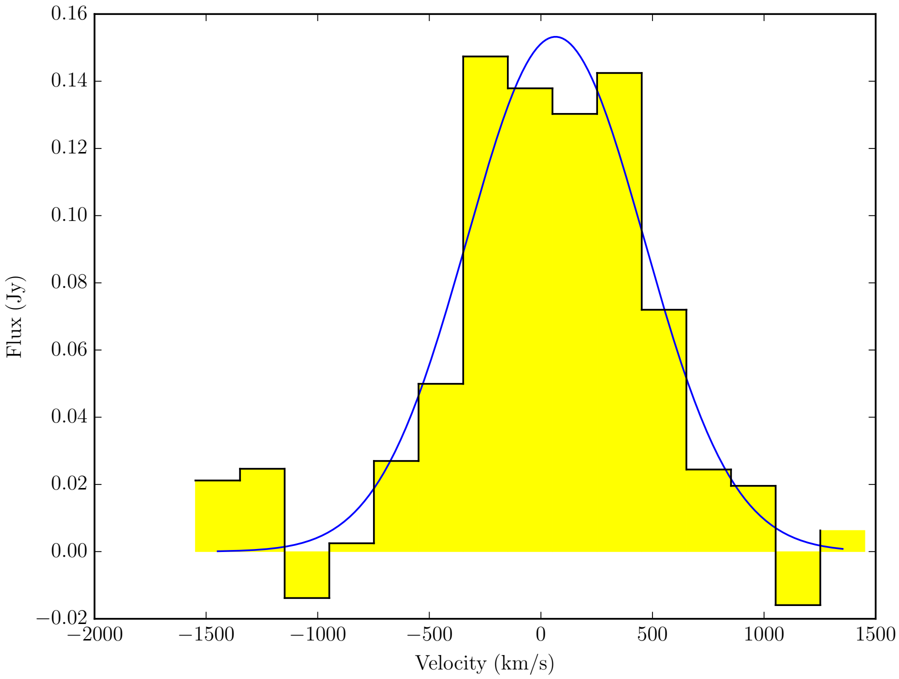

Figure 18: The Total integrated spectrum for Source F. All spectra that were included in the analysis were summed together and fit with a Gaussian in order to determine the total dispersion of the source.

possible some of the galaxies are more dispersion dominated systems and equation 14, the dynamical mass estimate for a turbulent galaxy, should be used instead. Thus, the total integrated dispersion (σ) for each of the galaxies must also be determined.

In order to determine σ, the spectrum from each pixel associated with a particular galaxy was added together and then fit with a Gaussian. The dispersion value for that fitted Gaussian was then used in equation 13 and are listed in Table 1. An example of the summed spectra for Source F can be seen in Figure 18.

Finally, using these derived parameters, we were able to calculate M_{dyn} for each source. Both mass estimates calculated are tabulated in Table 2 and plotted against one another in Figure 19. The dashed line in Figure 19 shows where both of the estimates are equal. The plot doesn't seem to suggest that one mass estimate is dominate over the other.

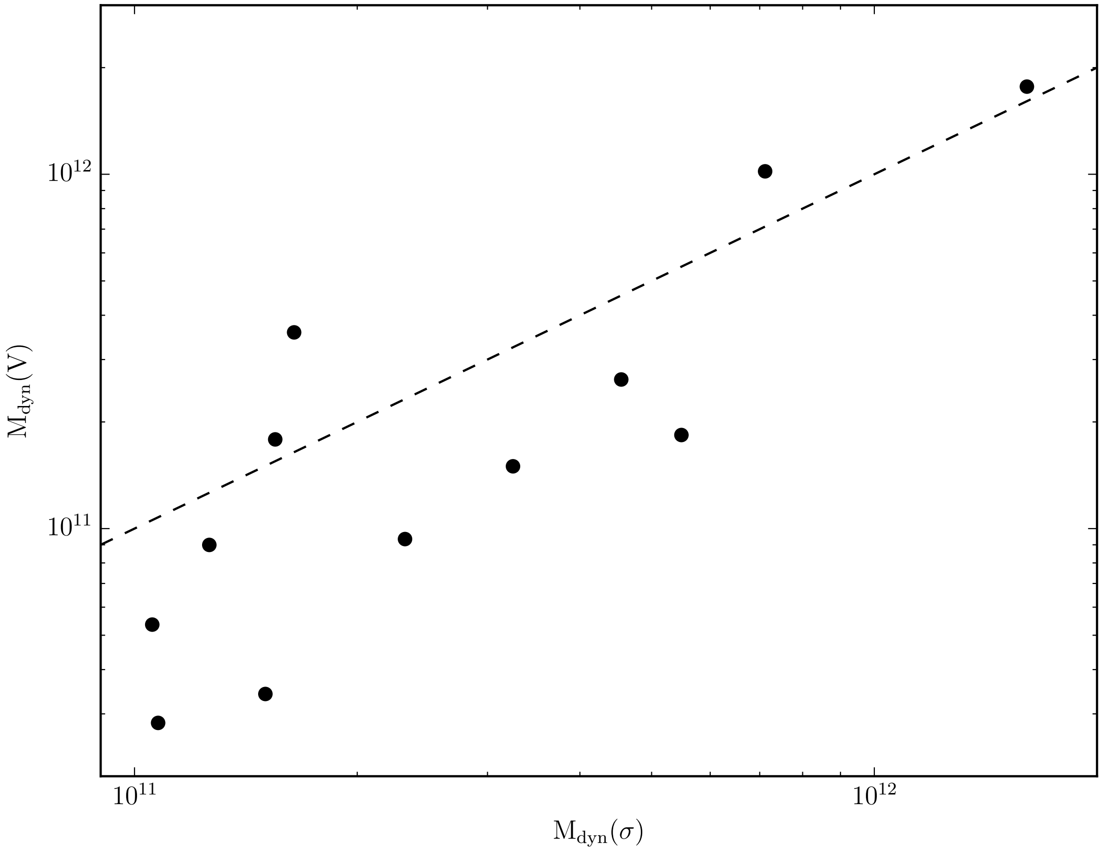

Figure 19: The above plot shows both of the dynamical mass estimates for each of the 12 sources plotted against one another. The dotted line shows the value in which both estimates are equal. The plot doesn't seem to suggest that either mass estimate is dominant over the other.

However, it would be useful to look at whether or not one of the estimates would be better than the other for a given galaxy. As mentioned earlier in §2.7, Förester Schreiber et al. (2009) define a criteria to determine what kinematics are dominating a galaxy based on the observed quantity of $\Delta V/2\sigma$. Thus, in order to determine which mass estimate is more appropriate, this criteria was measured for every galaxy in this thesis. The $\Delta V/2\sigma$ value for all the galaxies in this sample are shown in Table 2. $\Delta V/2\sigma$ is also plotted against SFR in Figure 20, along with all the galaxies in Förester Schreiber's sample as well. The black horizontal line in Figure 20 shows the transition criteria used by Förester Schreiber et al. (2009) to determine whether a galaxy is more rotationally ($\Delta V/2\sigma > 0.4$) or dispersion ($\Delta V/2\sigma < 0.4$) dominated.

By looking at Figure 20, its clear that based on the criteria given by Förester Schreiber et al. (2009), none of our galaxies should be dispersion dominated. It's possible this is due to the fact that some rotation curves were fit to the galaxies in our sample that clearly don't have a well defined velocity field. An example of this is Source L (shown in Appendix A as Figure 41). All sources that do not have a well defined rotation axis are flagged in Figure 20 with a red circle. Some of the sources also have edge regions in the velocity field that change very drastically, possibly raising the ΔV value higher than it really is (as previously discussed for Figure 16). This is most likely due to fitting errors where the emission line signal becomes weak and harder to fit properly. Thus, these reasons may be why it looks like all of our galaxies are rotationally dominated, given Förester Schreiber's $\Delta V/2\sigma$ metric, even though some are clearly not, given the qualitative measures described in §2.7. Thus, each galaxy will need to be looked at individually in order to determine their kinematic properties.

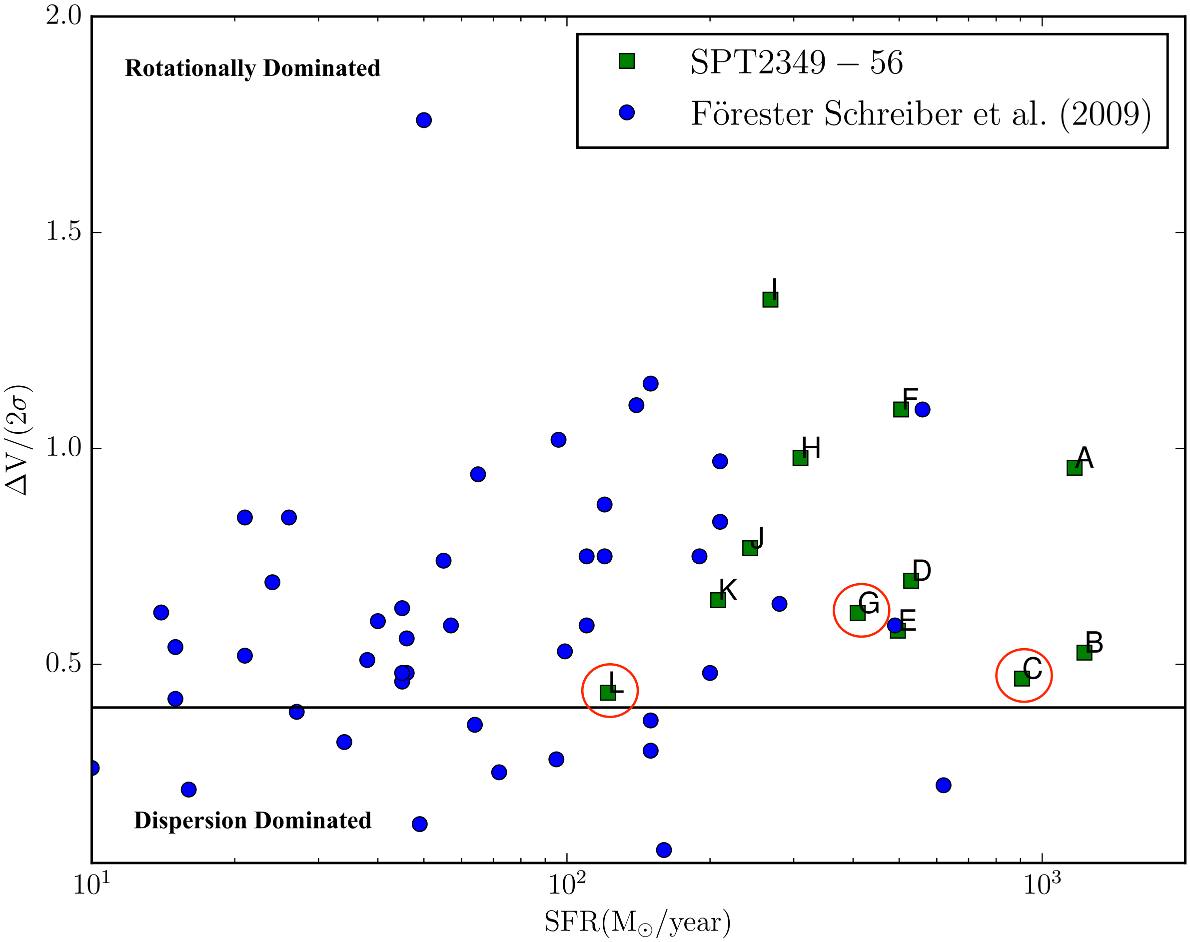

Figure 20: The ratio of $\Delta V/2\sigma$ versus SFR. The green squares show all 12 of our galaxies and are labeled accordingly. The blue dots show the sources from the SINS sample analyzed in Förester Schreiber et al. (2009). The black line is drawn at $\Delta V/2\sigma = 0.4$ and is the boundary determined by Förester Schreiber et al. (2009) in order to differentiate whether or not a galaxy was rotationally or dispersion dominated galaxy. The sources that do not have a well defined rotation axis but were forced one regardless to obtain a ΔV value are flagged with a red circle around them.

6.2 Notes On Individual Sources

This section is aimed at trying to identify some key characteristics of each galaxy. Specifically, the main objective will be to understand whether or not each galaxy is dispersion or rotationally dominated based on its velocity and dispersion maps, as well as comparing our findings to the $\Delta V/2\sigma$ criteria. Thus, ultimately trying to further understand how to best characterize the $\mathrm{M_{dyn}}$ of a system. The rotation axes of each galaxy will also be looked at, and whether or not trying to determine the axis in a semi-automated way (choosing the highest velocity gradient slice) or manually tweaking the axis is required for this analysis. This analysis will also allow us to look at whether or not there may be companion galaxies complicating the velocity fields, and so to not include them in our analysis. All of the source maps can be found in Appendix A, and rotation curves in Appendix B for reference.

Source A

The velocity field for Source A seems to have a very obvious rotation axis from the NE to SW section of the galaxy which also aligns with the maximum and minimum values of its velocity field. Source A contains the largest peak to peak velocity of all 12 sources and seems to be rotationally dominated due to its smooth velocity gradient and centralized dispersion peak. Calculating its $\Delta V/2\sigma$ results in a value of 0.96. Source A is also the spatially largest galaxy in our catalog as well, with a radius of 4kpc (before accounting for beam smearing). The rotation curve seems to clearly level off, leading us to believe we are mapping out the entire rotation curve of the source.

Source B

Again, the velocity axis seems obvious by observing the symmetric nature of the velocity field (E to W), however it does not align with the maximum and minimum values of the field. The rotation curve seems to indicate that the source has been mapped out right to the point where the rotation curve would flatten out. Source B initially seems to be rotationally dominated given its symmetric velocity field, however the dispersion map does show a fairly large amount of turbulence in the galaxy, with a peak that is clearly off center. Thus, Source B seems to have properties of both rotational and dispersion dominated kinematics. Calculating its $\Delta V/2\sigma$ results in a value of 0.53.

Source C

There is no real sign of rotation in the galaxy, however a rotation curve is fit to the estimated major axis of the source for completeness. It seems very plausible Source G could be contaminating the velocity field as the 2 sources are right next to each other ($\sim$ 6kpc separation). The low velocity pixels at the end of the galaxy may be arbitrarily raising the peak to peak velocity calculation and thus were excluded from the measurement. Edge region pixels that have a jump are often suspect since it could just be small warp that does not actually imply a larger $\mathrm{M}_{\mathrm{dyn}}$. There is also very clearly a lot of dispersion throughout the entire dispersion map, suggesting Source C is mostly dispersion dominated. Calculating its $\Delta V/2\sigma$ results in a value of 0.47.

Source D

The axis of rotation is less obvious here but again by looking at the symmetry of the system it was determined as NW to SE, however it does not directly line up with the minimum and maximum values of the field. The data used to calculate the maps of Source D are much noisier due to the fact that the galaxy is positioned near the edge of the data where the telescope response is much worse. Thus, the shape of the galaxy is much less well defined. However, most of the velocity map looks to be well behaved, except in the south region where the velocity starts to increase again. The dispersion map of the galaxy shows that the peak is off center, but it does coincide with the max integrated flux value. Source D appears to have the characteristics of both dispersion and rotationally dominated kinematics, however due to the poor quality of the data it is very hard to tell. Calculating its $\Delta V/2\sigma$ results in a value of 0.69.

Source E

Again, Source E is near the edge of the data cube and thus, the shape of the galaxy is much less well defined due to the low response of the telescope. That being said, the rotation axis of the galaxy is very clear (E-W) and lines up very well with the maximum velocity gradient. The peak dispersion also seems to be centered in the galaxy, which would make us believe it is rotationally dominated, although it is hard to tell with certainty. Calculating its $\Delta V/2\sigma$ results in a value of 0.58.

Source F

Source F has a very clear velocity map and rotation axis that runs completely N-S even though it is not aligned with the minimum and maximum velocity values. Source F seems to be very strongly rotationally dominated. However, there also does seem to be a high velocity (red) source, offset from the main galaxy. It is possible that this offset source is another galaxy undergoing a merger with Source F. Calculating its $\Delta V/2\sigma$ results in a value of 1.09.

Source G

Source G is difficult to isolate due to its close proximity to Source C which is larger and likely contaminating the spectrum of the galaxy. It does not seem to have a very well defined rotation axis, however a line was fit to the velocity map regardless. The Dispersion map also suggests that is may be dispersion dominated since the peak is so broad. Calculating its $\Delta V/2\sigma$ results in a value of 0.62.

Source H

Source H has some sort of a defined velocity field, however, it is not intuitive as to whether or not it is dispersion or velocity dominated by looking at the velocity field. The dispersion map does have a maximum fairly close to the center of the integrated flux maximum, although again by eye it is hard to tell exactly which process is dominating at galaxy. Calculating its $\Delta V/2\sigma$ results in a value of 0.98. The rotation curve of the galaxy hasn't seemed to level off yet, thus we may not be imaging all of the dark matter halo surrounding the galaxy. The axis of rotation is also not aligned with the maximum velocity gradient.

Source I

Source I has a well defined velocity field, although it doesn't show much symmetry, leading us to believe it may not be a disk galaxy. It's possible the rotation axis of the galaxy runs from SE to NW, however the axis chosen ($\sim$ E to W) such that the axis runs through the high dispersion area in the source as if it were a disk. Its possible the best explanation for this source is that its a poorly resolved merger. It seems as if Source I is rotatoinally dominated due to the smooth velocity gradient and central peak in the dispersion map. Calculating its $\Delta V/2\sigma$ results in a value of 1.34. The rotation curve seems to be levelling off to a constant velocity, so we are most likely imaging the galaxy all the way out to the dark matter halo.

Source J

The rotation axis of the galaxy is well defined by the symmetry in Source J. However looking at the dispersion map it's clear that the galaxy is somewhat turbulent and clearly does not have a peak dispersion. Calculating its $\Delta V/2\sigma$ results in a value of

0.77. The rotation curve does seem to level off as well, meaning we are most likely seeing the whole velocity spread of the galaxy. Generally, the rotation axis seems to align with the maximum velocity gradient.

Source K

The symmetric nature of the galaxy seems to indicate that the rotation axis is completely N-S even though there are a few high velocity pixels to the NW. The rotation axis does align with the maximum velocity gradient, although some edge pixels were left out of the calculations again due to arbitrarily raising the peak to peak velocity. Although the velocity field is fairly ordered, the dispersion map shows that there is a very broad peak offset from the flux center implying that the kinematics are leaning more towards being dispersion dominated. Calculating its $\Delta V/2\sigma$ results in a value of 0.65. The rotation curve does not seem to show any signs of flattening, thus we may need better data in order to map the velocity field completely.

Source L

There is no sign of a rotating disk in Source L. Thus, the galaxy is most likely a dispersion dominated galaxy. Calculating its $\Delta V/2\sigma$ results in a value of 0.43. The rotation axis shown below is arbitrary since it shows no sign of rotation.

6.3 $\Delta V/2\sigma$

From our sample and from Förester Schreiber et al. (2009), it seems clear that anything with $\Delta V/2\sigma < 0.4$ is a dispersion dominated galaxy. This value was chosen based on Source L, which seems to have almost no evidence of rotation in its velocity map and seems to be the most dispersion dominated source in the sample. Given that Source L has a $\Delta V/2\sigma = 0.43$, a value of $\Delta V/2\sigma < 0.4$ was chosen as the completely dispersion dominated criteria. In contrast to this, the most rotationally dominated Source in the sample seems to be Source A, based on its velocity and dispersion maps. Thus, given that Source A has a $\Delta V/2\sigma = 0.96$, a value of $\Delta V/2\sigma > 1.0$ was chosen as the completely rotationally dominated criteria. However, it becomes more vague in between $0.4 < \Delta V/2\sigma < 1.0$ where some of the sources seem to have qualities of both types of galaxies. Source J for example ($\Delta V/2\sigma = 0.77$) has a fairly smooth velocity gradient, but its dispersion map shows a wide spread over the entire galaxy. Thus, it seems that for galaxies with $0.4 < \Delta V/2\sigma < 1.0$, both rotation and dispersion are relevant to their kinematics.

Chapter 7

Discussion

7.1 Interpreting the $\mathrm{M}_{\mathrm{dyn}}$ of Protcluster Galaxies

As stated previously, when calculating the dynamical masses of SMGs, it can be difficult to know which one of the two dynamical mass equations gives a better estimate. When measuring the dynamical mass from the rotation of a galaxy, there are a number of different issues that could arise. If a galaxy is undergoing a major merger, the rotation of the galaxy can be interrupted and thus, no real rotation can be obtained in order to estimate the mass. This issue can be compounded by the fact that some galaxies are too small to be resolved by the large beam size of the telescopes used. It is also possible that some of these galaxies simply aren't disk galaxies, and the rotation mass equation would not give a good estimate (ie. Source L). The same applies to the dispersion-dominated mass estimate as well. Some galaxies are more rotationally dominated (ie. Source A) and thus the dispersion equation would not give a good estimate of the dynamical mass.

In any case, it is important to be able to distinguish between the two extremes in order to get a good estimate of the dynamical mass. It is also clear that from the analysis on each individual galaxy (§6.2) that a simple rotation or simple dispersion estimate is typically not a good characterization, and a new method in order to interpret the $\mathrm{M_{dyn}}$ estimates is desirable to best make use of the information in a galaxy's properties. A detailed disk modelling of a large selection of galaxies would go a long way in determining how to best quantify the $\mathrm{M_{dyn}}$. A weighted average of both mass estimates was derived as a first step towards a more detailed study. The weighted average estimate is dependent upon the criteria derived in §6.3, which gave a fairly good indication whether or not a galaxy was rotationally or dispersion dominated. The motivation for such an equation is to try and have the mass estimates closer to reality. Source K for example has a very clear rotation axis, but there is also a significant measure of dispersion that is sufficient to support some of the gravitational collapse.

Thus, we estimate that the "Optimal" Dynamical Mass for a galaxy be

$$\mathrm{M_{dyn}} = \begin{cases} 1.56 \times 10^6 \sigma^2 R & \text{if } \Delta V/2\sigma < 0.4 \\ 1.56 \times 10^6 \sigma^2 R(-\frac{5}{3}\Delta V/2\sigma + \frac{5}{3}) + 2.35 \times 10^5 V^2 R(\frac{5}{3}\Delta V/2\sigma - \frac{2}{3}) & \text{if } 0.4 < \Delta V/2\sigma < 1.0 \\ 2.35 \times 10^5 V^2 R & \text{if } \Delta V/2\sigma > 1.0 \end{cases} \tag{25}$$

As explained above, the two bounding estimates are for when a galaxy is completely rotationally or dispersion dominated, whereas the middle equation is used for galaxies that have both characteristics. The equation was derived by assuming that the transition between both estimates would be linear. The constants used in both linear terms are there to ensure that the function is continuous between both boundaries.

Further insight into the $\mathrm{M_{dyn}}$ estimates can be gained by plotting each against the galaxies SFR (where we have used the velocity or dispersion fields as symbols as a reference point for the individual galaxies properties). Figure 21 and Figure 22 show the rotational and dispersion mass estimators versus SFR, respectively and Figure 23 shows the Optimal Mass Estimator versus SFR as well. In general, one would expect that for a higher mass, the SFR would also increase. This is because more mass is required in order to counteract the additional radiation pressure due to the newly forming stars [30]. Thus, by observing this relation in any of the plots, it may suggests that one mass estimate may be better than the others.

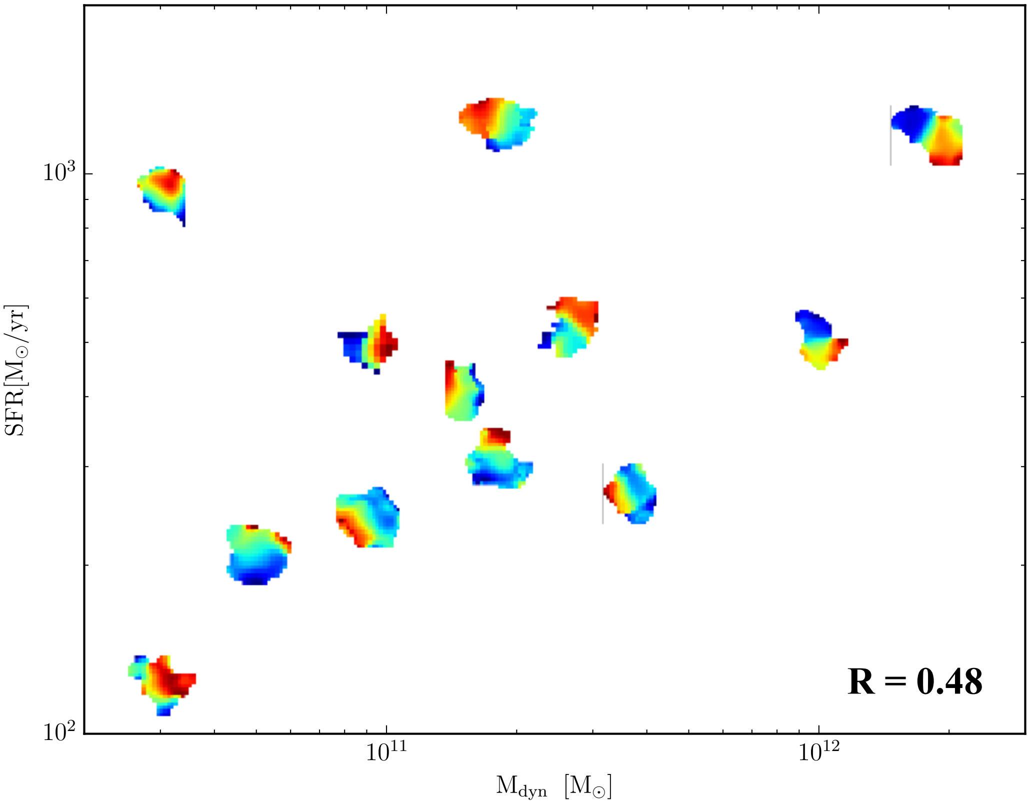

Figure 21: The above figure shows the dynamical mass estimated from the rotation velocity of the galaxy vs SFR. The plot symbol for each point is represented as the velocity map of each source. There seems to be a vague positive trend in the plot implying that a higher SFR rate would need a higher dynamical mass in order to support it, as expected. The correlation coefficient between the two parameters is R = 0.48.

In all 3 Figures, it seems there is some evidence that implies a higher SFR requires a higher M_{dyn} to support it, which isn't unexpected, although outlying galaxies with

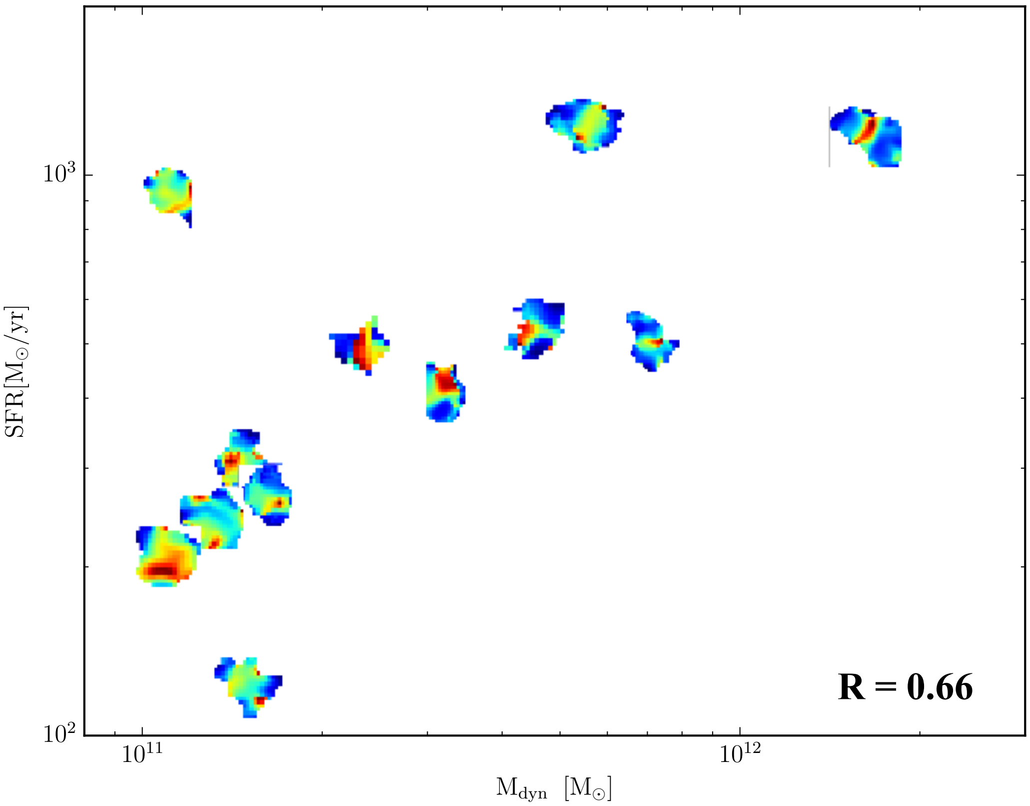

Figure 22: The above figure shows the dynamical mass estimated from the dispersion of the galaxy vs SFR. The plot symbol for each point is represented as the dispersion map of each source. There seems to be a fairly strong positive trend in the plot suggesting that a higher SFR requires a larger dynamical mass in order to support it, as expected. The correlation coefficient between the two parameters is R = 0.66.

very high (but likely short lived) SFRs for their M_{dyn} punctuate any underlying trend. The correlation coefficient, R, was determined for each of the plots to determine which one most strongly correlates total mass and SFR. The trend seems to be the strongest in Figure 22, the dispersion mass estimate, which gives a correlation coefficient R = 0.66, in contrast to the rotation estimate which gives R = 0.48, and the optimal mass estimate which gives R = 0.58. Thus, this may imply that the dispersion mass estimate is the best way to characterize the dynamical mass for these galaxies in the early, very dense protocluster system. This does make sense since given the

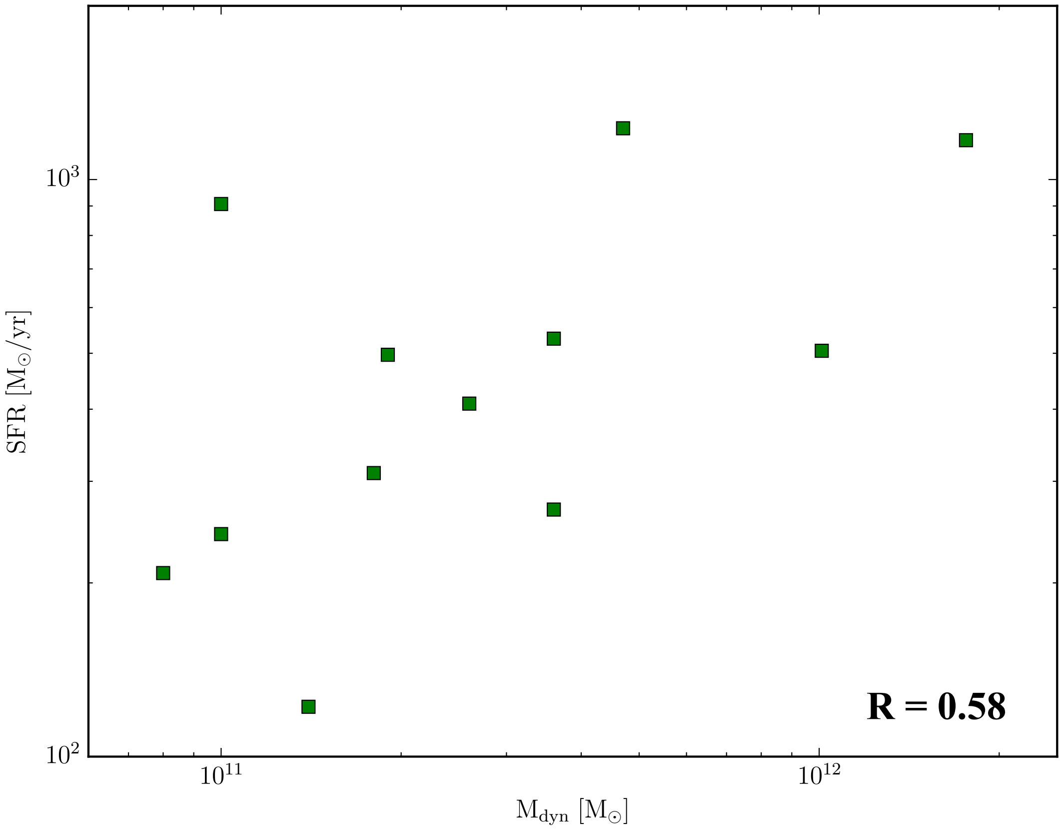

Figure 23: The above figure shows the optimal mass estimate vs SFR for each of the galaxies in SPT2349-56. Again, there seems to be a vague positive trend in the plot suggesting that a higher SFR requires a larger dynamical mass in order to support it, as expected. The correlation coefficient between the two parameters is R = 0.58.

dense environment of the protocluster, where mergers are more likely to occur and the gravitational force on all of these galaxies are very high which would most likely make these galaxies environment very chaotic. Förester Schreiber et al. (2009) find that generally for lower redshift and lower SFR galaxies, that the rotation mass estimate and the dispersion mass estimate both correlate well with SFR, indicating that the high density environment in the protocluster may be increasing the gas dispersion support in these SMGs. Given the relationship between SFR and M_{dyn} for the optical mass estimate (Figure 23) it is clear the weighted average approach used here did not work very well and would need refinements and better modelling to implement.

Now, by comparing the galaxies in SPT2349-56 to the sample of galaxies in Förester Schreiber et al. (2009) (typical galaxies found at at z $\sim$ 2.5, which aren't located in the dense environment of a protocluster core), one can gain insight into the difference between our protocluster galaxies versus normal field galaxies. Figure 24 shows the dynamical masses of all the galaxies in both samples plotted against their SFR. The mass estimate used in the plot for the SPT2349-56 sample is the Optimal Mass Estimate, as the galaxies in Förester Schreiber et al. (2009) use a mix of both rotational and dispersion-dominated estimates. Most of the galaxies in SPT2349-56 seem to have much larger dynamical masses and SFR than typical field galaxies, which we attribute to the dense environment of the protocluster.

Again, comparing the sample of galaxies in Förester Schreiber et al. (2009) to the ones in SPT2349-56, Figure 25 shows the value of $\Delta V/2\sigma$ plotted against the dynamical masses of the galaxies. Again in this case, the optimal mass estimate was used. The value of $\Delta V/2\sigma$ seems to generally increase with increasing dynamical mass. This may imply that if a galaxy becomes sufficiently large, then the rotational kinematics may swamp the turbulent component. Thus, for extremely massive galaxies, the rotational mass estimate may be better choice.

Its clear that there are many factors that play into whether one mass estimate should be used over another, and no clear consensus on which estimate should be used in any case. Thus, finding more samples of galaxies with known $\Delta V/2\sigma$ values to compare these results to is required.

7.2 Galaxy Mass Fractions

Once the masses of all the sources in SPT2349-56 was determined, the next question then became, what makes up this mass? Local disk galaxies, such as the milky way,

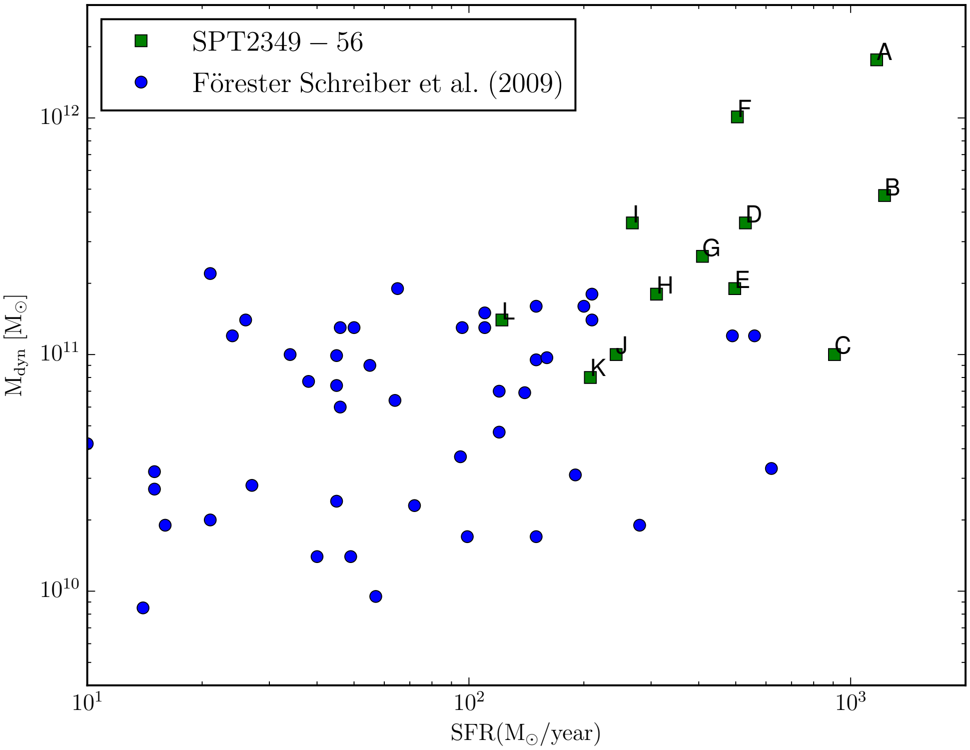

Figure 24: The optimal dynamical mass plotted against SFR for both our sample (SPT2349-56) as well as the field galaxies in the Förester Schreiber et al. (2009) sample. All of the galaxies in SPT2349-56 have much larger masses and SFRs. This is most likely do to the dense environment they reside in.

are highly dark matter dominated, wheres local elliptical galaxies are more baryon dominated typically. Given the stellar mass and gas masses from Miller et al. 2015 and the calculated dynamical masses from this analysis, the baryonic mass fractions for each galaxy in SPT2349-56 can be determined. Figure 26 shows the baryonic mass fraction ($[M_* + M_{gas}]/M_{dyn}$) of the 12 sources in SPT2349-56 as a function of the optimal M_{dyn}. The graph shows that at higher M_{dyn}, there is a lower fraction of baryonic mass, meaning there is a larger fraction of dark matter present. As expected, this implies that galaxies can only get so large with baryonic matter alone, but in order for galaxies to reach extremely high masses, they must have a large dark matter halo (White and Rees, 1978). It's possible galaxies cannot reach extremely

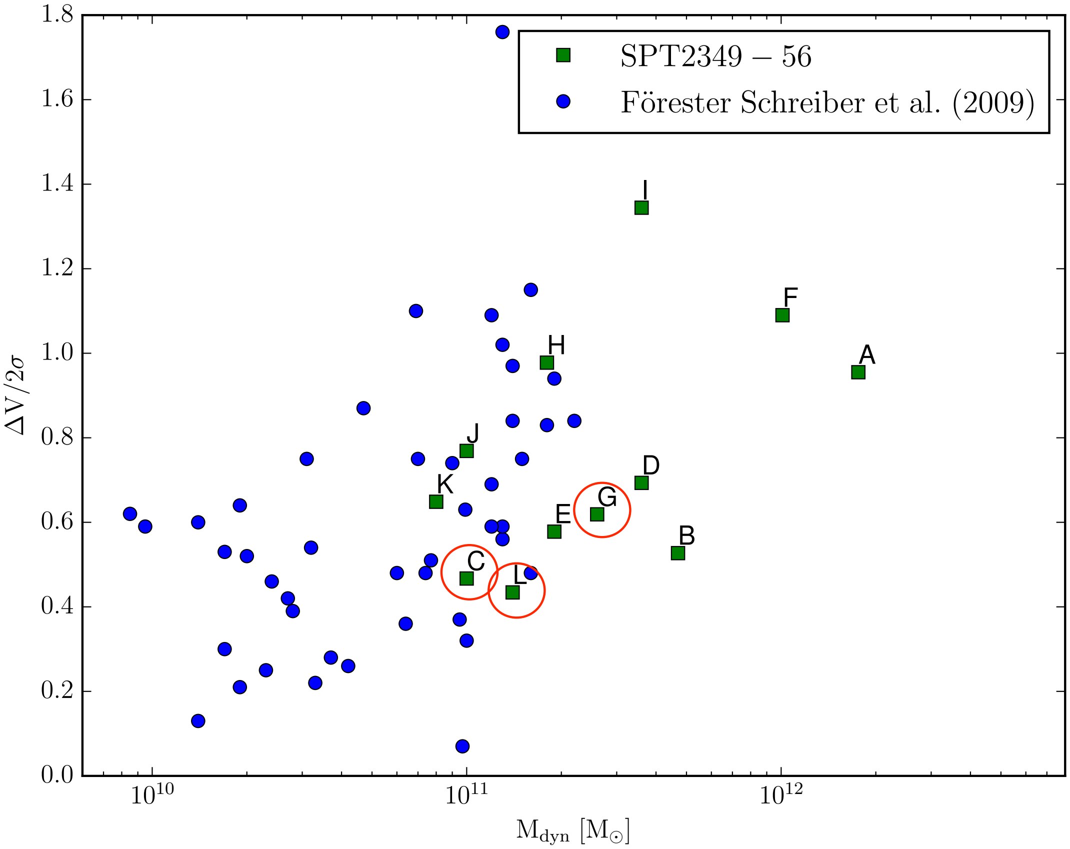

Figure 25: $\Delta V/2\sigma$ plotted against the optimal dynamical mass for both our sample (SPT2349-56) as well as the field galaxies in the Förester Schreiber et al. (2009) sample. It seems that for a higher mass galaxy the $\Delta V/2\sigma$ value is also increasing, suggesting that more massive galaxies are more rotationally dominated systems. The sources that do not have a well defined rotation axis but were forced one regardless to obtain a ΔV value are flagged with a red circle around them.

high masses with baryonic matter alone due to feedback mechanisms which drive the baryonic matter out of the galaxy (supernova, high velocity winds, etc).

As mentioned earlier, the galaxies residing in SPT2349-56 reside in a dense protocluster environment, which is most likely affecting their evolutionary process. Comparing these galaxies to other SMGs that are not a in a cluster or protocluster may help to characterize exactly how they have or haven't evolved differently. Bothwell et al, (2012) were able to successfully measure the gas fraction within their sample

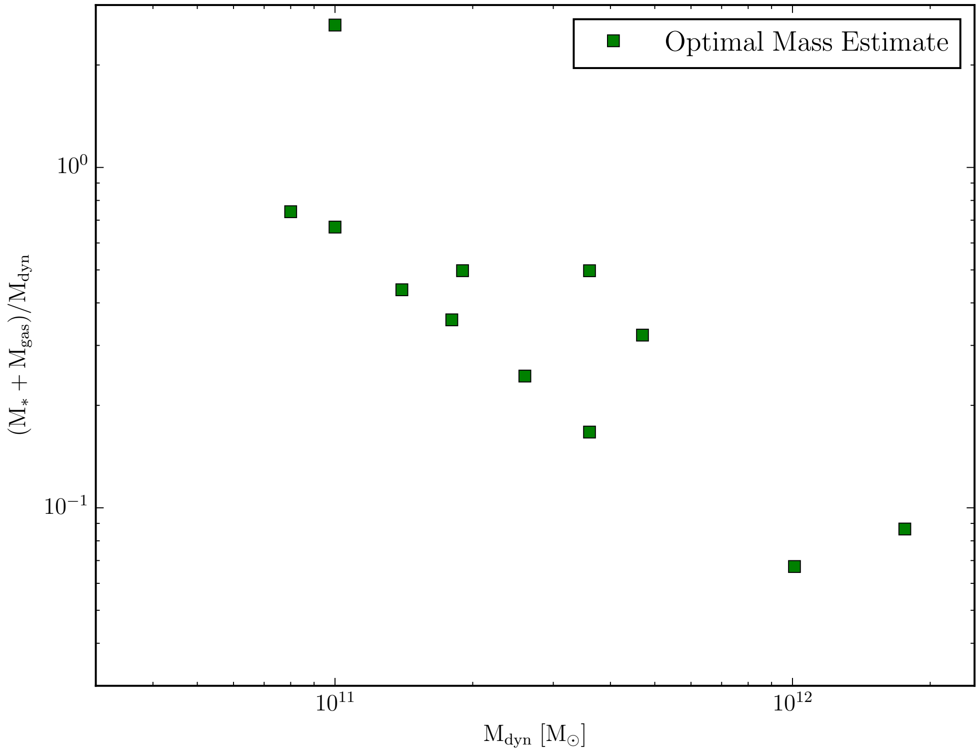

Figure 26: The baryonic mass fraction versus the optimal dynamical mass of each galaxy. Each point is labeled by its Source name its associated with. The general trend of the plot shows that the lower the dynamical mass of the galaxy, the higher fraction of baryonic mass it contains.

of field SMGs, so SPT2349-56 will be compared to their results. Figure 27 shows the fraction of gas in both our sample and Bothwell et al (2012)'s galaxies versus the total dynamical mass estimated from the dispersion (since Bothwell et al, (2012) exclusively used the dispersion estimate to measure their galaxies masses). The graph shows that the protocluster galaxies generally have a higher dynamical mass, but a lower fraction of gas. This is probably due to the fact that in such dense environments stars are formed at a much faster rate and their gas reserves are depleted much more quickly.

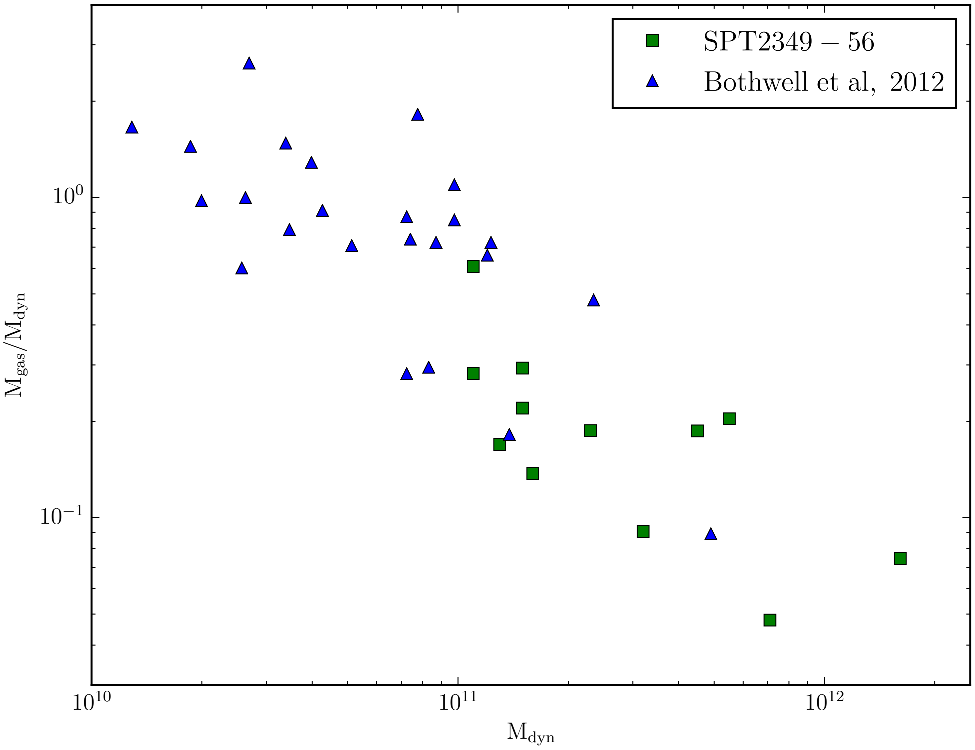

Figure 27: The gas fraction in each galaxy versus the dynamical mass estimated from the dispersion. The galaxies in SPT2349-56 (a dense protocluster) are compared to typical field galaxies from Bothwell et al, (2012). The plot shows that for a higher mass galaxy, the gas fraction is lower. This is attributed to the fact that a higher mass implies there is more gravitational force acting on the galaxy, causing more pressure and more stars to form. With more stars forming, the gas reservoirs will be depleted, giving a lower gas fraction.

7.3 Cluster Mass Fractions

Another important characteristic of this system is the total dynamical mass of the protocluster. This was previously calculated in Miller et al. (2018) as 1.16 $\times 10^{13}$ $M_{\odot}$. Again however, its important to understand exactly what makes up this cluster mass. Again, given the stellar and gas mass from Miller at al. (2018), dark matter mass of every source in SPT2349-56 can be determined now that the total mass of each galaxy is known. The dark matter mass is simply the total mass of the galaxy with the stellar and gas masses subtracted off. Finally, given all the mass contributions, the fraction each contributes to the total mass of the protocluster can be determined. Figure 28 shows a pie chart of the mass fractions in the galaxy protoccluster. 6.5% of the total mass is given by stars, 5.7% of the total mass is given by the gas, and 41.7% of the mass is given by dark matter. Surprisingly, 46% of the mass in SPT2349-56 is left over and not accounted for in our analysis. . However, the error on the total mass of the protocluster is large and it is possible for the 46% to go down to 0% if the lower limit of the total mass is used (5.0 $\times 10^{12}$ $M_\odot$). However, if that isn't the case, it is still important to try and determine that the unaccounted mass could be. Although its difficult to determine exactly what form this "other" category takes, by comparing with simulations one can get a little better idea of what it's made up of.

Liang et al. (2016) simulated groups of galaxy clusters in order to understand cluster mass fractions at different epochs (Figure 29) [27]. Comparing our mass fractions results on their plot shows the baryonic mass fractions sit reasonably well where you might expect them for a redshift of z $\sim$ 4.3 (top, third and fourth panels). One thing we are not able to measure however is the Hot Intragroup Medium (IGrM), which if we extrapolate for a redshift of 4.3 gives a value of $\sim$ 3%. Thus, it seems as if at least 3% of the other category is due to hot gas that exists between the galaxies in the cluster. This implies that $\sim$ 43% of the protocluster mass is still unaccounted for. The only other possibility then, is that this unaccounted for mass is dark matter that is not measured and other smaller or fainter galaxies within the cluster we cannot see. This is a very surprising result, and would be interesting to be able to compare to future cluster measurements to see if they find similar measurements.

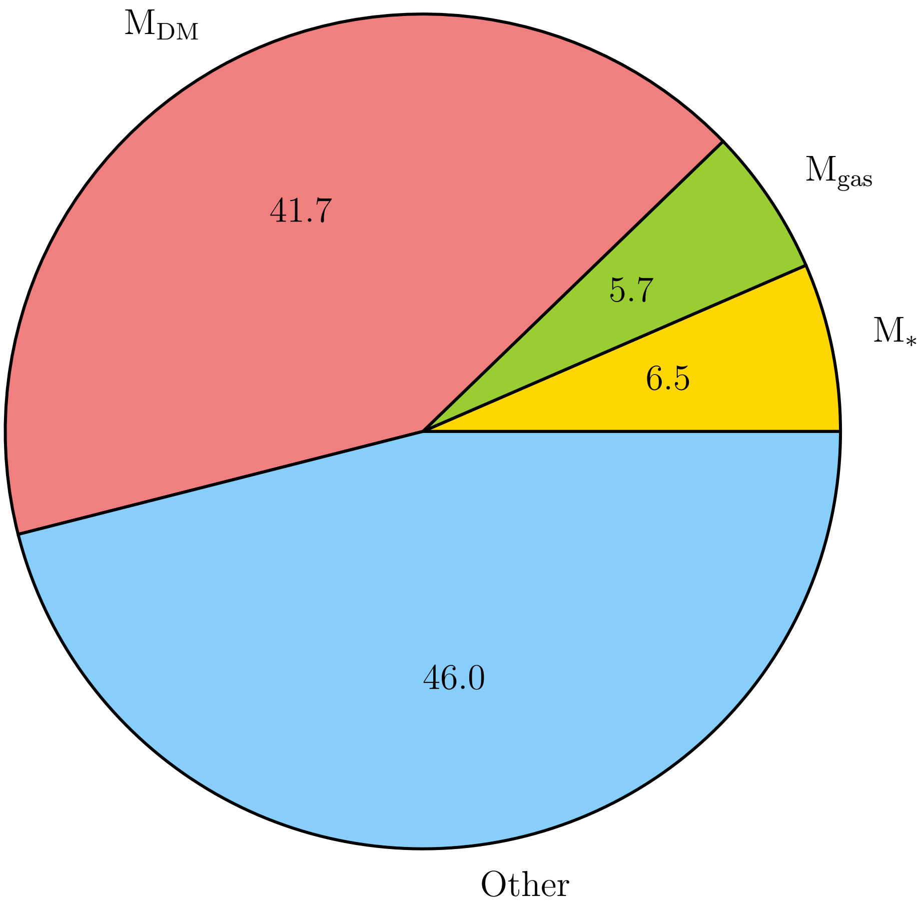

Figure 28: A pie chart displaying the mass fractions within the cluster SPT2349-56. 6.5% of the total mass is given by stars, 5.7% of the total mass is given by the gas, and 41.7% of the mass is given by dark matter. Surprisingly, 46% of the mass contained within the cluster is not seen in our analysis.

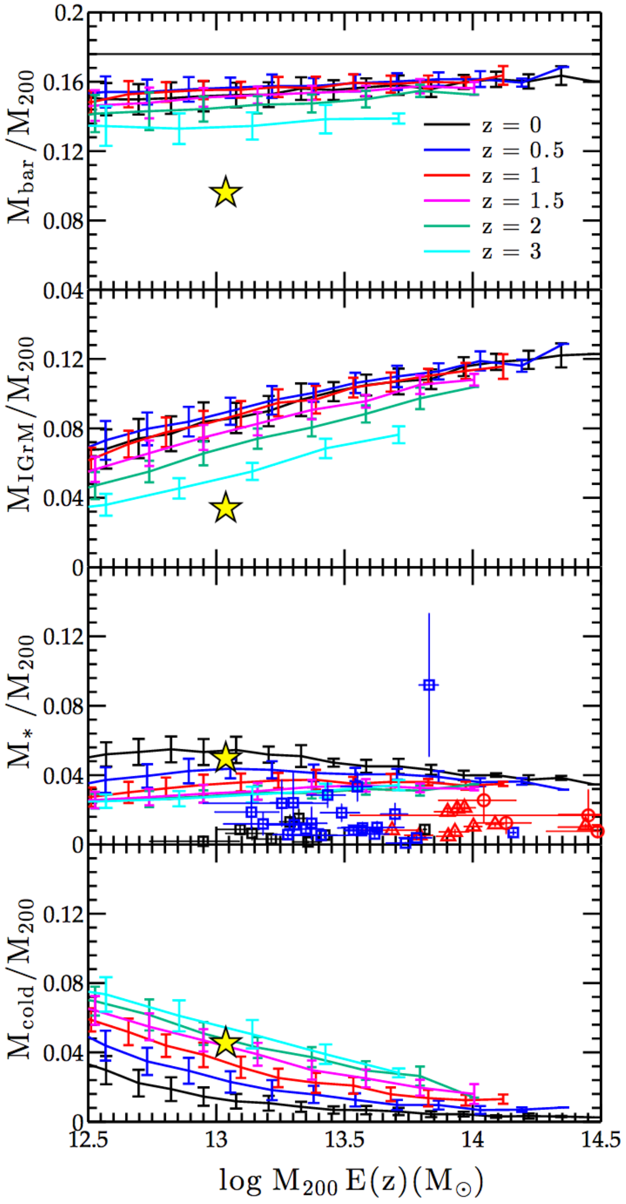

Figure 29: The above figure was taken from Liang et al. (2016) which shows the mass fractions for simulated galaxy clusters at different redshifts. In each panel SPT2349-56 is marked as a yellow star. **Top Panel:** The total baryonic mass fraction of the cluster. SPT2349-56 sits reasonably well where one might expect for a cluster at z = 4.3. **Second Panel:** The hot intragroup medium (IGrM) fraction. This property was not measured from the analysis of SPT2349-56. Thus, the value is extrapolated to where the cluster might lie for a redshift of 4.3, which gives a value of ∼ 3%. **Third Panel:** The stellar mass fraction. SPT2349-56 seems to sit a bit higher than where one might expect given the simulations, however it's not too far off. **Fourth Panel:** The Gas Mass fraction. SPT2349-56 is very close to where it is expect the gas mass should be, if again the values is extrapolated out to redshift 4.3

Chapter 8

Conclusions

Here we have presented the an analysis of the protocluster SPT2349-56, and the 12 brightest SMGs residing within it. All 12 galaxies were mapped out and their kinematics were determined by fitting Gaussian profiles to their emission lines. From these kinematics, their dynamical masses were also determined. We summarize our conclusions in the following.

Each galaxy was looked at case by case in order to determine whether or not it was rotationally or dispersion dominated kinematics. This was done by considering both the quantitative value of $\Delta V/2\sigma$ as well as a qualitative analysis of their velocity and dispersion fields.

We then found that although some galaxies are completely dispersion or rotationally dominated, it seems a lot of the sources we observed have qualities of both. Thus, we proposed an Optimal dynamical mass formula, which depends on the quantity $\Delta V/2\sigma$. This will hopefully be a first step towards determining a more accurate description of the dynamical mass for any type of galaxy observed. However, we do hypothesize that given the dense state of our protocluster galaxies, the dispersion estimate may generally give more accurate results over the rotation estimate. Also, comparing our results to the SINS sample of galaxies shows that our sample of SMGs generally have much larger SFRs and dynamical masses than typical field galaxies do, which is also attributed to the dense environment of SPT2349-56. Looking a little more closely at at the parameter $\Delta V/2\sigma$ revealed that the value seems be getting larger for increasing dynamical mass, meaning that massive galaxies may have their kinematics swamped by rotation.

Then, looking at the baryonic mass fraction within each of the individual galaxies showed a general trend towards a higher mass fraction for SMGs with lower dynamical masses. This suggests, as expected by White and Rees, (1978), that galaxies can only become extremely massive if they have a large dark matter halo, whereas feedback mechanisms will inhibit the baryonic mass from getting too large. Also, comparing our sample's gas mass fraction with field SMGs from Bothwell et al (2012) shows that our sources generally have higher dynamical masses, but lower gas fractions. This is most likely the case because the dense environment of SPT2349-56 caused the gas to be used up quickly and be depleted.

Finally, looking at the total mass fractions of the cluster SPT2349-56 revealed that over 46% of the total mass of the cluster was unaccounted for in this analysis. Meaning we see a little more than half of the mass contained within this cluster. This can be explained by using the lower limit of the mass estimate, however it is possible there is other matter in the protocluster that are not visible in the images. Comparing and extrapolating from simulations done in Liang et al. (2016) suggests that about 3% of the unaccounted for mass could be Hot Intragalactic Medium. The remaining 43% could then be fainter galaxies, or dark matter that we are not able to observe.

In the future, we hope to achieve higher resolution observations of these galaxies in order to further quantify these results and possibly see more of the faint galaxies we expect to see from our analysis. As stated before, simulations are yet to replicate the state that SPT2349-56 is undergoing at this epoch. Thus, by attaining better resolution images of these objects, we could more accurately determine the parameters of all these galaxies, with the hopes of constraining the simulations further.

We also hope to find more protoclusters similar to SPT2349-56 in the future in order to compare and assess the significance of our results. Finding more of these systems would also help us determine whether or not the state that SPT2349-56 is in, is a common occurrence or if we are observing this protocluster at an extremely rare event where all of the SMGs within the protocluster are undergoing starbursts. Either way, SPT2349-56 is an extremely useful tool in order to further understand the evolution of the universe. Of course, finding more of these systems is a non-trivial task, and will require us to continue to work hard in the field of submillimeter astronomy.

Table 1: The measured properties of each of the galaxies in SPT2349-56.

Source	RA (J2000) [h:m:s]	Dec (J2000) [d:m:s]	$S_{1000\mu m}$ [mJy]	$S_{870\mu m}$ [mJy]	[CII] $\int$ S dv [a] [Jy Km s^{-1}]	Central σ [km s^{-1}]	[CII] σ_V [b] [km s^{-1}]
A	23:49:42.67	-56:38:19.3	4.63 ± 0.04	7.8 ± 0.1	8.176	372.8 ± 5	535 ± 10
B	23:49:42.79	-56:38:24.0	4.35 ± 0.04	8.2 ± 0.1	7.724	327.2 ± 5	393 ± 4
C	23:49:42.84	-56:38:25.1	2.69 ± 0.04	6.0 ± 0.1	4.224	198.6 ± 1	193 ± 2
D	23:49:41.42	-56:38:22.6	2.20 ± 0.08	3.5 ± 0.3	1.759	469.8 ± 20	346 ± 10
E	23:49:41.23	-56:38:24.4	2.12 ± 0.11	3.3 ± 0.4	0.931	351.9 ± 12	393 ± 14
F	23:49:42.14	-56:38:25.8	1.69 ± 0.05	3.4 ± 0.1	2.859	331.7 ± 3	397 ± 4
G	23:49:42.74	-56:38:25.1	1.11 ± 0.04	2.7 ± 0.1	2.349	305.9 ± 5	277 ± 4
H	23:49:43.46	-56:38:26.2	0.85 ± 0.05	2.1 ± 0.1	2.216	250.0 ± 1	237 ± 2
I	23:49:42.22	-56:38:28.3	0.78 ± 0.05	1.8 ± 0.1	1.788	243.4 ± 2	217 ± 2
J	23:49:43.22	-56:38:30.1	0.61 ± 0.06	1.6 ± 0.2	2.133	176.0 ± 2	175 ± 2
K	23:49:42.96	-56:38:17.9	0.34 ± 0.04	1.4 ± 0.1	2.190	164.2 ± 2	166 ± 1
L	23:49:42.38	-56:38:25.8	0.23 ± 0.04	0.8 ± 0.1	2.493	207.6 ± 2	201 ± 1
M	23:49:43.39	-56:38:21.1	0.21 ± 0.05	0.5 ± 0.2	–	–	–
N	23:49:43.27	-56:38:22.9	0.18 ± 0.04	0.4 ± 0.1	–	–	–

[a] The value of the central integrated velocity flux value

[b] The value of the total/summed dispersion

Table 2: The derived properties for each of the galaxies in SPT2349-56.

Source	ΔV [km s^{-1}]	SFR [$M_\odot$ yr^{-1}]	M_{dyn} (σ) [10^{11} $M_\odot$]	M_{dyn} (V) [10^{11} $M_\odot$]	Size [kpc]	Corr. Size [kpc]	$\Delta V/2\sigma$	M_{dyn} (optimal) [10^{11} $M_\odot$]
A	1021.579533	1170± 390	16.1	17.7	8.0	7.2	0.96	17.6
B	414.238042	1227± 409	5.5	1.8	5.7	4.6	0.53	4.7
C	180.645162	907 ± 302	1.1	0.3	5.0	3.7	0.47	1.0
D	479.228426	530 ± 182	4.5	2.6	6.0	4.9	0.69	3.6
E	454.727475	497 ±179	2.3	0.9	3.9	1.9	0.58	1.9
F	865.850946	505 ±169	7.1	10.1	6.7	5.8	1.09	10.1
G	342.602892	409 ±137	3.2	1.5	6.4	5.4	0.62	2.6
H	464.071190	310 ±105	1.5	1.8	4.9	3.5	0.98	1.8
I	584.200501	268 ±91	1.6	3.6	5.6	4.5	1.34	3.6
J	269.492928	243 ±85	1.3	0.9	6.3	5.3	0.77	1.0
K	214.905451	208 ±71	1.1	0.5	6.0	4.9	0.65	0.8
L	174.416018	122 ±43	1.5	0.3	5.9	4.8	0.43	1.4
M	–	75 ± 34	–	–	–	–	–	–
N	–	64 ± 29	–	–	–	–	–	–

Bibliography

[1] C.M. Casey D. Narayanan and A. Cooray. Dusty star-forming galaxies at high redshift. *Physics Reports*, 541:45–161, 2014.

[2] Juan E. González et al. The role of submillimetre galaxies in hierarchical galaxy formation. *Monthy Notices of the Royal Astronomical Society*, 413(2):749–762, April 2011.

[3] S. C. Chapman et al. A redshift survey of the submillimeter galaxy population. *The Astrophysical Journal*, 622(2):772–796, April 2005.

[4] C. L. Carilli et al. Imaging the molecular gas in a submillimeter galaxy at z = 4.05: Cold mode accretion or a major merger? *The Astrophysical Journal*, 714(2):1407–1417, May 2010.

[5] J. M. Simpson et al. The scuba-2 cosmological legacy survey: Alma resolves the bright end of the sub-millimeter number counts. *The Astrophysical Journal*, 807(2), July 2015.

[6] H. Engel et al. Most submillimeter galaxies are major mergers. *The Astrophysical Journal*, 724(1):233–243, November 2010.

[7] R. Gray and J. Dunning-Davies. A review of redshift and its interpretation in cosmology and astrophysics.

[8] Gabriel R. Bengochea. What do we talk about when we speak of cosmological redshift? February 2018.

[9] John G. Hartnett Moshe Carmeli and Firmin J. Oliveira. The cosmic time in terms of the redshift. *Foundations of Physics Letters*, 19(3):277–283, June 2006.

[10] V. K. Shchigolev. Calculating luminosity distance versus redshift in flrw cosmology via homotopy perturbation method. *Gravitation and Cosmology*, 23(2):142–148, April 2017.

[11] Mauro Giavalisco. *Galaxy Evolution*. Nature Publishing Group, 2001.

[12] Roberto G. Abraham and Sidney van den Bergh. The morphological evolution of galaxies. *Science*, 293(5533):1273–1278, August 2001.

[13] J. I. Davies et al. Dustpedia: A definitive study of cosmic dust in the local universe. *The Astronomical Society of the Pacific*, 129(974), March 2017.

[14] Rachel S. Somerville and Romeel Dave. Physical models of galaxy formation in a cosmological framework. *Annual Review of Astronomy and Astrophysics*, 53:51–113, April 2015.

[15] L. Silva et al. Modelling the spectral energy distribution of galaxies: introducing the artificial neural network. *Monthly Notices of the Royal Astronomical Society*, 410(3):2043–2056, January 2011.

[16] E. Da Cunha et al. An alma survey of sub-millimeter galaxies in the extended chandra deep field south: Physical properties derived from ultraviolet-to-radio modelling. *The American Astronomical Society*, 806(1), June 2015.

[17] R. Narayan and M. Bartelmann. Lectures on gravitational lectures on gravitational lensing. ArXiv Astrophysics e-prints, October 1997.

[18] Michele Cappellari. Structure and kinematics of early-type galaxies from integral field spectroscopy. *Annual Review of Astronomy and Astrophysics*, 54:597–665, 2016.

[19] Van Albada et al. Distribution of dark matter in the spiral galaxy ngc 3198. *Astrophysical Journal*, 295:305–313, August 1985.

[20] J. Wagg. [cii] line emission in massive star-forming galaxies at z = 4.7. *The Astrophysical Journal Letters*, 752(2), 2012.

[21] M. Cousin G. Lagache and M. Chatzikos. The [cii] 158 m line emission in high-redshift galaxies. *Astronomy and Astrophysics*, 609(A130), January 2018.

[22] G. C. Jones et al. Dynamical characterization of galaxies at z 4-6 via tilted ring fitting to alma [cii] observations. *The Astrophysical Journal*, 850(2), 2017.

[23] Paolo Cabella Vladimir Luković and Nicola Vittorio. No access dark matter in cosmology. *International Journal of Modern Physics A*, 29(19), 2014.

[24] A. Gnerucci et al. A dynamical mass estimator for high z galaxies based on spectroastrometry. *Astronomy and Astrophysics*, 533(A124), September 2011.

[25] M. S. Bothwell et al. A survery of molecular gas in luminous sub-millimetre galaxies. *Monthy Notices of the Royal Astronomical Society*, 429(4):3047–3067, March 2013.

[26] *ALMA Partnership, 2017, S. Asayama, A. Biggs, I. de Gregorio, B. Dent, J. Di Francesco, E. Fomalont, A. Hales, J. Hibbard, G. Marconi, S. Kameno, B. Vila Vilaro, E. Villard, F. Stoehr.*

[27] Liang et al. The growth and enrichment of intragroup gas. *Monthly Notices of the Royal Astronomical Society*, 456(4):4266–4290, March 2016.

[28] T. B. Miller et al. A massive core for a cluster of galaxies at a redshift of 4.3. *Nature*, 556:469–472, 2018.

[29] C. M. Casey et al. A massive, distant proto-cluster at z=2.47 caught in a phase of rapid formation. *The Astrophysical Journal Letters*, 808(2), 2015.

[30] Nick Scoville. Starburst and agn connections and models. *Journal of The Korean Astronomical Society*, 36(3):167–175, 2003.

Appendix A

The following Appendix contains the integrated velocity flux maps, velocity maps, and dispersion maps for all the galaxies characterized in this thesis.

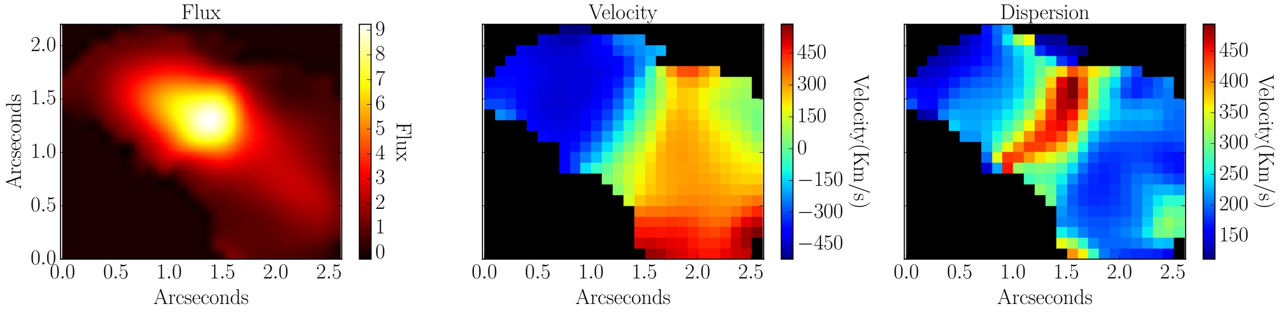

Figure 30: The integrated velocity flux map, velocity field map, and the dispersion map for Source A in SPT2349-56.

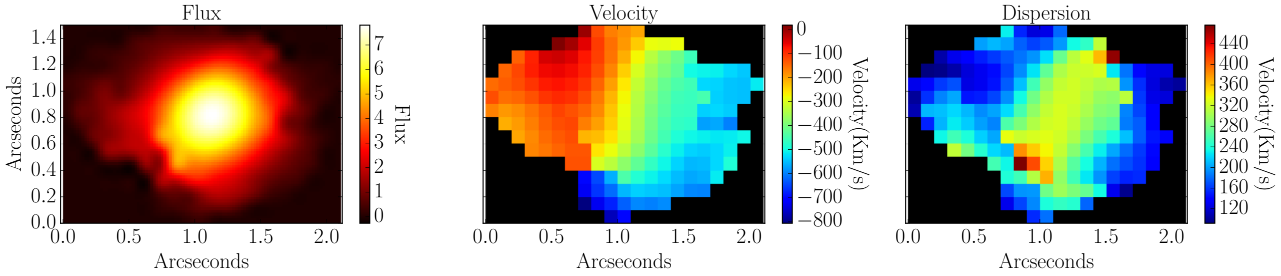

Figure 31: The integrated velocity flux map, velocity field map, and the dispersion map for Source B in SPT2349-56.

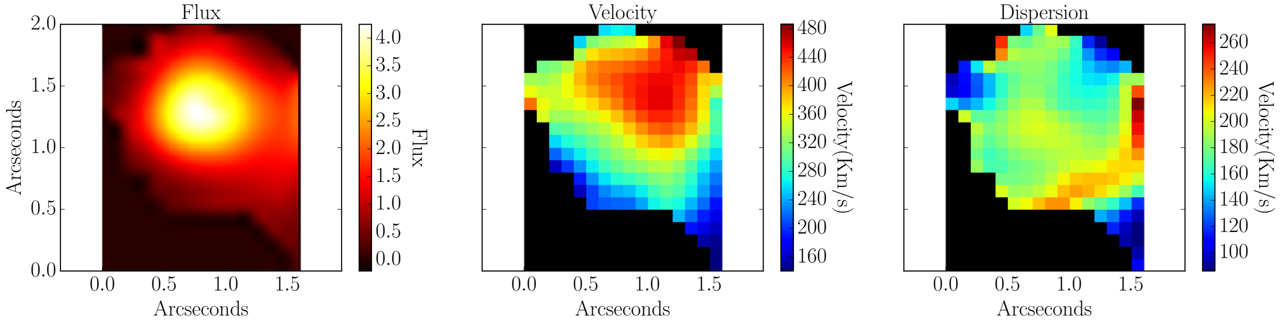

Figure 32: The integrated velocity flux map, velocity field map, and the dispersion map for Source C in SPT2349-56.

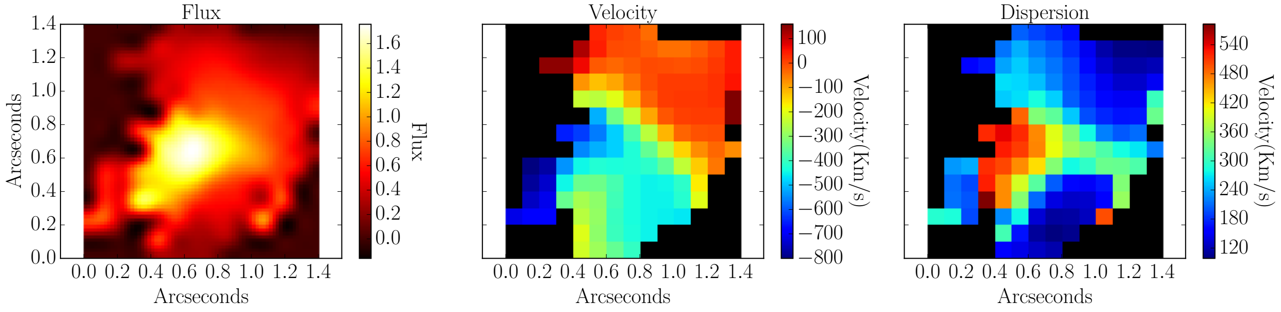

Figure 33: The integrated velocity flux map, velocity field map, and the dispersion map for Source D in SPT2349-56.

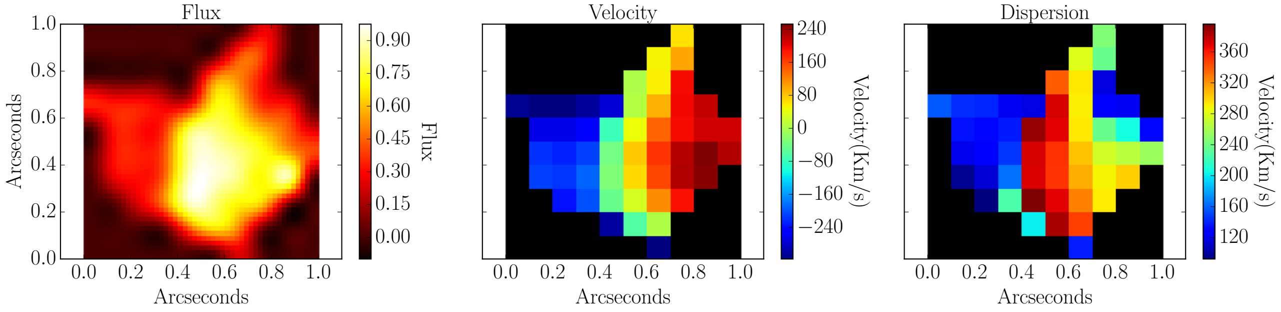

Figure 34: The integrated velocity flux map, velocity field map, and the dispersion map for Source E in SPT2349-56.

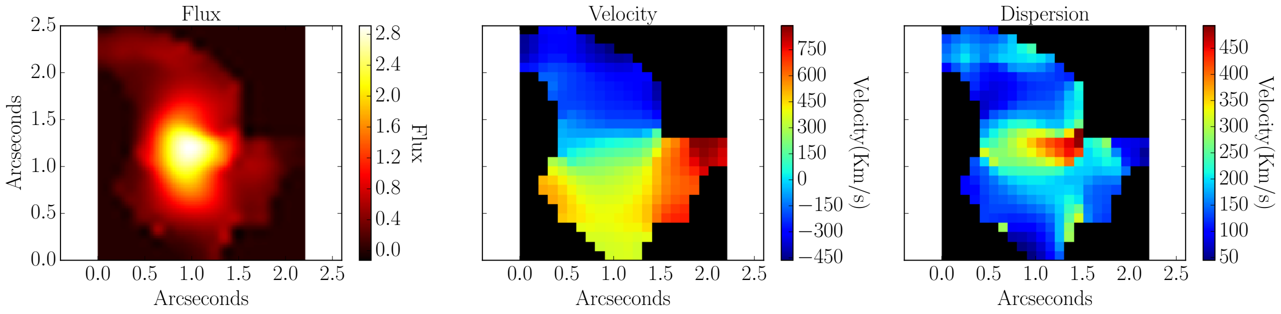

Figure 35: The integrated velocity flux map, velocity field map, and the dispersion map for Source F in SPT2349-56.

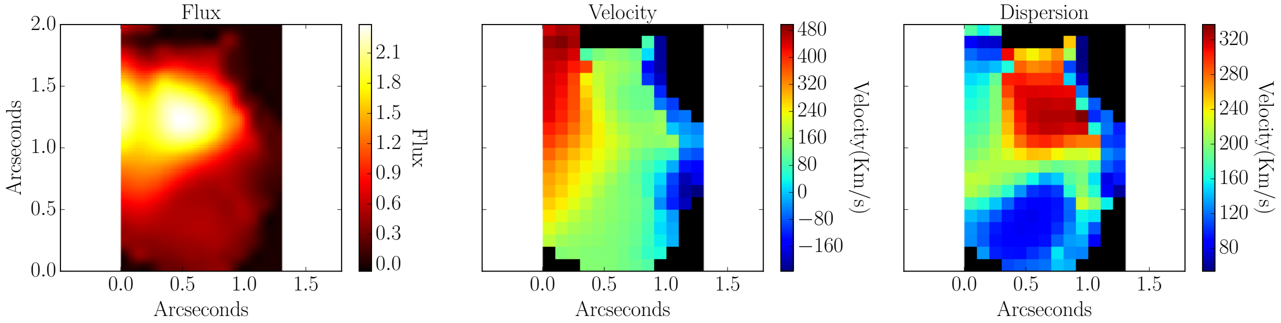

Figure 36: The integrated velocity flux map, velocity field map, and the dispersion map for Source G in SPT2349-56.

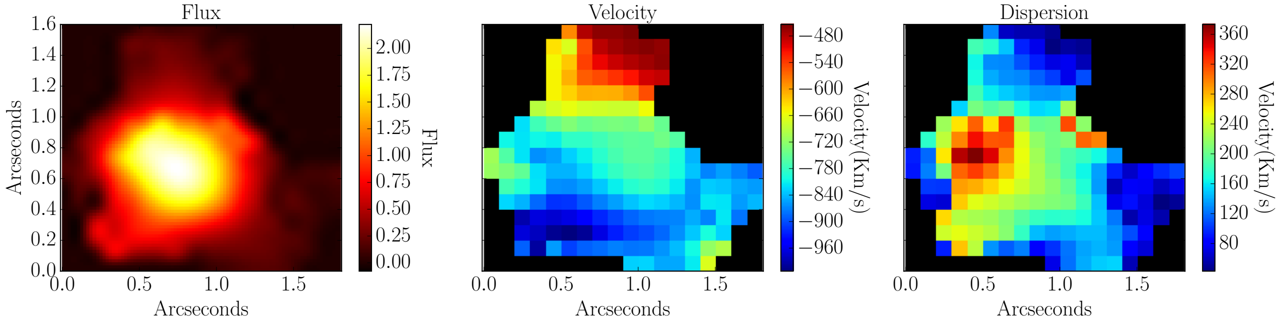

Figure 37: The integrated velocity flux map, velocity field map, and the dispersion map for Source H in SPT2349-56.

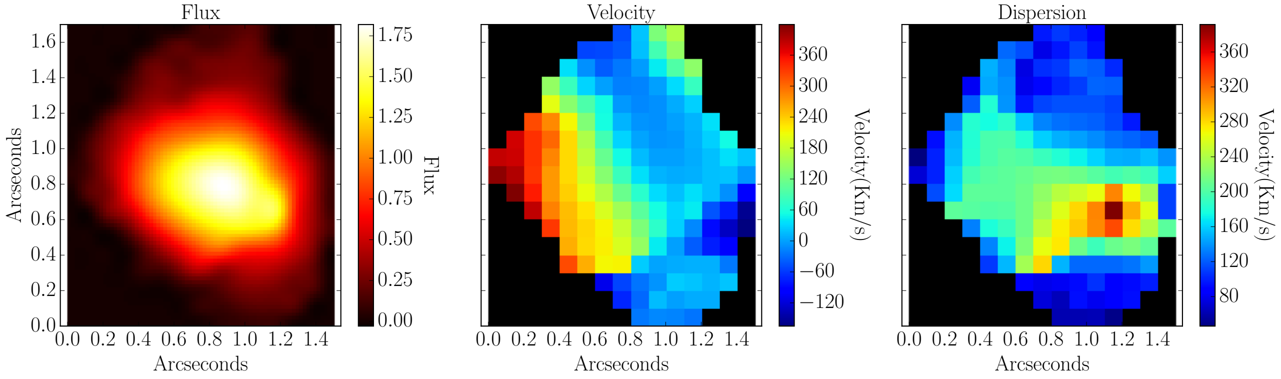

Figure 38: The integrated velocity flux map, velocity field map, and the dispersion map for Source I in SPT2349-56.

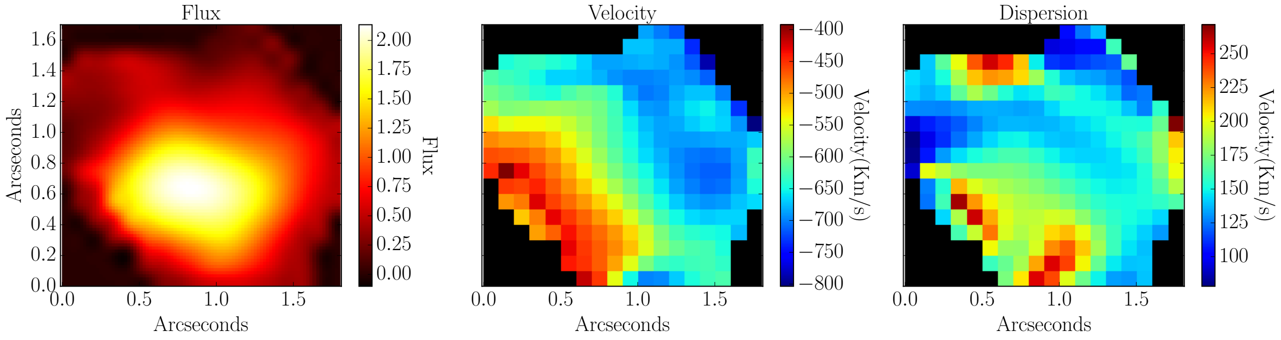

Figure 39: The integrated velocity flux map, velocity field map, and the dispersion map for Source J in SPT2349-56.

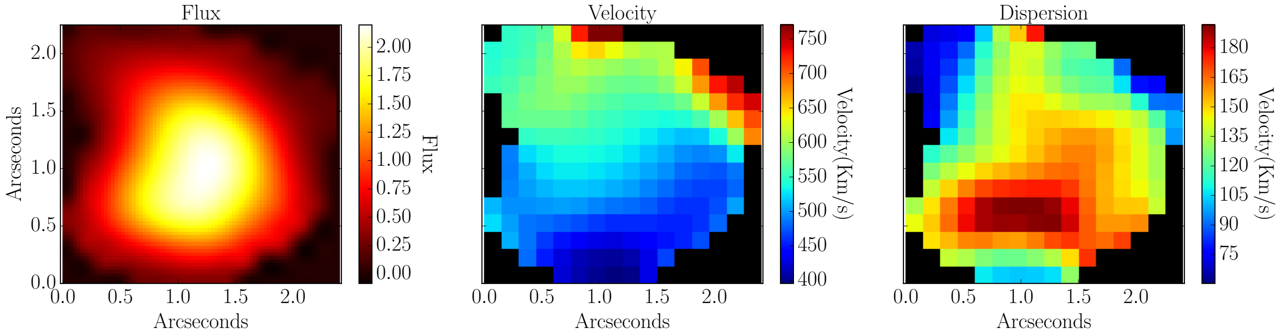

Figure 40: The integrated velocity flux map, velocity field map, and the dispersion map for Source K in SPT2349-56.

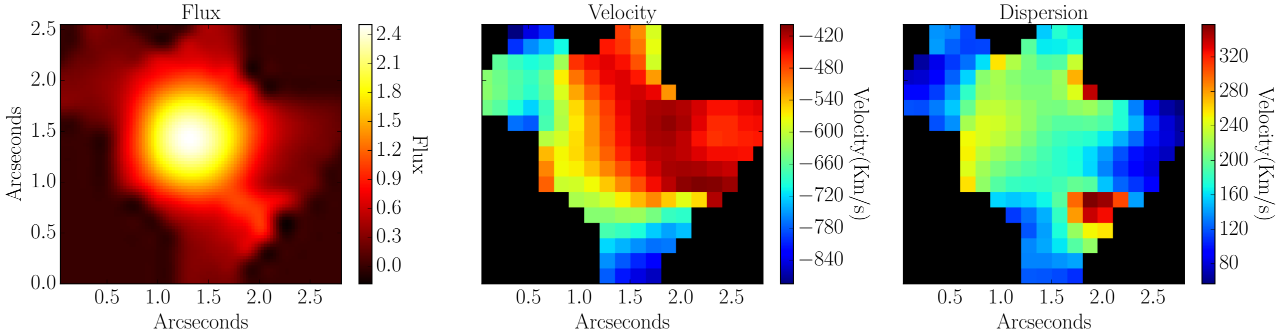

Figure 41: The integrated velocity flux map, velocity field map, and the dispersion map for Source L in SPT2349-56.

Appendix B

The following Appendix contains the rotation curves and chosen rotation axes for all the galaxies characterized in this thesis.

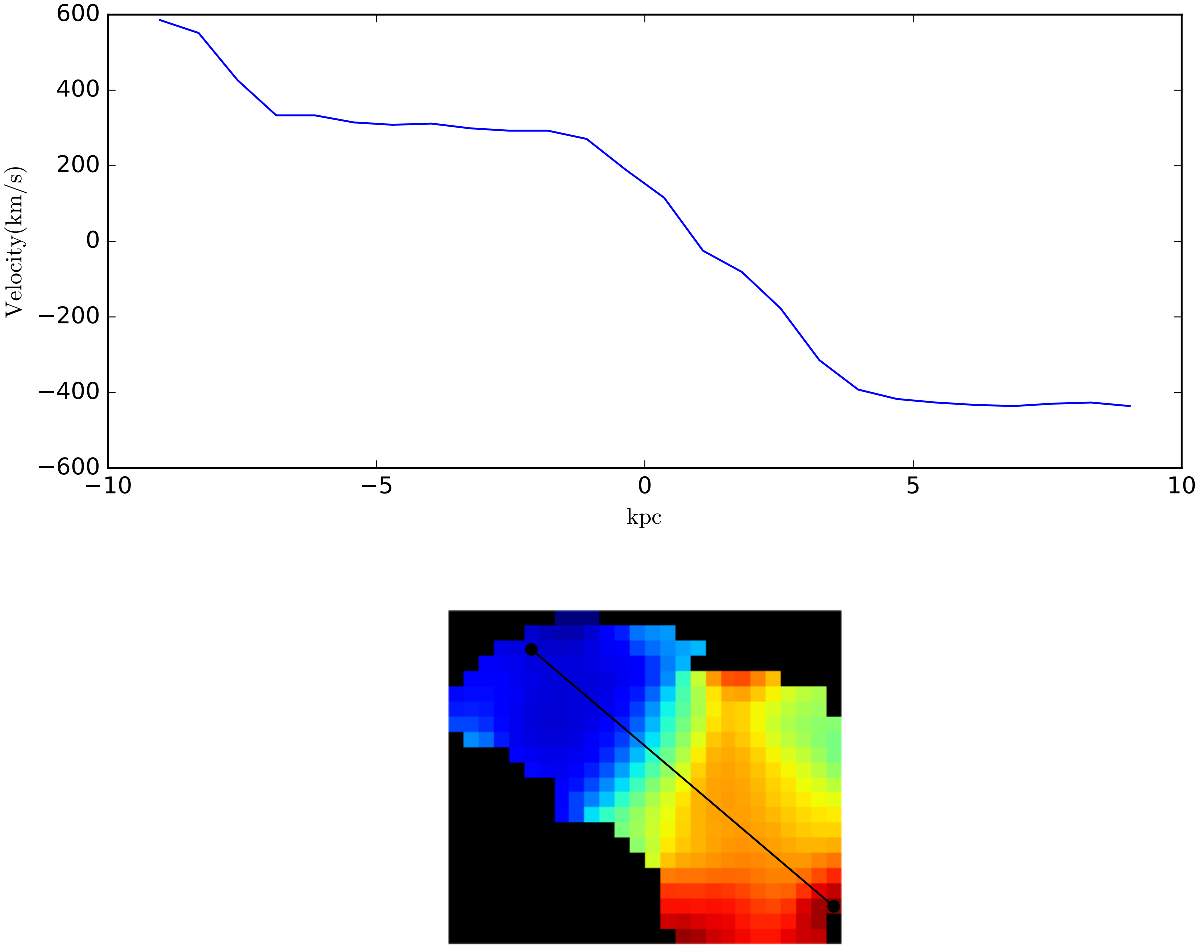

Figure 42: **Top:** The rotation curve measured from the velocity field of Source A. **Bottom:** The velocity field measured for Source A. The black line slicing through the map shows the major axis chosen in order to create the rotation curve.

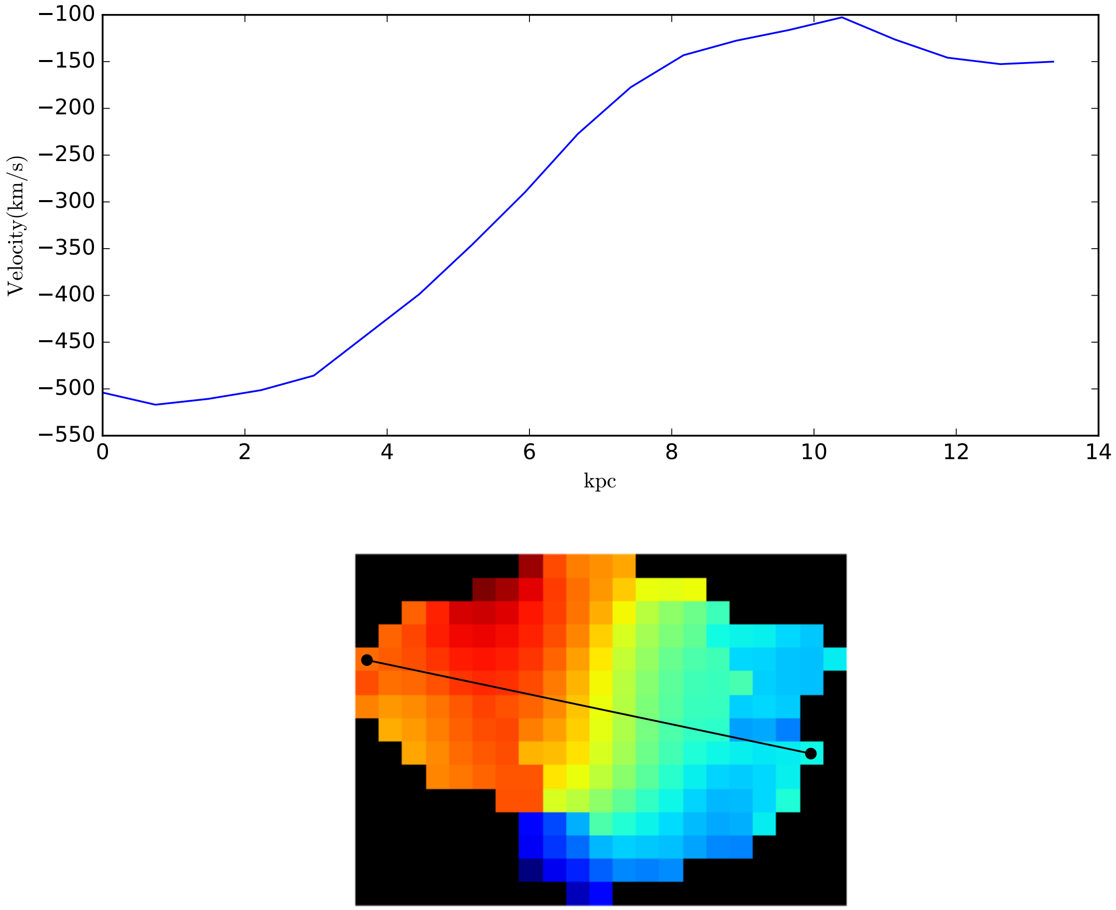

Figure 43: **Top:** The rotation curve measured from the velocity field of Source B. **Bottom:** The velocity field measured for Source B. The black line slicing through the map shows the major axis chosen in order to create the rotation curve.

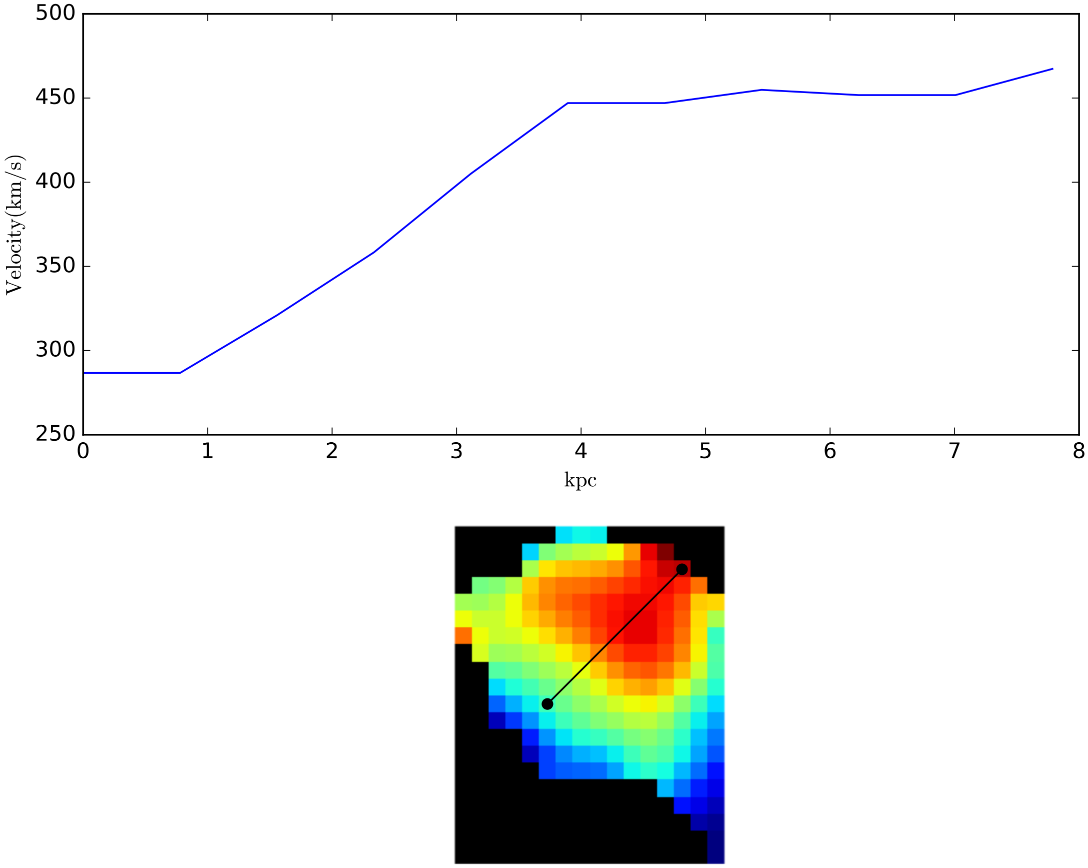

Figure 44: **Top:** The rotation curve measured from the velocity field of Source C. **Bottom:** The velocity field measured for Source C. The black line slicing through the map shows the major axis chosen in order to create the rotation curve.

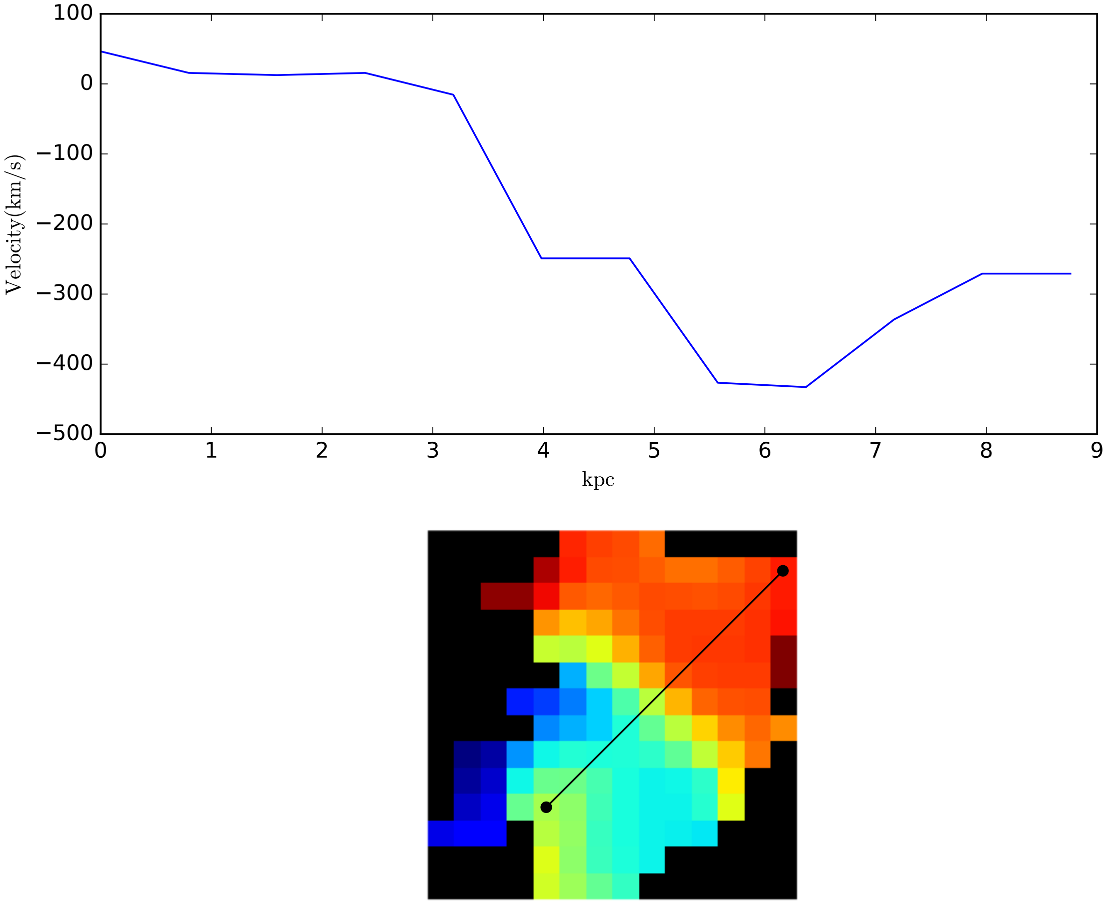

Figure 45: **Top:** The rotation curve measured from the velocity field of Source D. **Bottom:** The velocity field measured for Source D. The black line slicing through the map shows the major axis chosen in order to create the rotation curve.

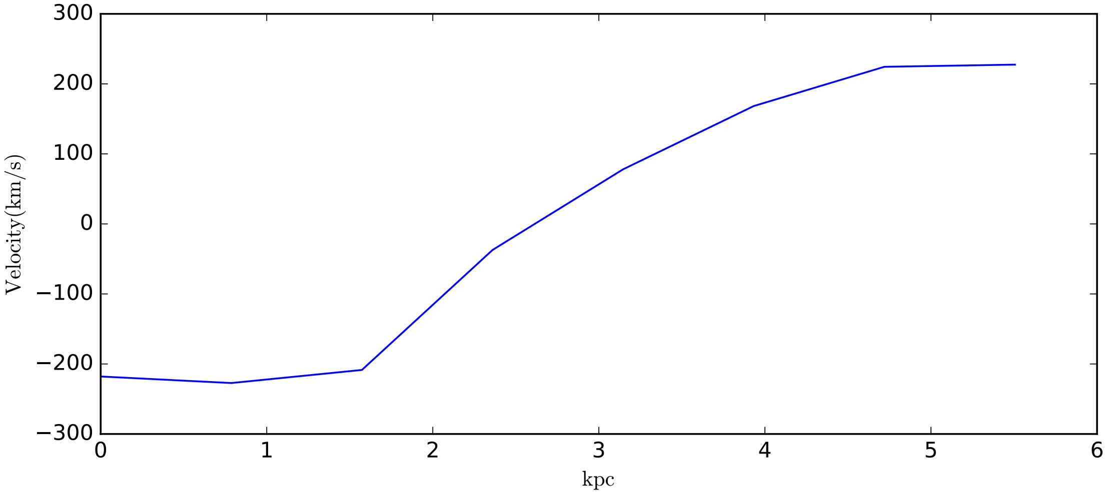

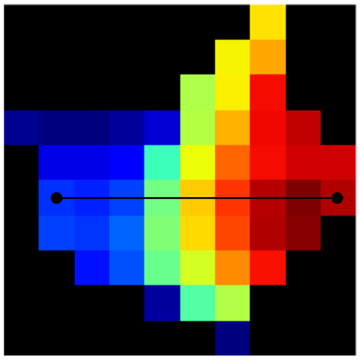

Figure 46: **Top:** The rotation curve measured from the velocity field of Source E. **Bottom:** The velocity field measured for Source E. The black line slicing through the map shows the major axis chosen in order to create the rotation curve.

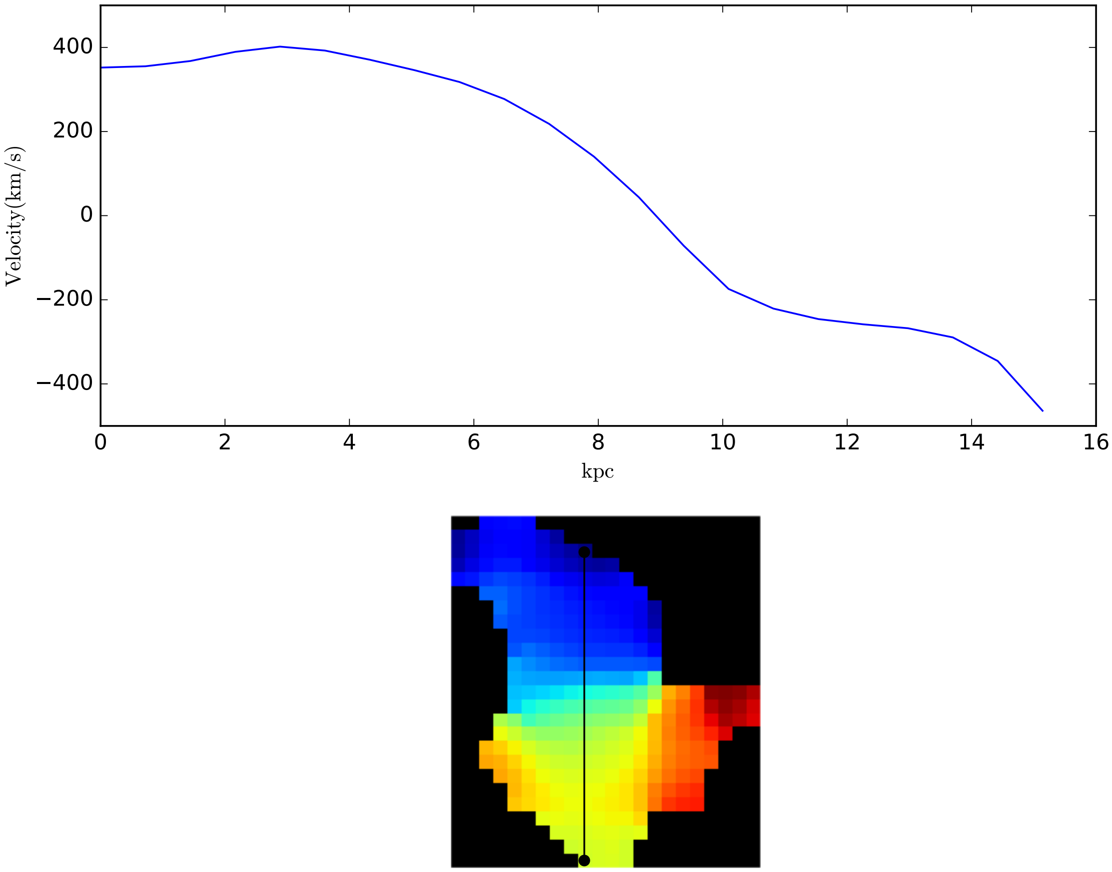

Figure 47: **Top:** The rotation curve measured from the velocity field of Source F. **Bottom:** The velocity field measured for Source F. The black line slicing through the map shows the major axis chosen in order to create the rotation curve.

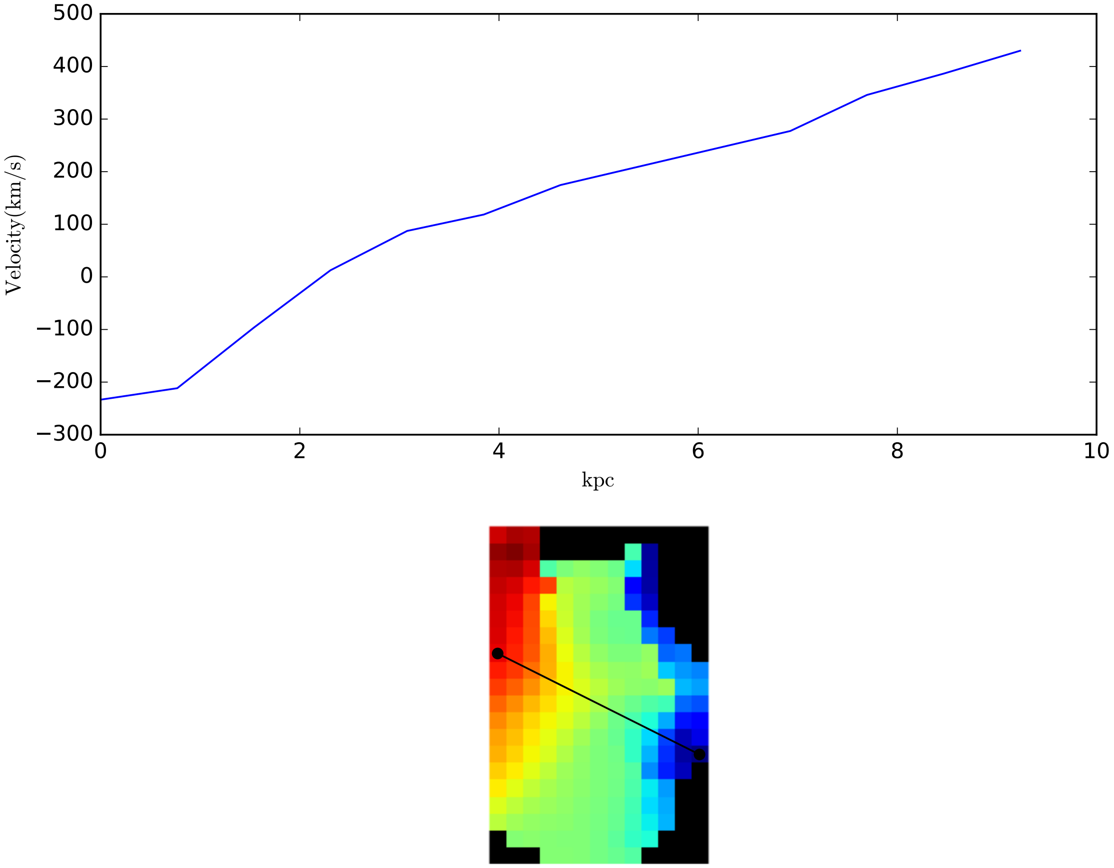

Figure 48: **Top:** The rotation curve measured from the velocity field of Source G. **Bottom:** The velocity field measured for Source G. The black line slicing through the map shows the major axis chosen in order to create the rotation curve.

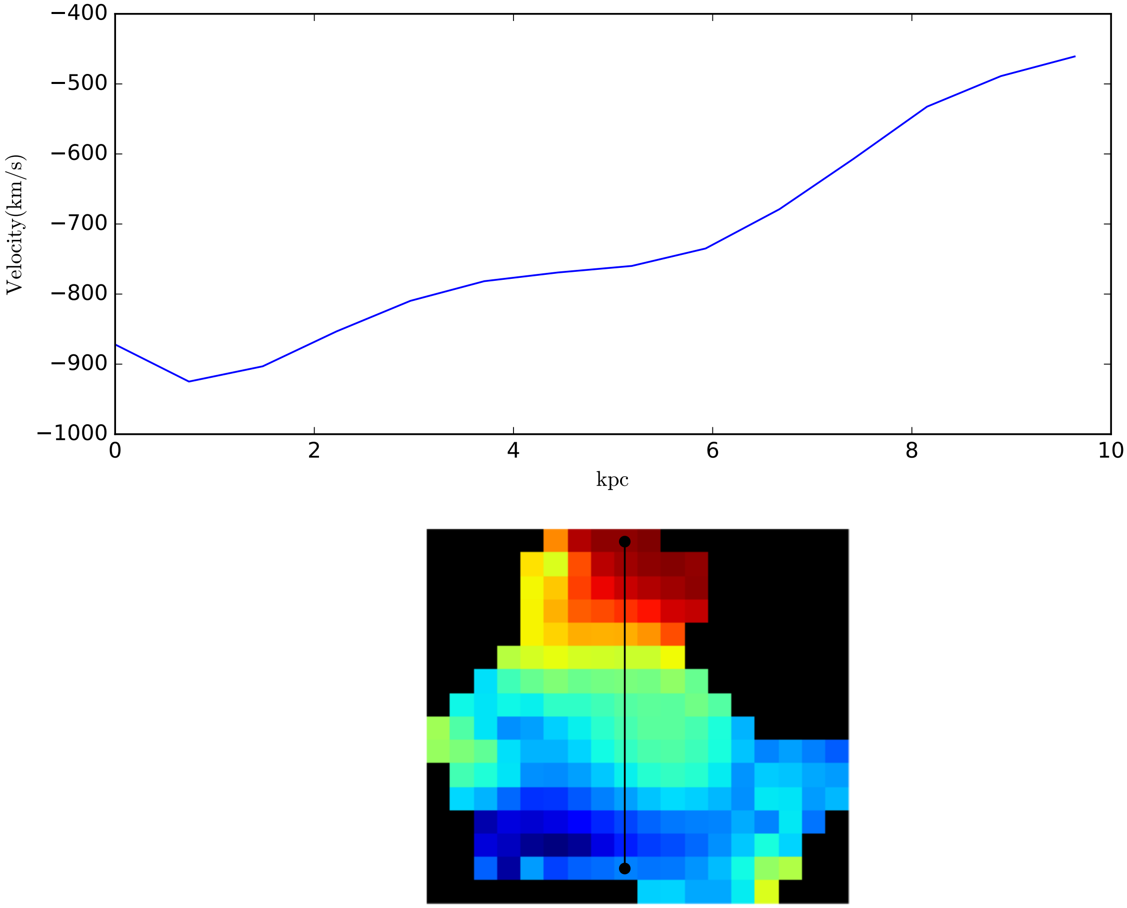

Figure 49: **Top:** The rotation curve measured from the velocity field of Source H. **Bottom:** The velocity field measured for Source H. The black line slicing through the map shows the major axis chosen in order to create the rotation curve.

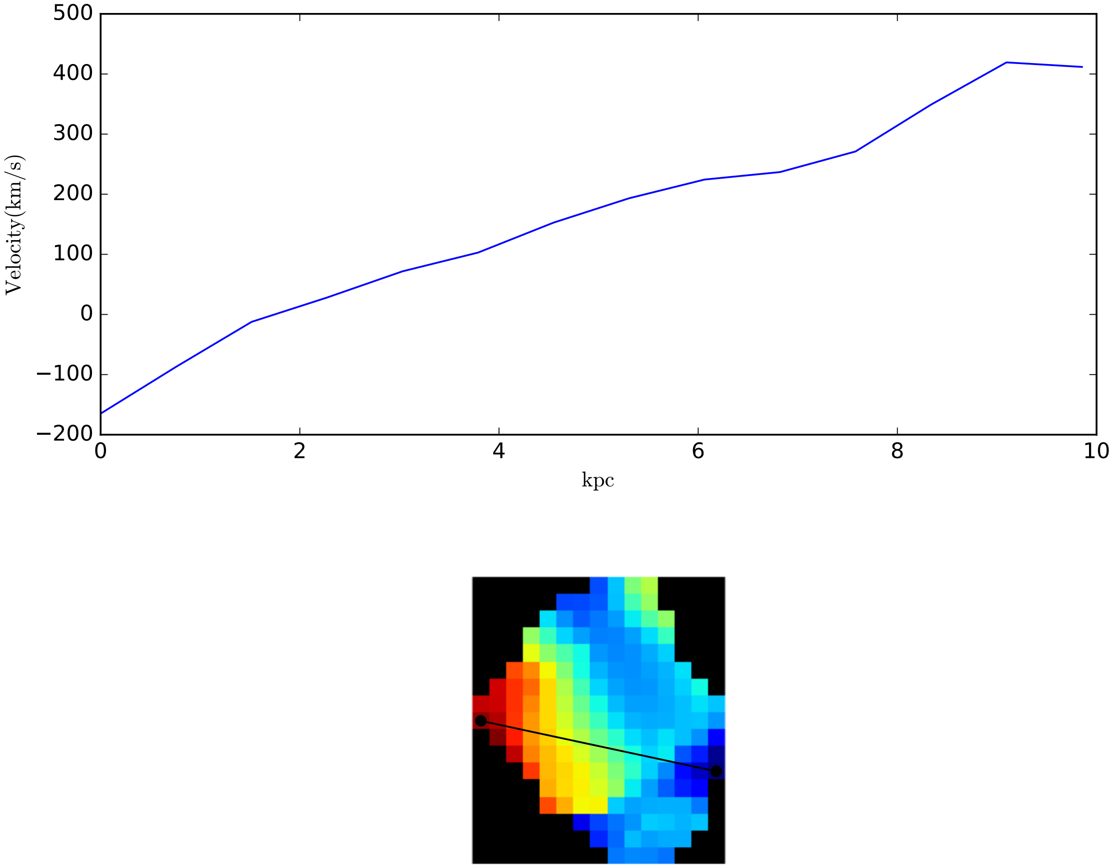

Figure 50: **Top:** The rotation curve measured from the velocity field of Source I. **Bottom:** The velocity field measured for Source I. The black line slicing through the map shows the major axis chosen in order to create the rotation curve.

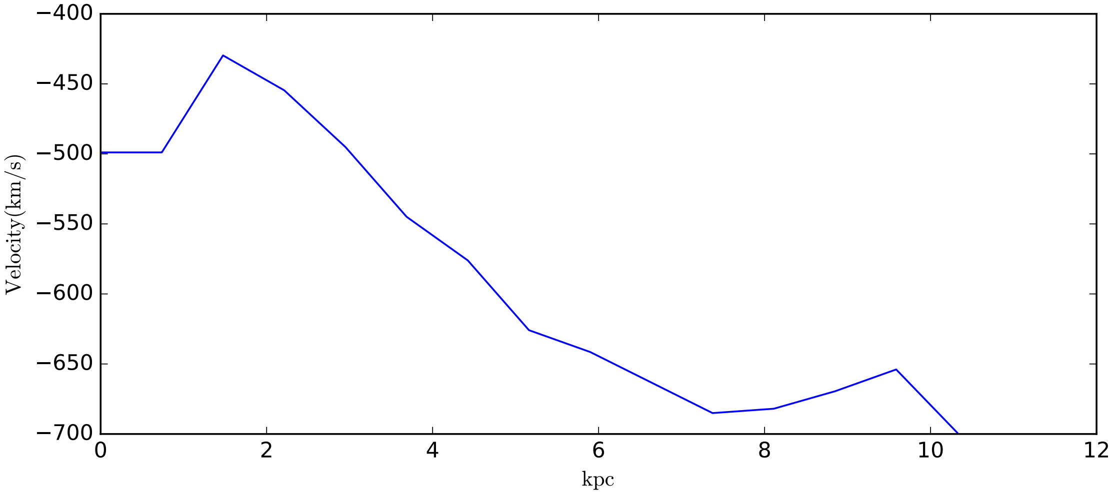

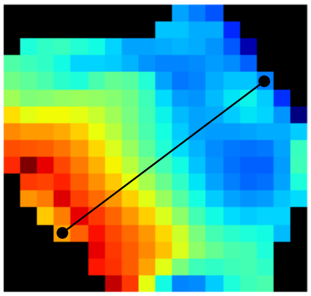

Figure 51: **Top:** The rotation curve measured from the velocity field of Source J. **Bottom:** The velocity field measured for Source J. The black line slicing through the map shows the major axis chosen in order to create the rotation curve.

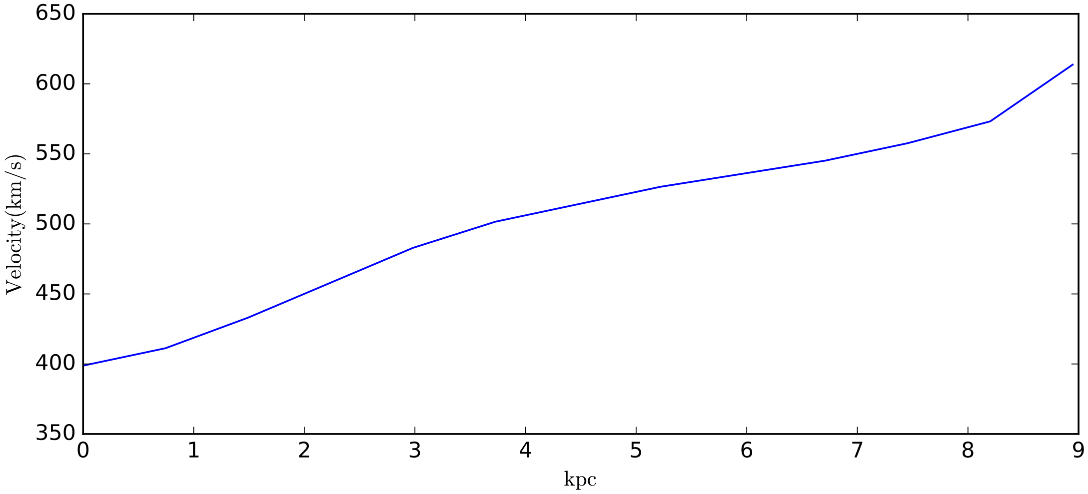

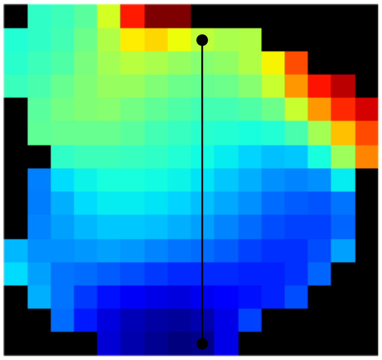

Figure 52: **Top:** The rotation curve measured from the velocity field of Source K. **Bottom:** The velocity field measured for Source K. The black line slicing through the map shows the major axis chosen in order to create the rotation curve.

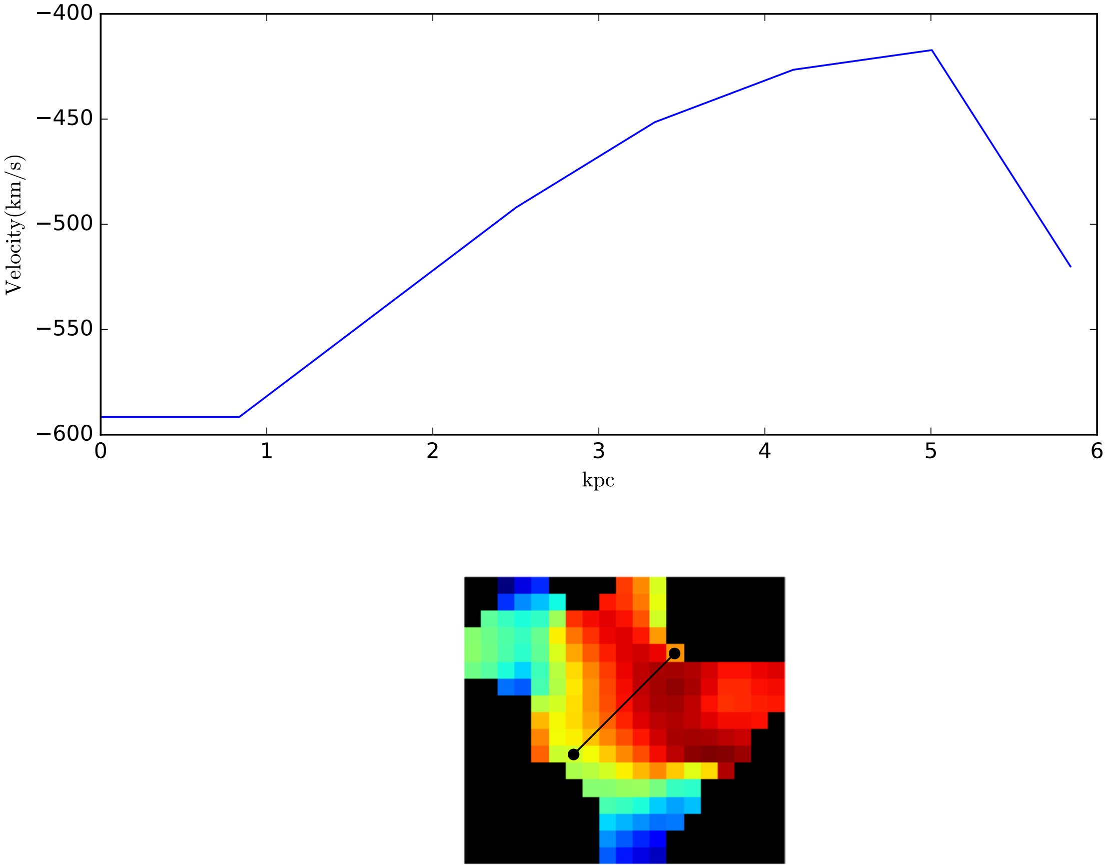

Figure 53: **Top:** The rotation curve measured from the velocity field of Source L. **Bottom:** The velocity field measured for Source L. The black line slicing through the map shows the major axis chosen in order to create the rotation curve.